5-2009

Mean kinematic vorticity of retrograde mylonite in the Brevard fault zone, South Carolina

Ching Tu
University of Tennessee

Recommended Citation

Tu, Ching, "Mean kinematic vorticity of retrograde mylonite in the Brevard fault zone, South Carolina. " Master's Thesis, University of Tennessee, 2009.
https://trace.tennessee.edu/utk_gradthes/5722

To the Graduate Council:

I am submitting herewith a thesis written by Ching Tu entitled "Mean kinematic vorticity of retrograde mylonite in the Brevard fault zone, South Carolina." I have examined the final electronic copy of this thesis for form and content and recommend that it be accepted in partial fulfillment of the requirements for the degree of Master of Science, with a major in Geology.

Robert D. Hatcher, Micah J. Jessup, Major Professor

We have read this thesis and recommend its acceptance:

Accepted for the Council:
Carolyn R. Hodges

Vice Provost and Dean of the Graduate School

(Original signatures are on file with official student records.)

To the Graduate Council:

I am submitting herewith a thesis written by Ching Tu entitled "Mean Kinematic Vorticity of Retrograde Mylonite in the Brevard Fault Zone, South Carolina" I have examined the final copy of this thesis for form and content and recommend that it be accepted in partial fulfillment of the requirements for the degree of Master of Science, with a major in Geology.

Prof. Robert D. Hatcher, Jr.
Co-advisor

Dr. Micah J. Jessup
Co-advisor

We have read this thesis
and recommend its acceptance:

Prof. Theodore C. Labotka

Acceptance for the Council:

Carolyn R. Hodge
Vice Provost and Dean of
The Graduate School

(Original signatures are on file with official student records.)

MEAN KINEMATIC VORTICITY OF RETROGRADE MYLONITE IN THE BREVARD FAULT ZONE, SOUTH CAROLINA

A Thesis
Presented for Partial Fulfillment of the Requirement for the
Master of Science Degree
University of Tennessee, Knoxville

Ching Tu
May, 2009

DEDICATION

To my beloved parents Tu, Chen-San and Tu-Chang, Yen-Feng, who always love and support me unconditionally…

謹獻給

在台灣我摯愛的父母杜建三與杜張月鳳

他們無條件的愛與支持是促使我能完成碩士學位最偉大的動力

ACKOWLEDGMENTS

I wish to thank my co-advisors Prof. Robert D. Hatcher, Jr., and Dr. Micah J. Jessup. I thank Prof. Hatcher for guidance, financial support, and unlimited patience in listening to my numerous questions as well as being my English teacher. He encouraged me to ask questions regardless of how stupid they may seem. Micah’s input provided invaluable ideas and taught me new techniques, and I appreciate his assistance. I also thank Dr. Theodore C. Labotka for being on my thesis committee and for carefully scrutinizing my thesis.

I am grateful to all of those who helped me in completing my research, especially during sample preparation. Both Dr. Michael J. Harrison at The Tennessee Technological University and Ms. Nancy Roberts in the Department of Civil Engineering at University of Tennessee, assisted me by providing access to rock saws to cut chips of my samples for thin sections and to keep my research on schedule.

It was a rough challenge taking two classes, teaching three labs, and writing and editing my thesis simultaneously. This tough mission could not have been done without editing and proofreading by Ms. Nancy Meadows. I thank members from the “Hatchery” family. Arthur Merschat, a strong bridge, helped me cross the gap between hydrogeology and Appalachian tectonics. William Gilliam and I met in summer 2005 at the field camp course for Indiana University, and he generously carried my rocks from Montana to Tennessee. It was a pleasure having conversations with Shawna Cyphers. I miss Mary Varnell who was playing cheer leader and saying “Good Job! Go Ching!” to me when I was stuck in my mysterious vorticity. Heather Byers reminded me to print out extra resumes and business cards for the AAPG Student Expo, the result being that I received a job offer. I enjoyed having Makino’s shushi with Brittany Davis. Andrew Wunderlich provided many helps in GIS and GeoRef matters. Matt Huebner, the office early bird, was always making coffee in the morning; it was important to a person like me who drinks a lot of coffee. Phillip Derryberry, my officemate, bravely tolerated my emotional fluctuations. To all of you, I owe you an apology; I forgot how to smile for a while. I think I will miss coffee shop brain storm sessions on Friday mornings with the “Jessupy.”

I sincerely thank my parents and my family members in Taiwan. I am so lucky to have a pair of awesome parents who love and trust me unconditionally. My brother, Tu, Ben-Chen and sister–in–law Lu, Xiu-Wen kept me posted about the family’s health and welfare.

To my dear friends, Wang, Lung-Wen and Liu, Lirong, you encouraged me to use my curiosity in a different way. Your support kept me away from the “critical threshold” when I was almost reaching my physical and mental “yield point.”

Last, but not least, I would like to thank all the faculty, staff, and colleagues of the UT Department of Earth and Planetary Sciences for offering me a home.

"*J'ai duex amour. Mon pays et Knoxville…*" *Josephine Baker* (1931).

ABSTRACT

The Brevard fault zone (BFZ) is one of the largest faults in the southern Appalachians, extending from Virginia to Alabama. It was originally recognized as a relatively narrow (1-3 km-wide) low-grade metamorphic belt, flanked by high-grade rocks on both sides. Recently, the concept of the BFZ has been expanded to include a wide (> 10 km) shear zone exposed over much of the Inner Piedmont (IP) with high-grade metamorphism, indicating incipient A-subduction by the exotic Carolina superterrane of Laurentia and other Paleozoic terranes. Exhumation processes are reflected in the retrograde metamorphic gradient across the IP into the Blue Ridge.

The main objective of this thesis is to delimit the relative contributions of pure and simple shear (kinematic vorticity) along strike within the retrograde mylonite in the study area (32 km^2). Vorticity analysis is regarded as a useful approach in various tectonic settings to estimate pure/simple shear during non-coaxial progressive deformation. In the BFZ, feldspar porphyroclasts and other clasts were observed in the shear zone rocks, which were used to estimate mean kinematic vorticity (W_m). To improve data credibility, orientation of every sample was documented in detail and the vorticity data were plotted on the rigid grain net. Higher and lower W_m values were grouped. Results indicated that higher W_m values are associated with SW-directed crustal transport. Mesoscopic W_k values in the high-grade Neoacadian BFZ are substantially higher than W_m values in the early Alleghanian BFZ, a result of ductile deformation during the early

Alleghanian orogeny. A triclinic deformation mechanism may have contributed to the W_m high-low patterns. Quartz c-axis patterns are similar to those from a previous study, and reveal a top-to-the-SW shear sense.

TABLE OF CONTENTS

LIST OF TABLES

LIST OF FIGURES

CHAPTER I

INTRODUCTION

The retrograde Brevard fault zone (BFZ) is an Alleghanian 1-3 km-wide linear belt of different rock types flanked on either side by relatively higher grade rocks. It extends ~750 km from Virginia to Alabama. The retrograde BFZ separates the Blue Ridge (BR) from the Inner Piedmont (IP) in the southern Appalachians (Reed and Bryant, 1964; Roper and Dunn, 1973; Edelman et al., 1987; Hatcher, 2001; Merschat et al., 2005; Hatcher et al., 2007). Previous investigations employed field mapping, geochemistry, geochronology, and kinematic analysis to characterize the BFZ (Sinha and Glover, 1978; Sinha et al., 1988; Condie and Sinha, 1996; Hatcher et al., 2000; Hatcher, 2001; Hatcher et al., 2007). Results from these investigations indicate that BFZ lithologies have undergone several phases of ductile deformation; a brittle deformation occurred at the last stage of the Alleghanian orogeny.

The Alleghanian BFZ is dominated by penetrative, heterogeneous strain, retrograde metamorphism, and evidence for fluid flux (chlorite overprint) that occurred during the early- to late-Alleghanian orogeny (Sinha et al., 1988). My study endeavored to perform kinematic analysis of samples collected along strike in the best-exposed portion of the BFZ to quantify the relative contributions of pure and simple shear during the early Alleghanian orogeny. The study area was located in South Carolina (Fig. 1-1) in parts of the Whetstone and Tamassee 7.5-minute quadrangles. Detailed geologic mapping and mesofabric analysis

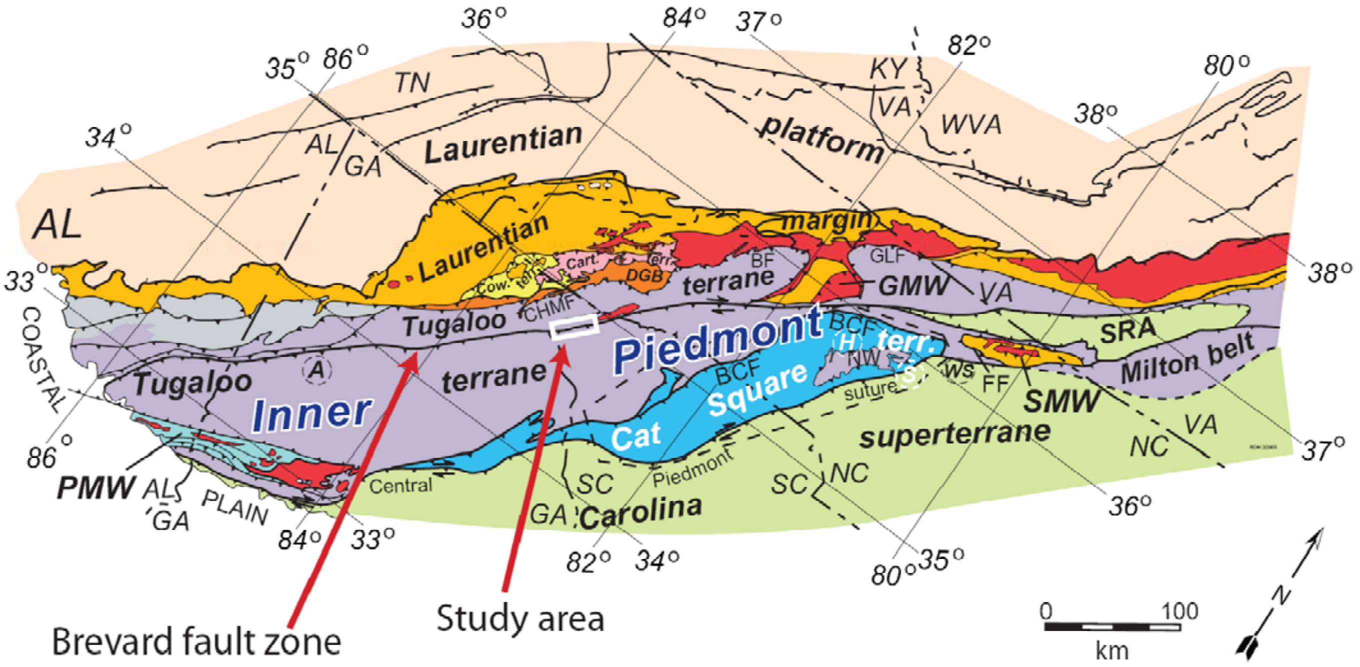

Figure 1-1. Simplified tectonic map of the southern Appalachians showing the location of the Brevard fault zone, Inner Piedmont, and other terranes (after Hatcher and Merschat, 2006). White box is the location of the study area. BCF: Brindle Creek fault. BF: Burnsville fault. Cart. terr.: Cartoogechaye terrane. CHMF: Chattahoochee-Holland Mountain fault. Cow. terr.: Cowrock terrane. DGB: Dahlonega gold belt. FF: Forbrush fault. GLF: Gossan Lead fault. GMW: Grandfather Mountain window. Light gray: probable western Tugaloo terrane rocks in Alabama and Georgia. NW: Newton window. S: Statesville. SMW: Sauratown Mountains window. SRA: Smith River allochthon. A: Atlanta. H: Hickory. WS: Winston-Salem.

conducted in the study area by Hatcher (1971) and Hatcher et al. (2000) provided an ideal background for my detailed microstructural and kinematic analyses.

Vorticity analysis is an important tool for estimating the relationships between pure and simple shear in deformed rocks (Means et al., 1980; Bobyarchick, 1986). Passchier (1987, 1988) suggested that the orientation and aspect ratio (R) of rigid porphyroclasts in a ductile matrix can be used to estimate the mean kinematic vorticity number (W_k). W_k is a dimensionless number between 0 (100% pure shear) and 1 (100% simple shear) that quantifies the relationship between pure and simple shear during non-coaxial progressive deformation (Means et al., 1980). Assuming the deformation occurs under steady-state conditions, the ratio of pure and simple shear for various W_k values is non-linear (Tikoff and Fossen, 1995; Law et al., 2004). However, steady-state deformation may oversimplify the deformation mechanism, especially in a channel-flow type tectonic setting (Jiang and White, 1995). An alternative interpretation is suggested by Jiang and White (1995), indicating W_k can be estimated in a non-steady-state flow regime (Fig. 1-2). Kinematic vorticity analysis has been used to study a variety of tectonic settings, such as transpression, compression, extension, and extrusion (Wallis, 1995; Simpson and de Paor, 1997; Xypolias and Doutsos, 2000; Wells, 2001; Xypolias and Koukouvelas, 2001; Bailey and Eyester, 2003; Bailey et al., 2004; Jessup et al.,

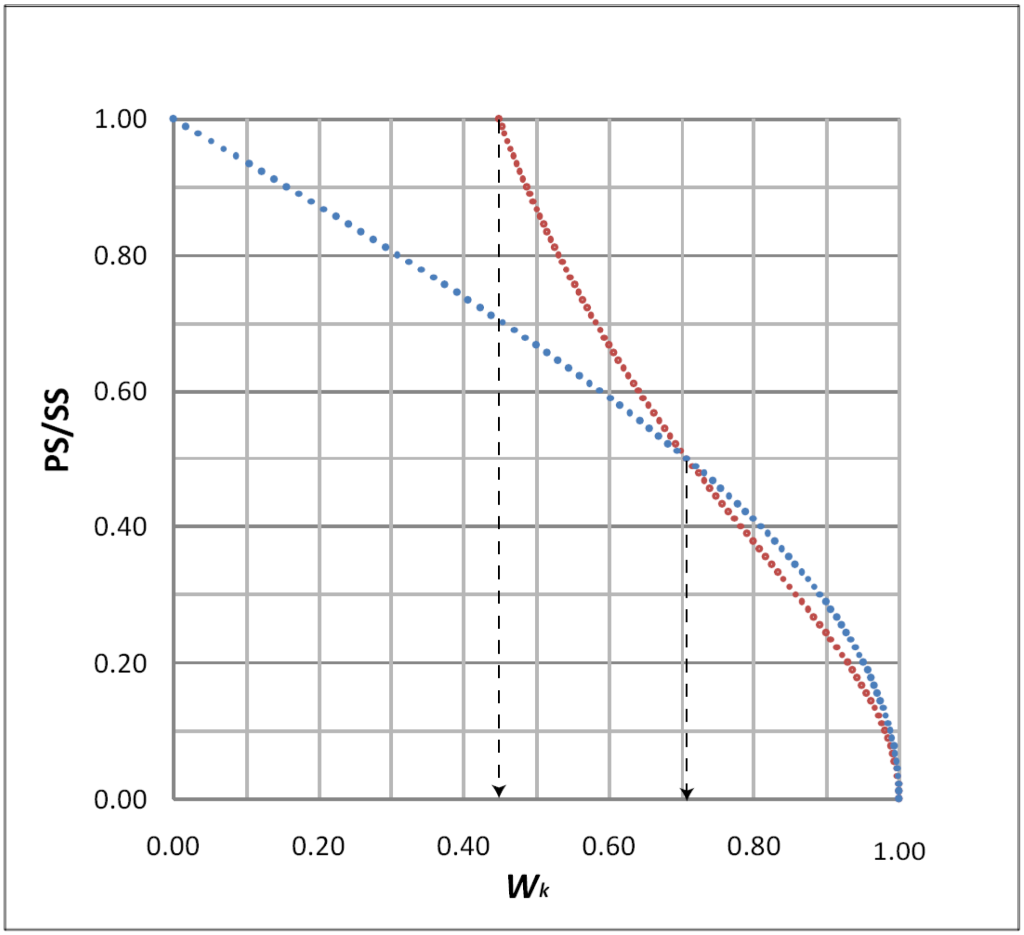

Figure 1-2. Pure shear (PS)/simple shear (SS) vs. W_k in a steady-state deformational system (blue dotted line) (Law et al., 2004), and a non-steady-state deformational system (red dotted line) (Jiang and White, 1995). Agreement of the two curves, which contribute equally to pure/simple shear ($W_k = 0.71$). When $W_k > 0.71$, deformation is dominated by simple shear, and the discrepancy between steady-state and non-steady-state deformation is relatively insignificant. When $W_k < 0.71$, pure shear dominates and the ratio of pure/simple shear deviates significantly. Under non-steady-state conditions, crustal loading could facilitate sheared rock mass transportation laterally. So, pure shear is underestimated for values of $W_k < 0.45$.

2006, 2007). These results indicate that kinematic vorticity analysis is a useful method to better understand tectonic evolution and deformation history.

GOALS

This study attempts to 1) estimate the relative contributions of pure and simple shear along parts of the reactivated BFZ to help decipher its kinematic evolution and deformational history during the Late Carboniferous-Permian (300–270 Ma; Sinha et al., 1988); and 2) study petrofabrics and microstructures in the study area.

METHODS

Fifteen oriented samples were collected from twelve localities in the BFZ in South Carolina. Thin sections were cut normal to dominant foliation, and parallel and perpendicular to the most prominent mineral lineation. Thin sections were prepared by a commercial thin section maker in order to carry out mean kinematic vorticity and quartz *c*-axis analyses using a petrographic microscope.

HYPOTHESIS

The reactivated BFZ may have involved a more complicated deformation scheme than monoclinic deformation. The dominant 3D strain mechanism is probably triclinic.

OBJECTIVES

Two methods were employed to carry out mean kinematic analyses.

1) Rigid-body rotation analysis: the rigid grain net (RGN) method (Jessup et al., 2007) was used to carry out rigid-body rotation analyses. Oriented samples of retrograde mylonitic Henderson Gneiss (MHG) and mylonitic gneiss (MG) were collected and mean kinematic vorticity number was determined by measuring the parameters of rotating rigid bodies in thin section, including long and short axes of rigid grains and the angles between long axes and dominant foliation planes.
2) Quartz *c*-axis analysis: quartz-rich layers were studied within the MGH and phyllonite. These samples were collected to carry out quartz *c*-axis analysis.

TECTONIC AND GEOLOGIC SETTING OF THE BREVARD FAULT ZONE

Tectonic Setting of the Brevard Fault Zone

The BFZ probably formed during the Neoacadian orogeny (407-350 Ma) when the Carolina superterrane collided with Tugaloo and other more westerly terranes (Merschat et al., 2005; Hatcher and Merschat, 2006). This event may have produced a wide shear zone (>10 km) and a dextral, SW-directed tectonically formed orogenic channel as Tugaloo and Cat Square terranes were A-subducted beneath the Carolina terrane (Hatcher and Merschat, 2006; Hatcher et al., 2007). This process resulted in anatexis in the IP and eastern BR and SW-directed mid-crustal flow with approximately 200-400 km of displacement (Fig.1-3) (Hatcher and Merschat, 2006). The first reactivation event in the BFZ occurred during

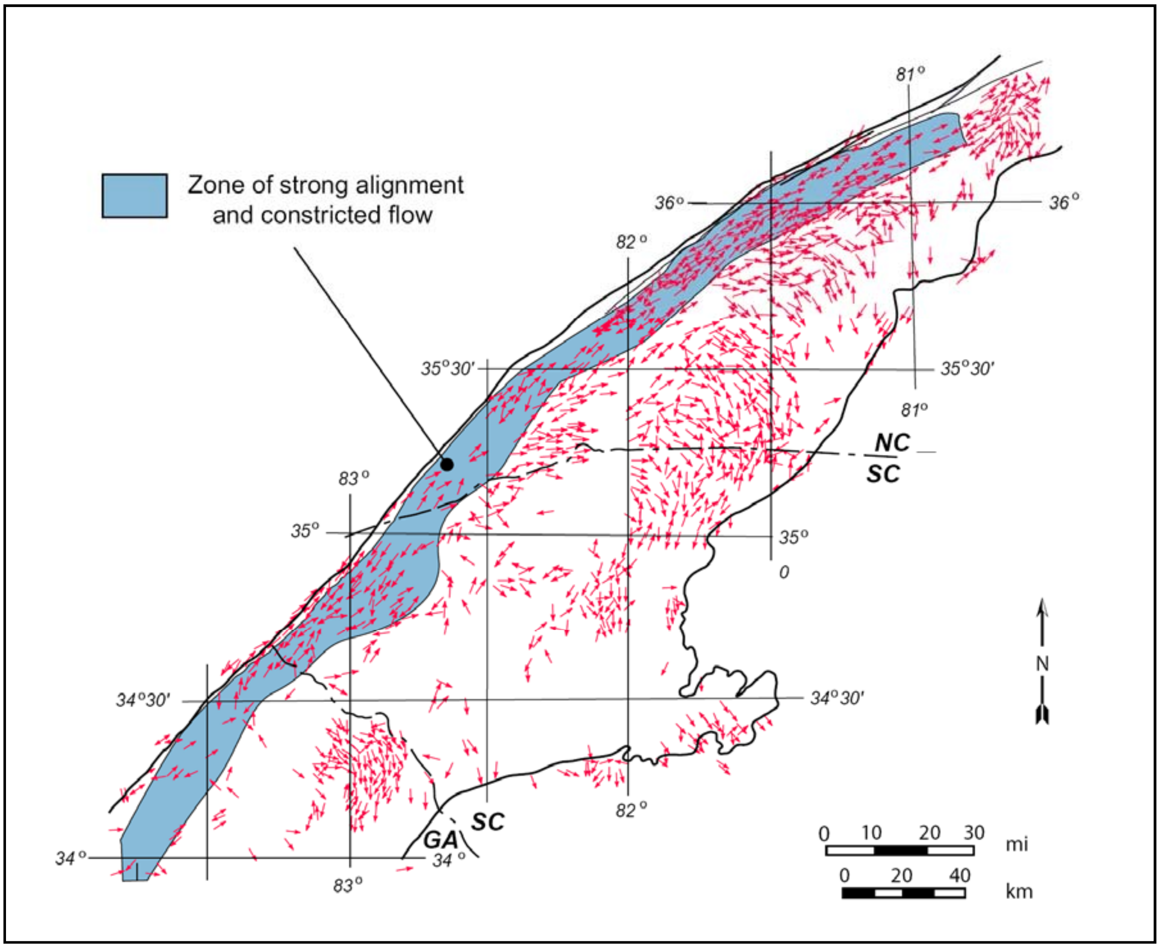

Figure 1-3. Outline map of the IP showing the high temperature pattern of mineral lineations (red arrows) formed during the Neoacadian orogeny. Shaded area outlines the buttress that produced constricted flow, which also corresponds approximately to the area of the retrograde BFZ. After Hatcher, 2001.

the Alleghanian orogeny, producing dextral reactivation at greenschist facies conditions. The second reactivation event occurred under brittle conditions with approximately 10-20 km of dip-slip displacement along its NW boundary from Atlanta, GA, northeastward; however, displacement along the early Alleghanian fault is difficult to estimate, because no markers exist on either side of the fault to determine offset (Hatcher, 2001; Hatcher et al., 2007).

Alleghanian Retrograde Brevard Fault Zone

The Alleghanian orogeny lasted ~60 m.y., from the Late Carboniferous into the Permian, during which time an evolving stress regime was produced by the “zippered” north–to–south collision of Gondwana and Laurentia (Fig. 1-4) (Hatcher, 2002). Rb-Sr geochronologic data indicate that the reactivated BFZ formed in a “fluid-enhanced” environment during the late Pennsylvanian and Early Permian (~273 Ma) (Sinha et al., 1988). As a result, deformation in the BFZ occurred during the early Alleghanian at ductile conditions associated with fluid flux, whereas during the later Alleghanian deformation was entirely brittle, forming the Rosman fault (Hatcher, 2001).

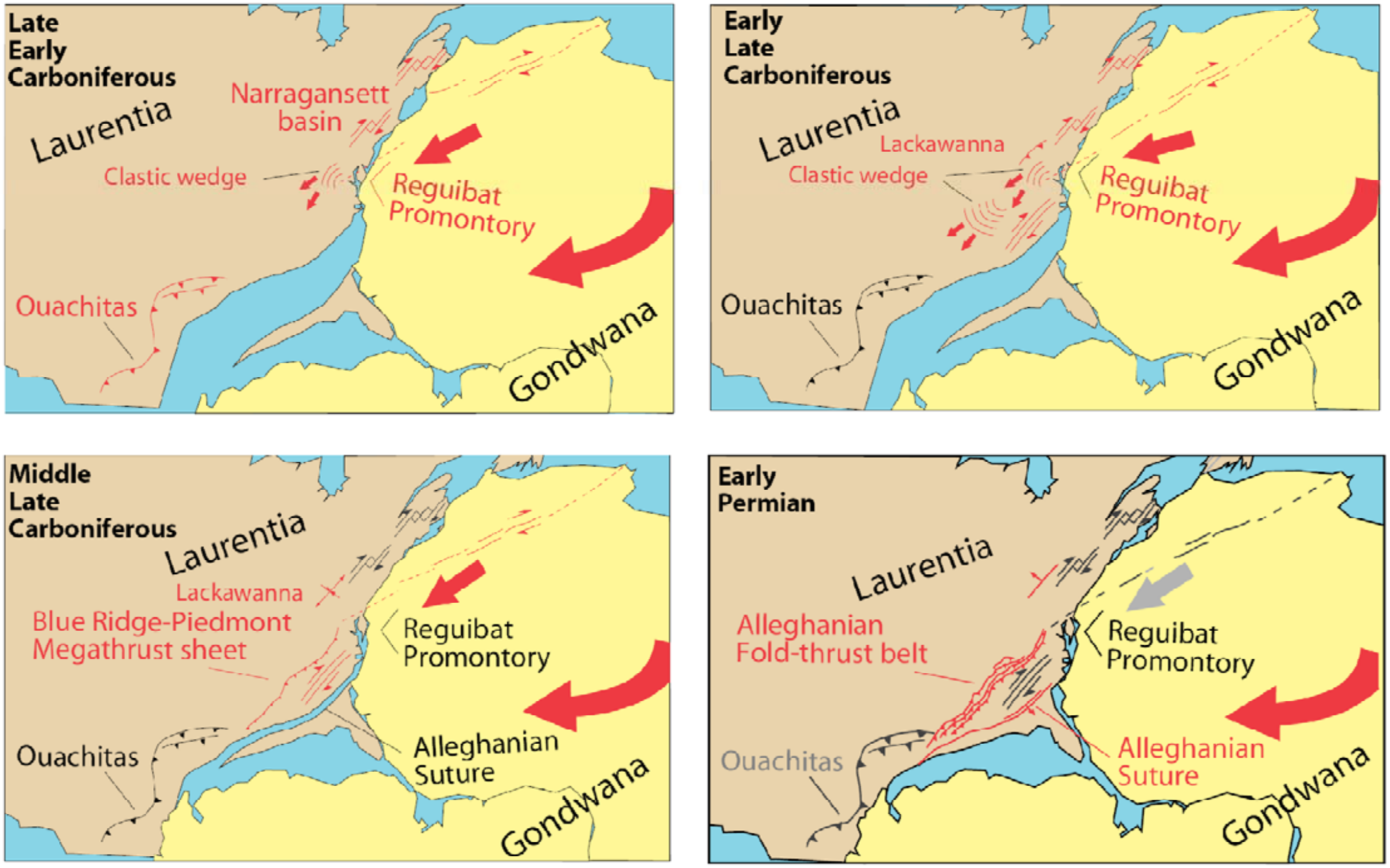

Figure 1-4. Reconstructed motion of continents during the final assembly of Pangea. Gondwana collided with Laurentia north to south and triggered the BFZ reactivation (Hatcher, 2002). Red arrows indicate motion direction. Gray and black labels represent tectonic motion ceased.

Geologic Setting

The BFZ in the study area consists of a series of NE-striking narrow belts of different rock types including phyllonite, graphite phyllonite, quartzite, and impure marble, composing the Chauga River Formation (Hatcher et al., 2000). On a geologic map (Fig. 1-5), the fault zone is characterized as a low-grade metamorphic zone that is flanked by higher-grade rocks (Reed and Bryant, 1964; Hatcher et al., 2000). The prograde metamorphic (Fig. 1-6) assemblage SE of the BFZ (Chauga belt) contains garnet ± staurolite porphyroblasts (Roper and Dunn, 1973; Hatcher et al., 2000). Feldspar porphyroclasts are present in the MHG (Fig. 1-7) and in its protolith, the high-temperature Henderson Gneiss (Hatcher et al., 2000; Gatewood, 2007). The BFZ truncates Tugaloo terrane rocks on both sides of the BFZ that consist of metagraywacke, aluminous schist, amphibolite, and granitic rocks, and reached medium to high grade (Griffin, 1971; Hatcher, 1971). A polyphase Paleozoic tectonic history is reflected in Neoacadian high-temperature and medium-pressure, kyanite- and sillimanite-bearing mineral assemblages that are overprinted by Alleghanian low-temperature and low-pressure, garnet- bearing assemblages (Roper and Dunn, 1973).

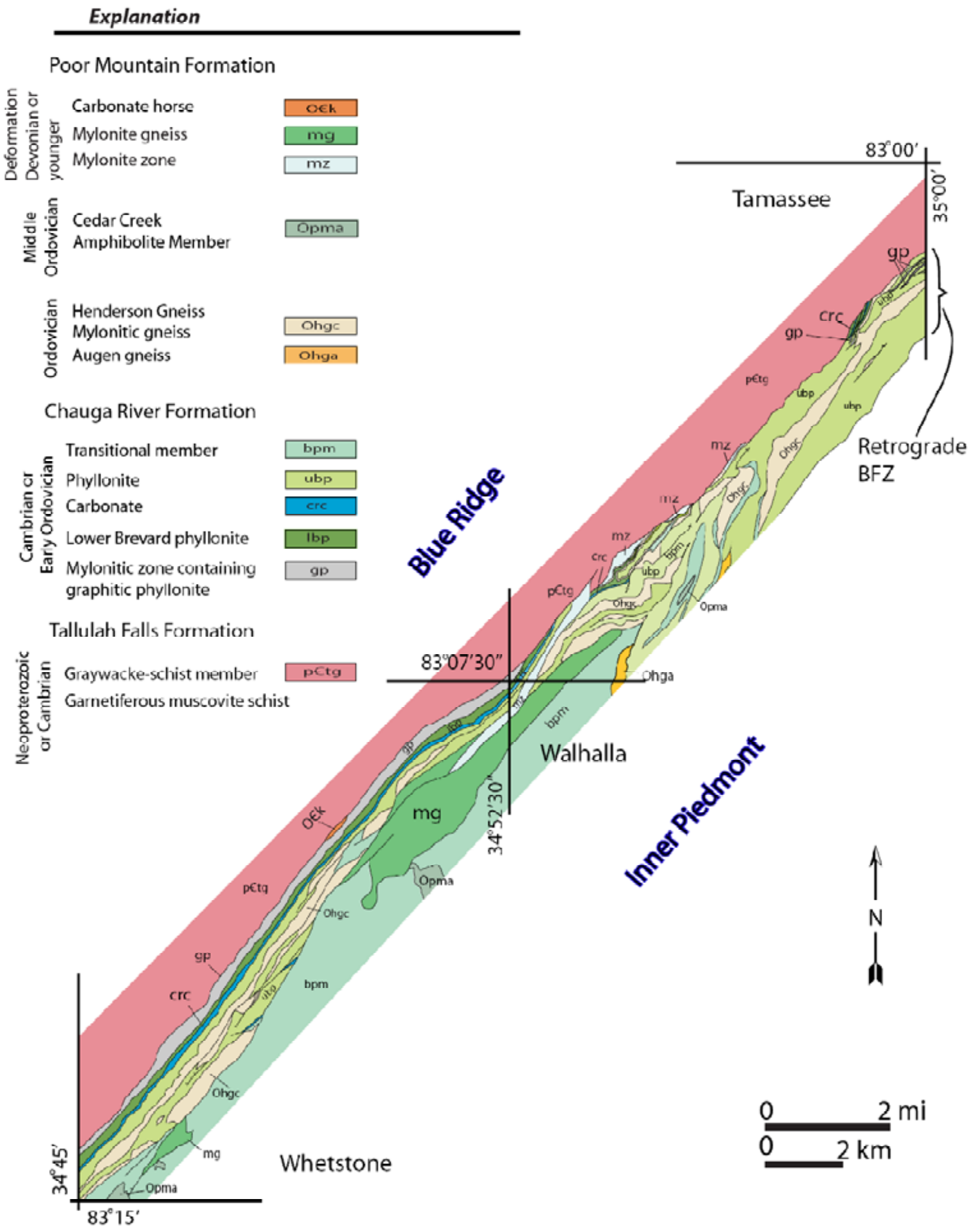

Figure 1-5. Geologic map of parts of Tamassee, Walhalla, and Whetstone quadrangles, South Carolina. After Griffin (1971), Hatcher et al. (2000), and Hatcher and Acker (unpublished map).

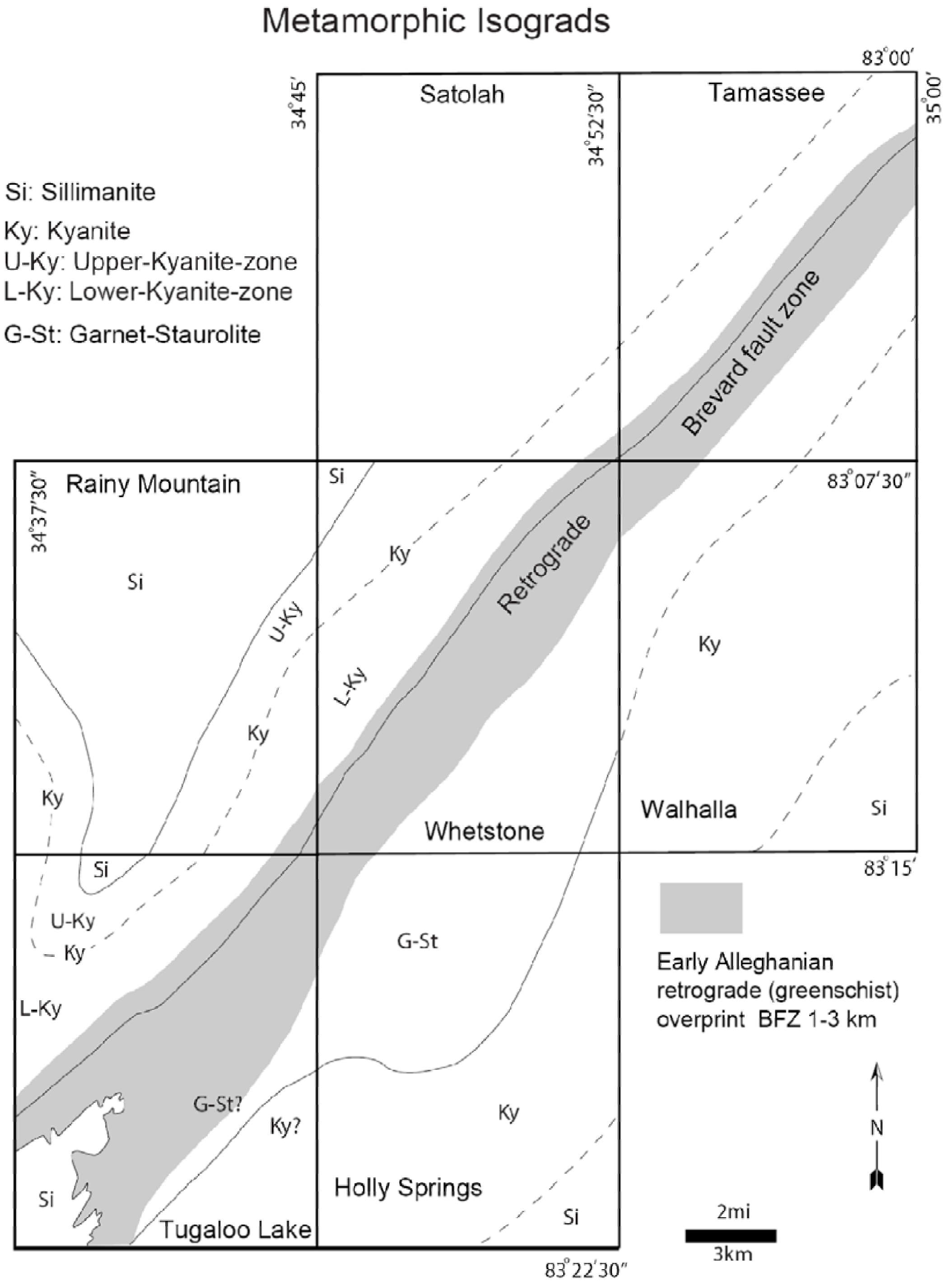

Figure 1-6. Metamorphic grade of the BFZ and adjacent area in northwestern SC. After Hatcher et al., 2000.

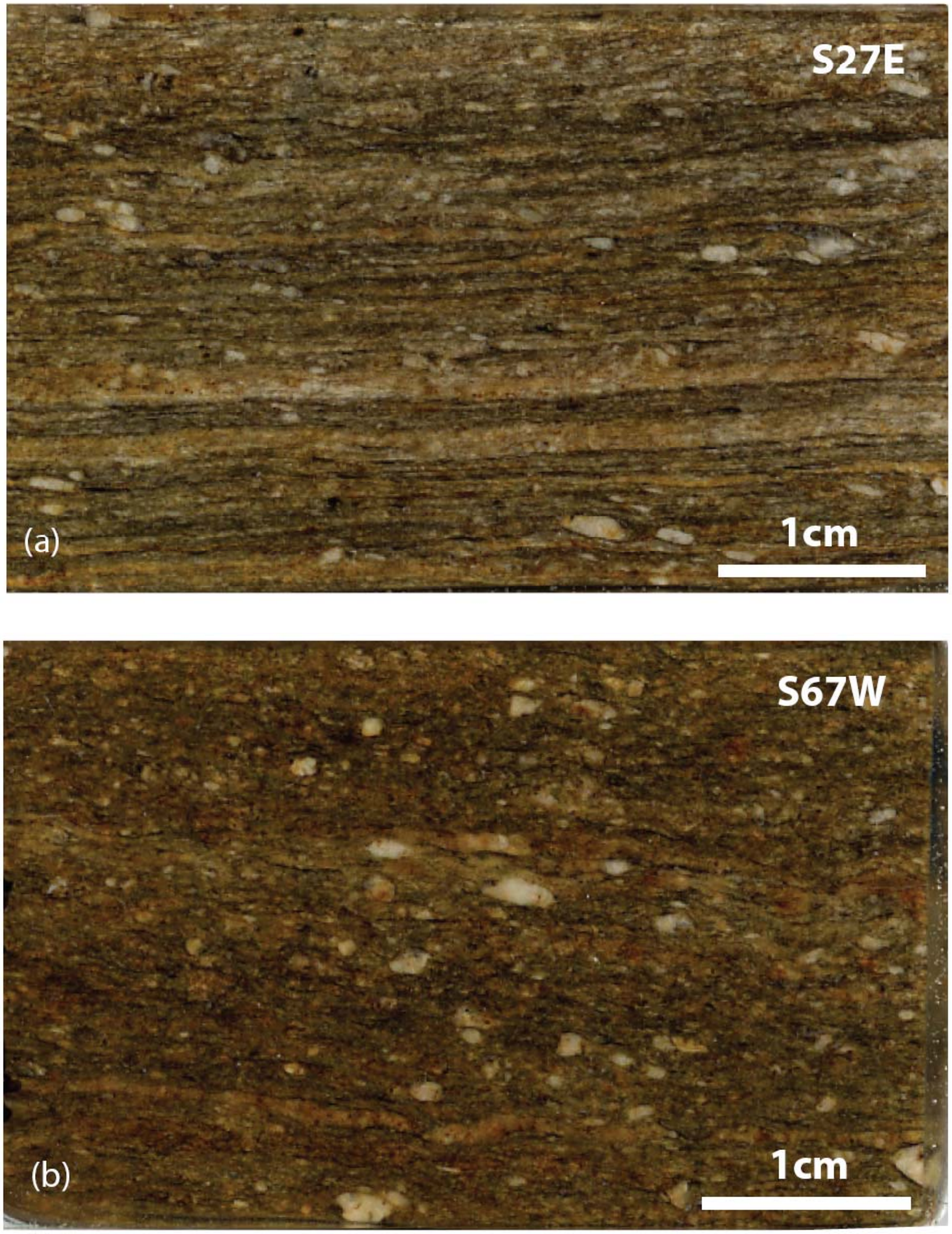

Figure 1-7. Scanned rock chips. Feldspar porphyroclasts in the fine-grained matrices of MHG. Samples were collected from US-76, Whetstone quadrangle, SC (N 34^{o} 45.395’, W 083^{o} 14.366’). Oriented samples (a) and (b) illustrate the banded texture parallel and perpendicular to mineral lineation, respectively.

CHAPTER II

METHODOLOGY

KINEMATIC VORTICITY

Originally, vorticity was defined as an “axial vector” (Truesdell, 1954), quantifying the simultaneous relationships of rotational behavior and “strain rate” within a fluid (Means et al., 1980); vorticity vector is a resultant with respect to rotational center within a system. In high-strain shear zones, for instance, deformation is dominated by ductile behavior; these rigid bodies within the flow matrices spin with respect to vorticity axes (Fig. 2-1). Truesdell (1954) introduced a term kinematic vorticity number (W_k), condensing the relationship of rotation and principal stretch tensors as a constant value, and this fundamental parameter has been used to study kinematics in structural geology and tectonics (McKenzie, 1979; Means et al., 1980).

Kinematic Vorticity Number (W_k) and Mean Kinematic Vorticity Number (W_m)

Truesdell (1954) invented the W_k, which is used to estimate a fluid velocity **v** varying in flowing 3D space. W_k can be defined as a ratio of the rotation and stretch tensors. In terms of rotating behavior, curl **v** is used to describe the vector field in a 3D flowing matrix that is equal to vorticity vector **w**. However, in natural systems, the rate of deformation may change because of temporal and

Figure 2-1. Schematic illustration of the evolution of a rigid body (a) in forward rotation with sinistral shear direction in a ductile matrix; (b) the same rigid grain continues rotating motion, and (c) deforming processes ceased, with the rigid body in the final position. Black arrows in (a) and (b) indicate hypothetical stress along X-axis coordinate system. Gray arrows in (a) and (b) represent hypothetical stress along Y-axis coordinate system. Red and blue arrows indicate coaxial and non-coaxial shear, respectively.

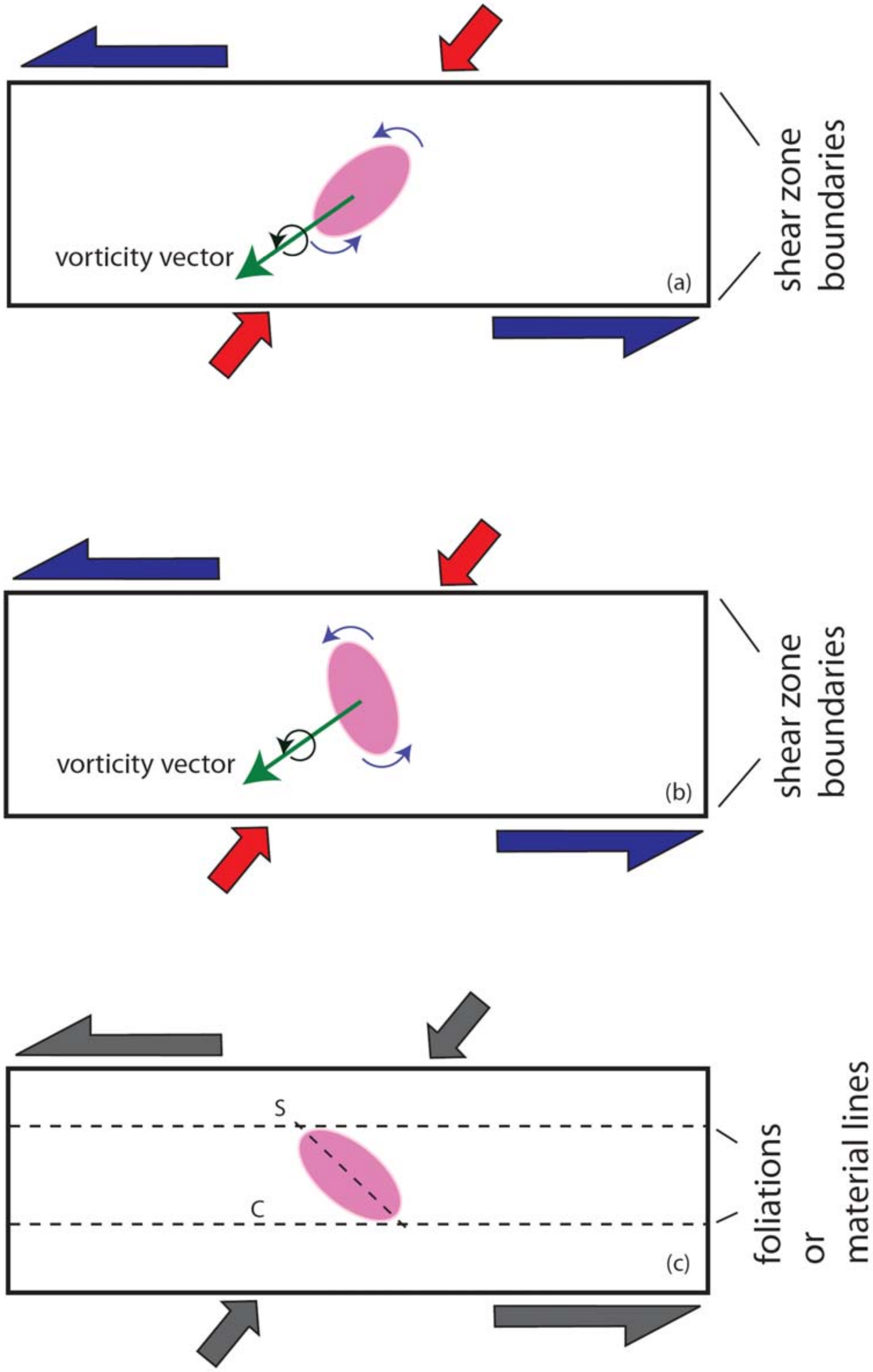
vorticity vector
(a)
shear zone boundaries
vorticity vector
(b)
shear zone boundaries
S
C
(c)
foliations or material lines

spatial variations. Hence, using the term “mean kinematic vorticity” W_m is more realistic to represent the progressive deformation history under these conditions (Means et al., 1980; Passchier, 1987, 1988).

MATHEMATICAL BACKGROUND

Genetically, vorticity is widely discussed in mathematics and broadly applied in engineering. It is worth reviewing the fundamental concepts and mathematical derivations.

In a flowing field, assuming a condition without fluid loss and no adjacent rigid body interference, assume the fluid moves counterclockwise with an angular speed (ω). The term, **v**, represents the velocity field of the 2D flow matrix. Vorticity vector **w** equals curl **v**, in which the vector differential operator (∇) is expressed in Equation 2-1

$$\mathbf{w} = \text{curl}\ \mathbf{v} = \boldsymbol{\nabla} \times \mathbf{v} = \begin{vmatrix} \mathbf{i} & \mathbf{j} & \mathbf{k} \\ \frac{\partial}{\partial x} & \frac{\partial}{\partial y} & \frac{\partial}{\partial z} \\ -\omega y & \omega x & 0 \end{vmatrix} = \left(\omega \frac{\partial x}{\partial x} + \omega \frac{\partial y}{\partial y}\right)\mathbf{k} = 2\omega\mathbf{k} \qquad [2\text{-}1]$$

where **i**, **j**, and **k** are unit vectors in the directions of the positive x, y, and z axes. If the analysis is expanded into a 3D system, the **v** of a uniform rotation about the z-axis can also be expressed as

$$\mathbf{v}\,(x, y, z) = -\omega y\mathbf{i} + \omega x\mathbf{j} \qquad [2\text{-}2]$$

The angular velocity vector (***ω***) thus can be described as

$$\boldsymbol{\omega} = \omega\mathbf{k} \qquad [2\text{-}3]$$

Combining Equations 2-1, 2-2, and 2-3 the relationship among **w**, $\boldsymbol{\omega}$, and curl **v** can be described as

$$\mathbf{w} = 2\,\boldsymbol{\omega} = \text{curl}\,\mathbf{v} \qquad [2\text{-}4]$$

Equation 2-4 illustrates that the angular velocity vector is half of the vorticity vector. Stretch tensor $\dot{\mathbf{S}}$ can be decomposed into the stretching rates in the 3D (*x*, *y*, and z-axes) system; they are $\dot{s}_x$, $\dot{s}_y$, and $\dot{s}_z$, which are the eigenvalues of $\dot{\mathbf{S}}$. Then, W_m is defined as (Truesdell, 1954):

$$W_m = \frac{\mathbf{w}}{\sqrt{2\left(\dot{s}_x^2+\dot{s}_y^2+\dot{s}_z^2\right)}} = \frac{2\boldsymbol{\omega}}{\sqrt{2\left(\dot{s}_x^2+\dot{s}_y^2+\dot{s}_z^2\right)}} \qquad [2\text{-}5]$$

As stated above, the rotating motion with respect to the z-axis, produces zero stretching along the z-axis; hence, $\dot{s}_z$ may be discarded. Equation 2-5 can be rewritten for a 2D condition as (Truesdell, 1954; Passchier, 1987, 1988)

$$W_m = \frac{\mathbf{w}}{\sqrt{2\left(\dot{s}_x^2+\dot{s}_y^2\right)}} \qquad [2\text{-}6]$$

Since the units on both the denominator and numerator cancel, W_m becomes a dimensionless term. In a deformed system without rotation, **w** is zero; hence, $W_m = 0$. The deformation system is dominated exclusively by pure shear. On the other hand, $W_m = 1$ when the value of **w** is equal to $\dot{\mathbf{S}}$, which indicates the deformation is dominated by simple shear.

In geologic kinematic analysis, W_m lies somewhere between zero and 1.0, which is termed general shear. A third possible situation is a pulsating condition, in which $W_m \rightarrow \infty$ (Truesdell, 1954). This situation commonly occurs in spherical rigid bodies ($R = 1$) and no additional shear direction information would be provided by these rigid grains.

Eigenvectors (ε) and Instantaneous Stretching Axis (ISA)

In a shear zone, pure and simple shear coexist during deformation. The eigenvectors are treated as a resultant of pure and simple shear in 2D (Bobyarchick, 1986). One eigenvector ($\boldsymbol{\varepsilon}_1$) lies in the dominant foliation, and another eigenvector ($\boldsymbol{\varepsilon}_2$) varies by the petrofabric variables. For instance, in an outcrop with S-C or S-C' fabric, shear–sense foliations are treated as $\boldsymbol{\varepsilon}_1$ and mineral lineation orientation is regarded as $\boldsymbol{\varepsilon}_2$. The angle ($\alpha$) between $\boldsymbol{\varepsilon}_1$ and $\boldsymbol{\varepsilon}_2$ is attributed to pure and simple shear (Fig. 2-2). The angular relationship can be expressed in terms of a trigonometric function (Equation 2-7) (Bobyarchick, 1986). Notice that W_m conceptually is a representative mean value in terms of a large–scale pattern, not an average value.

$$W_m = \cos\alpha \qquad [2\text{-}7]$$

During rotation, two orthogonal lines are fixed as instantaneous stretching axes in positive and negative stretching directions where a rigid object

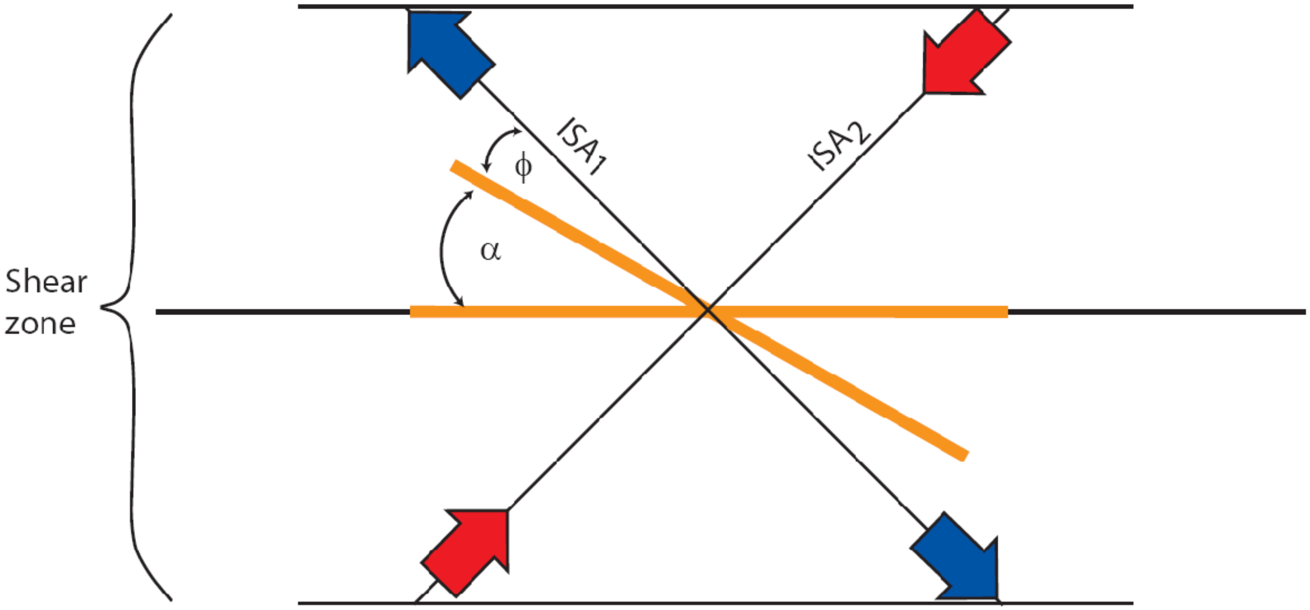

Figure 2-2. Relationship of ISA and $\boldsymbol{\varepsilon}$, and the angles α and ϕ with respect to the shear zone boundaries. Blue arrows at shear zone boundaries indicate simple shear. Red arrows represent pure shear. Orange lines indicate two eigenvectors; one eigenvector parallels the shear zone boundaries, another is aligned parallel to flow apophyses. α is the angle between two eigenvectors. ϕ is the angle between an eigenvector and ISA_1.

is rotating (Means et al., 1980; Bobyarchick, 1986; Passchier, 1987, 1988).This principle is not limited to rocks with porphyroclasts; it also can be applied to the case of quartz grain boundary rotation. Wallis (1992, 1995) suggested that ISAs align parallel to the oblique foliation (Passchier, 1987; Wallis, 1992, 1995). The relationship between ISA and $\boldsymbol{\varepsilon}$ can be expressed as Equation 2-8, where ϕ indicates the angle between the oblique foliation and the dominant foliation

$$W_m = \cos\alpha = \sin 2\,\phi \qquad [2\text{-}8]$$

Grain Shape Effect (B*) and Aspect Ratio (R)

The ISA and $\boldsymbol{\varepsilon}$ of porphyroclasts are more complicated to define because shape and aspect ratio of rigid grains could have affected the final position angle (θ) with respect to foliation ($\boldsymbol{\varepsilon}_1$). Because the $\boldsymbol{\varepsilon}_2$ varies with individual grains, Equations 2-7 and 2-8 are not satisfied to use for rigid grain rotation kinematic studies. However, the ISA remains orthogonal and is fixed to the long (ISA_1) and short (ISA_2) axes of individual grains. The final positions of these rigid grains are the result of the vorticity vector **w**; and they would be terminated at a stable angle with respect to foliation ($\boldsymbol{\varepsilon}_2$), which is related to grain shape.

B^* is a constant term describing rotational motion of particles specifically with low Reynolds numbers (i.e., laminar flow) (Bretherton, 1962), and R is aspect ratio (Wallis, 1995). Hence, B^*, R, and θ with respect to foliation provide indicators of kinematic mechanism during non-coaxial progressive deformation. The θ angle, in fact, is similar to α, yet, the variation of B^* and R of individual grains would generate noisy data, yielding a wide range of θ values. Hence, the concept of the "critical threshold" is adopted to sort out the W_m value (Passchier, 1987; Wallis, 1995; Jessup et al., 2007). Elongate rigid bodies, for example, in an unstable position would be rotated (either forward or backward) within a flowing matrix, and they would be stabilized at the final positions if there is sufficient simple shear (Passchier, 1987, 1988). For instance, an elongate grain would have a lower critical threshold angle (θ_c) in response to a non-coaxial shear system. A rounded grain (R = 1), on the other hand, would be rotated infinitely, and the critical threshold angle cannot be defined. For instance, garnets cannot be used as indicators for the study of rigid grain rotation behavior.

Assumptions Related to W_m: Monoclinic vs. Triclinic Deformation

Conventionally, monoclinic deformation is assumed to be an end-member condition in kinematic vorticity analysis (Passchier, 1987, 1988; Law, 1990), and W_m analysis is limited to 2D (Tikoff and Fossen, 1995). Mineral lineation is assumed to result from maximum stretching during progressive non-coaxial, monoclinic deformation. Almost all W_m values are estimated from the XZ-plane in thin sections, which are cut parallel to lineation and perpendicular to the dominant foliation. However, monoclinic deformation does not always occur on a crustal scale. Triclinic deformation probably occurs during simple-shear deformation, or as an end-member of a tectonic event (Lin et al., 1998; Williams et al., 2006). Both monoclinic and triclinic shear systems may have similar 2D patterns in the XZ section (Fig. 2-3). A slight change between two miniature shear boundaries (foliations) may not be easily identified, although the cumulative results of these subtle changes could be essential evidence of 3D triclinic deformation. To envision deforming regimes in 3D, it is worthwhile to investigate those sections perpendicular and oblique to lineation and foliation (Forte and Bailey, 2007) (Fig. 2-4). It is still plausible, however, to treat each thin section as a monoclinic deformation system when comparing to crustal-scale deformation.

For instance, a parabolic curve can be divided into infinitesimal segments, with each individual segment being a very small straight line. In terms of crustal scale, each thin section contains an incremental segment of the overall deformation process. The cumulative results, in fact, provide a useful scale of triclinic geometry. Thus, the tectonic interpretation of W_m should be based on the trend of W_m values along the shear zone on sections both parallel and perpendicular to lineation.

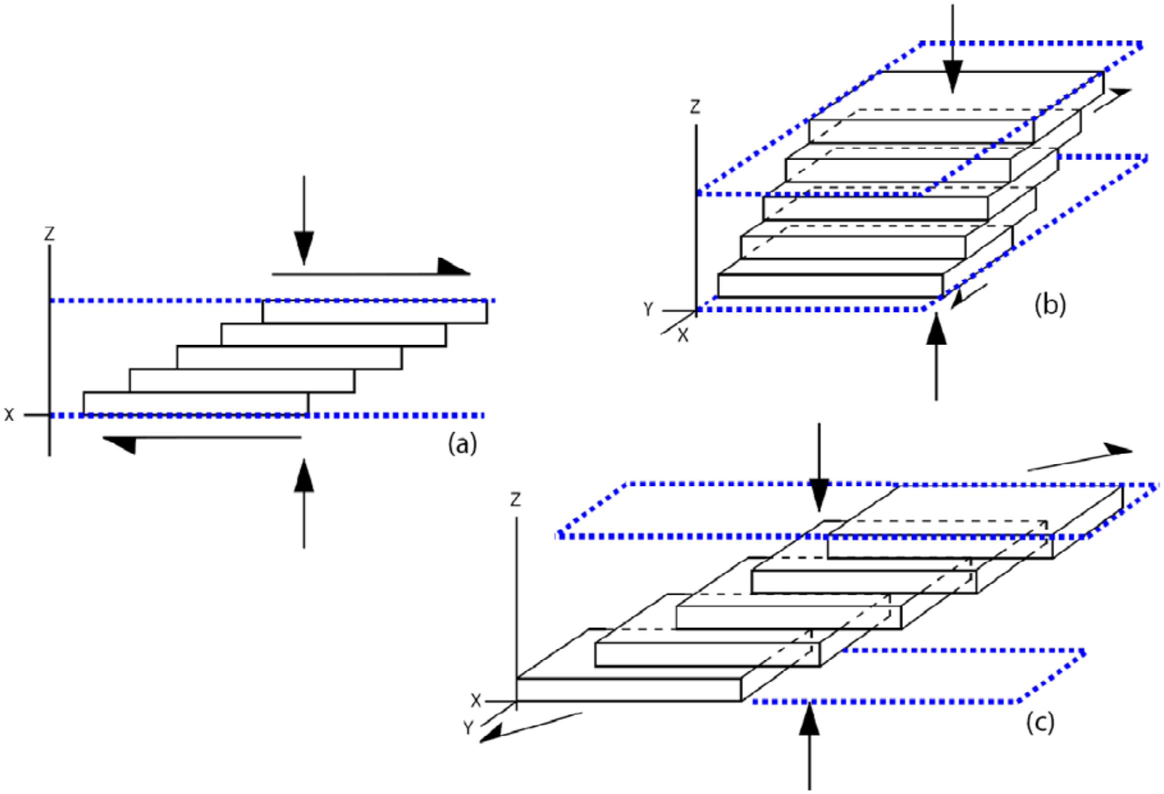

Figure 2-3. Monoclinic deformation in 2D (a) can be reproduced by 3D monoclinic (b) and (c) triclinic shear systems. Blue dashed-line region represents shear zone boundaries. X and Z axes are the relative coordinates with respect to thin section orientation.

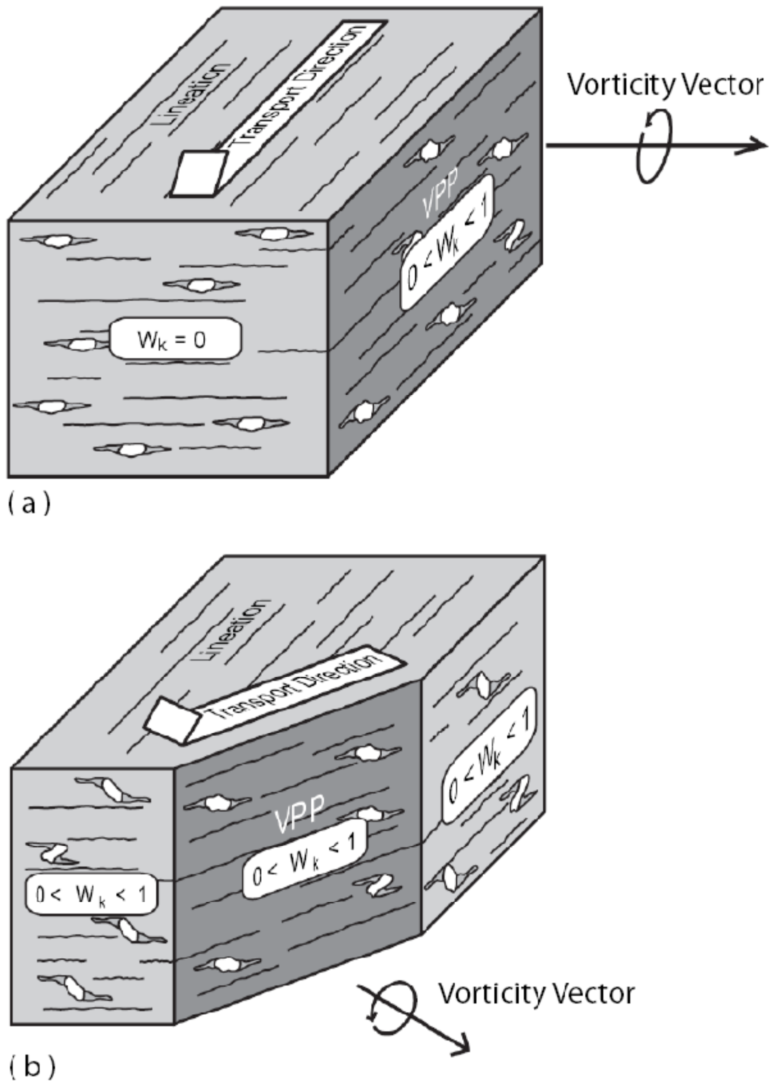

Figure 2-4. Monoclinic (a) deformation vs. triclinic (b) deformation. (a) Monoclinic deformation gives a $W_m = 0$ in the section perpendicular to lineation. (b) Possible W_m range if it is a result of triclinic deformation. VPP: vorticity profile plane (from Forte and Bailey, 2007).

Techniques of W_m Measurement

Numerous methods have been suggested to estimate W_m, based on geologic scales, deformation, and strain markers. The methods include: 1) rotated porphyroclast behavior analysis; 2) lattice-preferred orientation (LPO); 3) vein-set analysis; 4) rotated porphyroblast behavior gauges; 5) tension gashes and foliation in shear zones; and 6) oblique foliation (Ramberg, 1975; Ramsay and Huber, 1983; Passchier and Trouw, 2005). Two methods were used in this study: behavior of rigid bodies rotating to determine W_m and crystallographic fabric orientation.

Rigid Grain Net (RGN) Method

With a sufficient sample size and a clear pattern, the orientation of each rigid grain within a rock matrix may be seen as a snapshot, resulting from progressive deformation (Passchier and Trouw, 2005). Each snapshot records different increments of flow history; thus the rigid-grain method can be utilized to study the kinematic framework of the shear zone. In rotated porphyroclast analysis, measurement is made of rotational behavior in a flowing rock mass associated with grain shape. The ratio of long to short axes, R, represents the tendency of rigid bodies to be rotated. For instance, during non-coaxial deformation, a rounded grain is likely to rotate in perpetuity with an $R = 1$ (i.e., in an unstable position). Elongate grains, on the other hand, are most likely to attain a stable position with $R > 1$.

The rotating behavior of porphyroclasts can be described as (Passchier, 1987).

$$B^* = \frac{M_L^2 - M_S^2}{M_L^2 + M_S^2} \qquad [2\text{-}9]$$

$$R = \frac{M_L}{M_S} \qquad [2\text{-}10]$$

$$\theta = \frac{1}{2}\sin^{-1}\frac{W_m}{B^*}\left(\sqrt{1 - W_m^2} - \sqrt{B^{*2} - W_m^2}\right) \qquad [2\text{-}11]$$

B^* represents the grain shape factor. M_L and M_S are lengths of long and short axes of individual grains, respectively, and θ represents the angle in degrees between the long axes and foliation. For tailless porphyroclasts, the angles are measured between long axes and the dominant foliation.

Several techniques may be used to estimate W_m, including the Passchier plot (Passchier, 1987), the porphyroclast hyperbolic distribution (PHD) plot (de Paor, 1988; Simpson and de Paor, 1993, 1997), and the Wallis plot (Wallis, 1995). Jessup et al. (2007) developed the rigid grain net (RGN) technique, modifying the above techniques, to estimate W_m. The RGN technique facilitates data analysis and reduces the ambiguity of W_m estimates. In the following section, selected samples were plotted and compared, using the RGN and Wallis methods.

In this study, W_m was determined in samples of Alleghanian retrograde MHG. Two sets of variables were measured in rotated porphyroclasts in flowing matrices: 1) lengths of the long (M_L) and short (M_S) axes; and 2) the angle (θ)

between long axes and foliation (Figs. 2-5). These parameters were recorded in an Excel spreadsheet to produce an RGN plot (Fig. 2-6). Conventionally, W_m values were determined by an arbitrary value at the positive and negative angles that may sacrifice significance of the measurements. So, W_m should be defined by a range at the positive and negative angles; it could also accommodate some measuring errors (M. J. Jessup per. comm.). Overall, the study is expected to yield information that can be used to test the existing tectonic models for the BFZ as well as to better understand its greenschist facies deformation pattern.

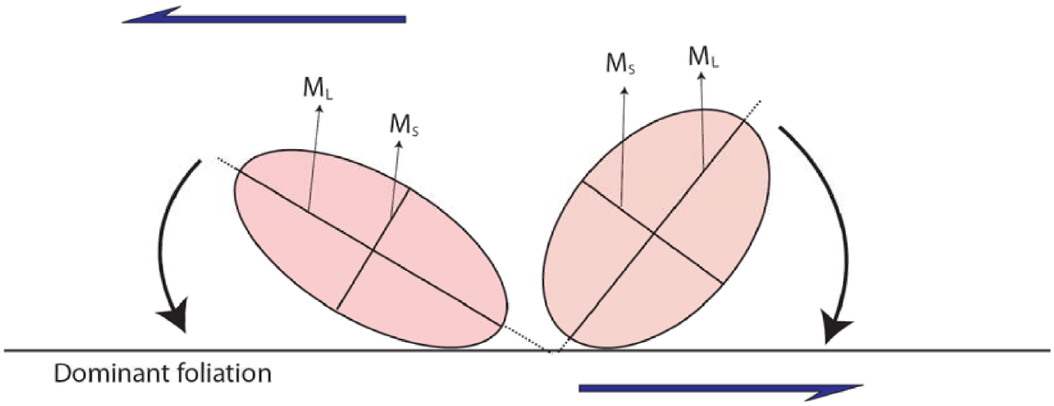

Figure 2-5. Schematics of rigid bodies in a hypothetical flow matrix with a sinistral stretching direction. M_L, M_s, and θ were measured. Shear sense in blue arrows represents top-to-the-left.

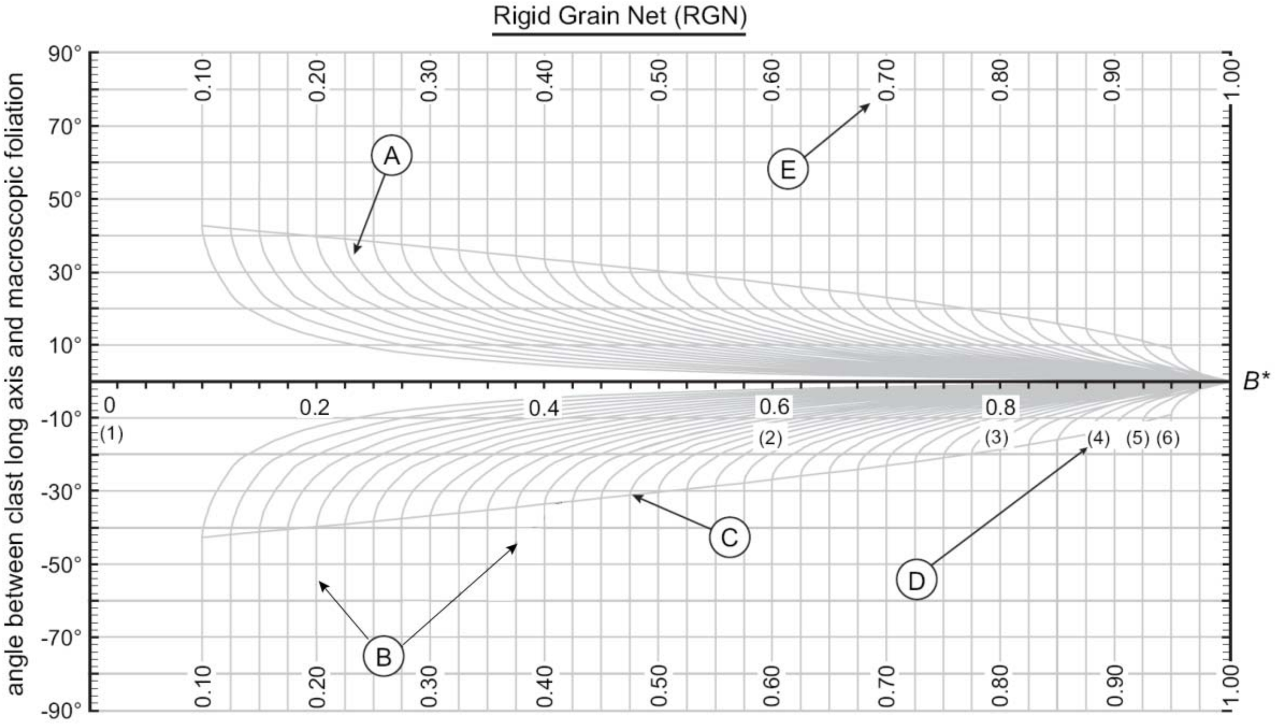

Figure 2-6. An example of an RGN plot; five regions A, B, C, D, and E are explained as following. A: Semi-hyperbola curve represents the relationship between θ and B^*. B: Vertical segments of curves illustrate the R-value at which rotating θ of rigid bodies > θ_c. C: Critical aspect ratio (R_c) when $W_m = B^*$. D: R, in parentheses. E: W_m for semi-hyperbolae. (From Jessup et al., 2007).

Nikon Image System (NIS)

To improve data credibility, real time images were connected to software (NIS-Element BR) that amplifies the image of rigid grains on the computer screen. Photomicrographs of mineral clasts can be captured and preserved, helping to double check measurements later. A digital rectangular box was used to match the M_L and M_S; the length and width of the rectangular box generated by software NIS-Element BR were recorded with respect to M_L and M_S . A reference line was also set up parallel to dominant foliation prior to measure the θ angle (Fig. 2-7).

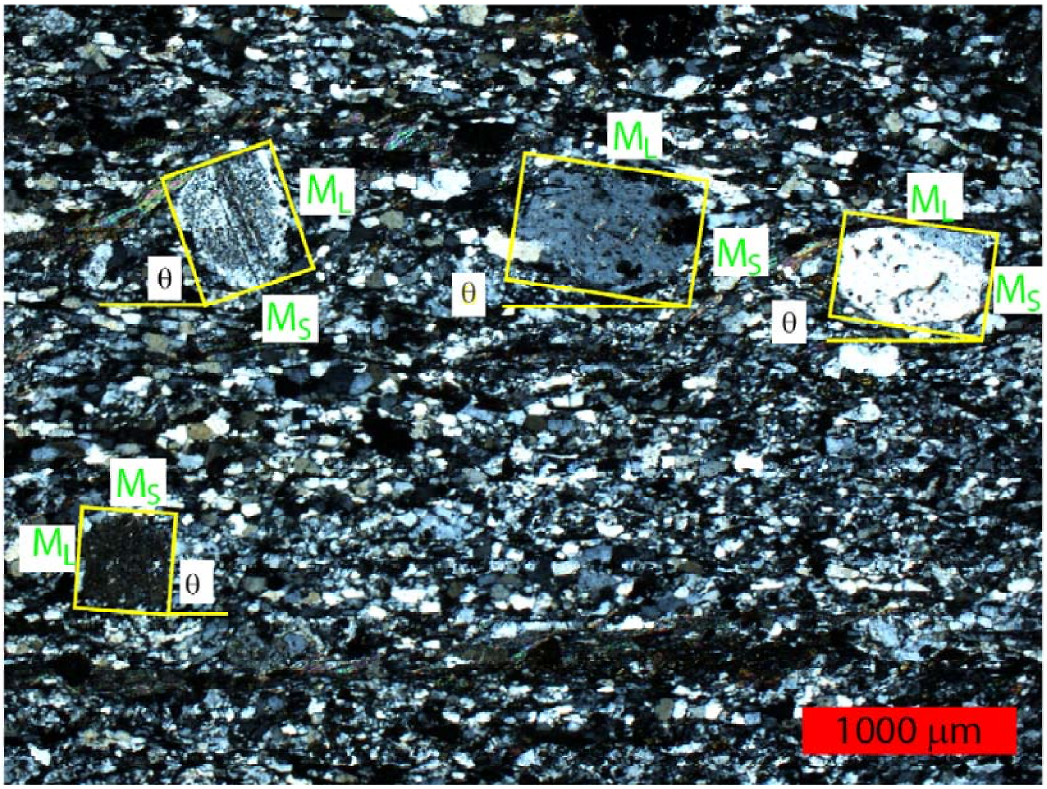

Figure 2-7. Photomicrograph of MHG (crossed polars) sample WS-017-I (from Blackwell Bridge, Chauga River, Whetstone quadrangle, SC). The porphyroclasts are plagioclase; fine-grained matrix is mainly composed of annealed quartz and muscovite, and minor twinned plagioclase. Parameters: M_L, M_S, and θ were measured.

Quartz *C*-axis Analysis

Crystallographic fabrics have been confirmed as a reliable tool to study sheared rocks (Lister and Williams, 1979, 1983; Lister and Hobbs, 1980), and they have been widely used to study slip systems in quartz (Law, 1986, 1987, 1990; Law et al., 1990, 1992, 2004; Wallis, 1995; Xypolias and Doutsos, 2000). During progressive deformation, crystallographic axes slip in response to strain and temperature, and this deformation is reflected in quartz *c*-axis patterns (Law, 1986, 1987, 1990; Passchier and Trouw, 2005). In general, two possible cross girdles are produced, resulting from deformation (Fig. 2-8) (Law, 1986, 1990; Law et al., 1990; 1992, 2004).

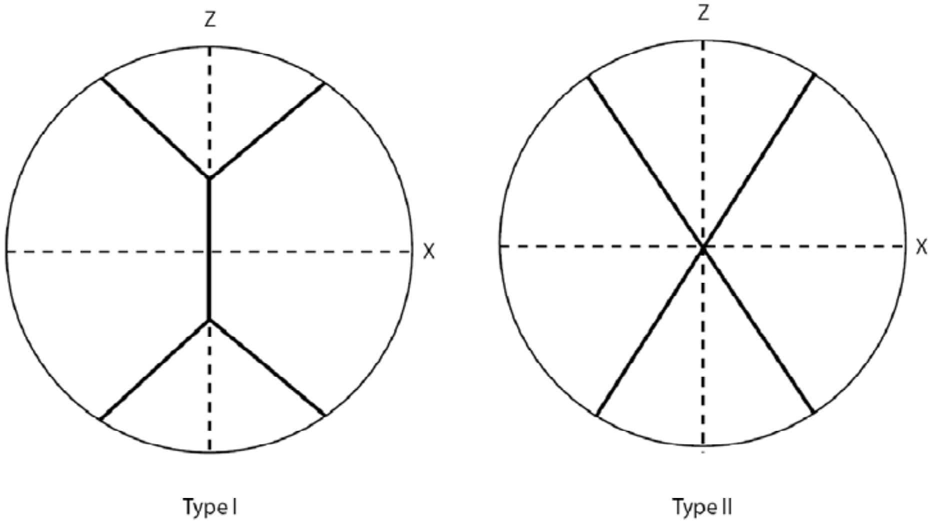

Figure 2-8. Quartz *c*-axis girdle patterns. Types I and II are associated with non-coaxial and coaxial progressive deformation, respectively (after Passchier and Trouw, 2005). Type I and II girdles are the result of non-coaxial and coaxial strain, respectively.

Quartz *c*-axis patterns can be used to determine deformed geometry in terms of internal and external asymmetry (Behrmann and Platt, 1982; Passchier and Trouw, 2005). The external asymmetry is used to resolve shear sense, determined by the angle of inclination (Ψ) of the central girdle with respect to the foliation (Behrmann and Platt, 1982) (Fig. 2-9). As a result, the angle (β) between the normal to central girdle and finite strain flattening plane can be calculated. The internal asymmetry is defined by the angles between the central girdle and limbs (ω_1 and ω_2) (Fig. 2-9).

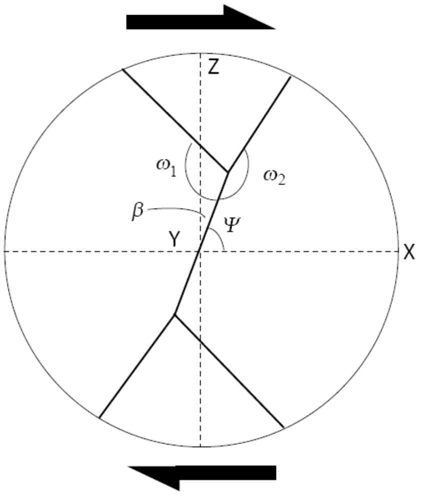

Figure 2-9. Schematic illustration of type-I fabric skeleton with dextral shear sense (after Passchier and Trouw, 2005).

Based on *c*-axis diagrams, there are three types of <*a*> slip systems and one type of c-slip: basal <*a*>, rhomb <*a*>, and prism <*a*>. A well defined basal <*a*> slip system that is related to a low temperature (regime I; Hirth and Tullis, 1992) deformation developed at the limb portion of the *c*-axis diagram. As deformation temperature increases the *c*-axis orientation begins to skew toward the girdle center and *c*-axis angle tends to cluster around the Y-axis. Rhomb <*a*> and prism <*a*> slip systems are associated with low to medium temperature (regime I to II; Hirth and Tullis, 1992). Under high temperature (regime III; Hirth and Tullis, 1992), *c*-axes develop perpendicular to Y-axes, resulting in ***c***-slip systems.

The open angle of the limbs may associate with deformation temperature (Kruhl, 1998; Law et al., 2004). *C*-axis measurements were made from quartz-rich layers and lenses in phyllonite (Fig. 2-10). Trend and plunge of individual quartz *c*-axes were recorded, and then plotted in a lower hemisphere equal-area stereonet. Once the center girdle is constructed, the slip angle (β) can be obtained. Additionally, strain ratio (R_f) can be obtained by a quadratic equation if W_m and β are known (Wallis, 1995).

$$R_f = \frac{-b \pm \sqrt{b^2 - 4ac}}{2a} \qquad [2\text{-}12]$$

Where :

$$a = 2W_m^2 - 2W_m^2 \cos 2\beta - 2sin^2 2\beta \qquad [2\text{-}12\text{-}a]$$

$$b = -2sin^2 2\beta \qquad [2\text{-}12\text{-}b]$$

$$c = 2W_m^2 + 2W_m^2 \cos 2\beta - 2sin^2 2\beta \qquad [2\text{-}12\text{-}c]$$

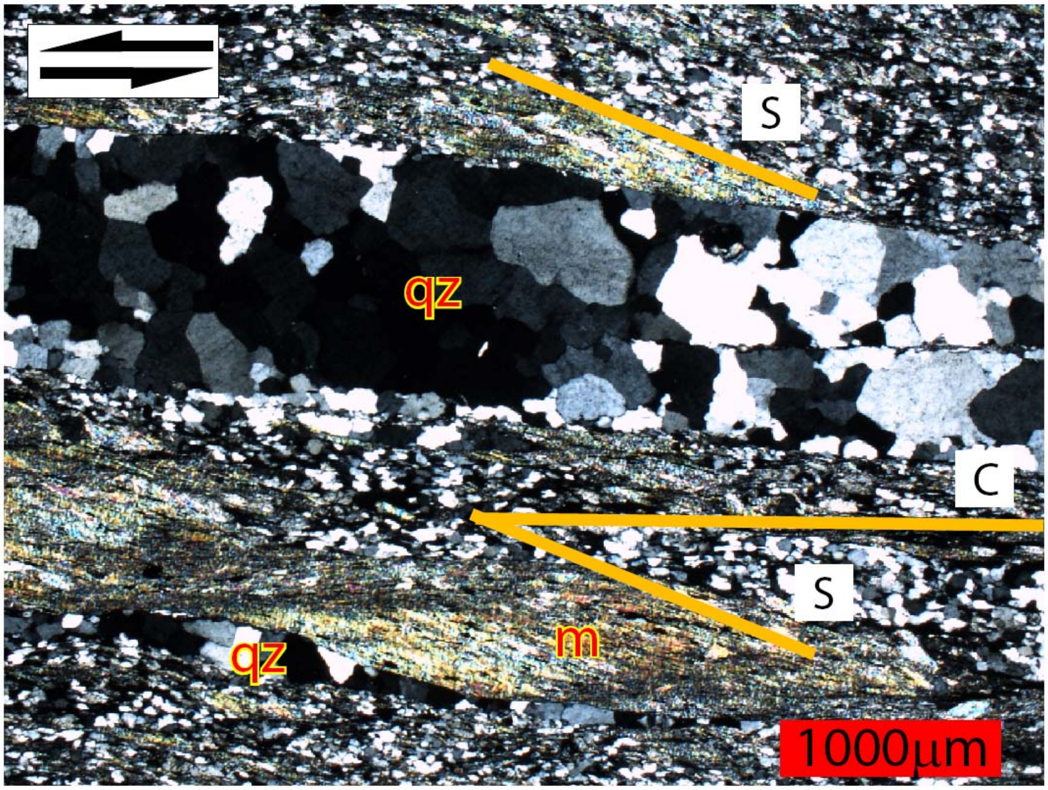

Figure 2-10. Quartz c-axes were measured from quartz bands in phyllonite; annealed quartz and white mica (WS-024-I from Blackwell Bridge, Chauga River, Whetstone quadrangle, SC). qz = quartz; m = muscovite. S-C fabric indicates top-to-the-SW shear sense.

CHAPTER III

SAMPLE LOCATIONS, DESCRIPTIONS AND PRELIMINARY MEASUREMENTS

SAMPLE LOCATIONS

Fifteen oriented samples were collected from 12 localities in NW South Carolina from the best mapped and best exposed segment of the BFZ (Whetstone and Tamassee quadrangles) (Fig. 3-1). Two sets of thin sections were cut: 1) normal to foliation and parallel to lineation; and 2) normal to foliation and lineation.

MYLONITIC HENDERSON GNEISS

Retrograde MHG ranges from coarse porphyroclastic mylonite to ultramylonite, and contains rigid feldspar prophyroclasts in a matrix of annealed quartz and micas. Fault rocks are mostly strongly NE-oriented C-L tectonites. Mineral lineation is subparallel to the dominant C foliation, and plunges gently NE and SW (Fig. 3-2).

Three rock types were collected from the study area: MHG, phyllonite, and MG. Table 3-1 summarizes the rock types, localities, and methods used in kinematic analysis. Modal analyses (Table 3-2) results indicate that MHG contains porphyroclasts within a groundmass composed of K-feldspar, quartz, muscovite, plagioclase (An_{35-45}) (Gatewood, 2007), biotite with accessory

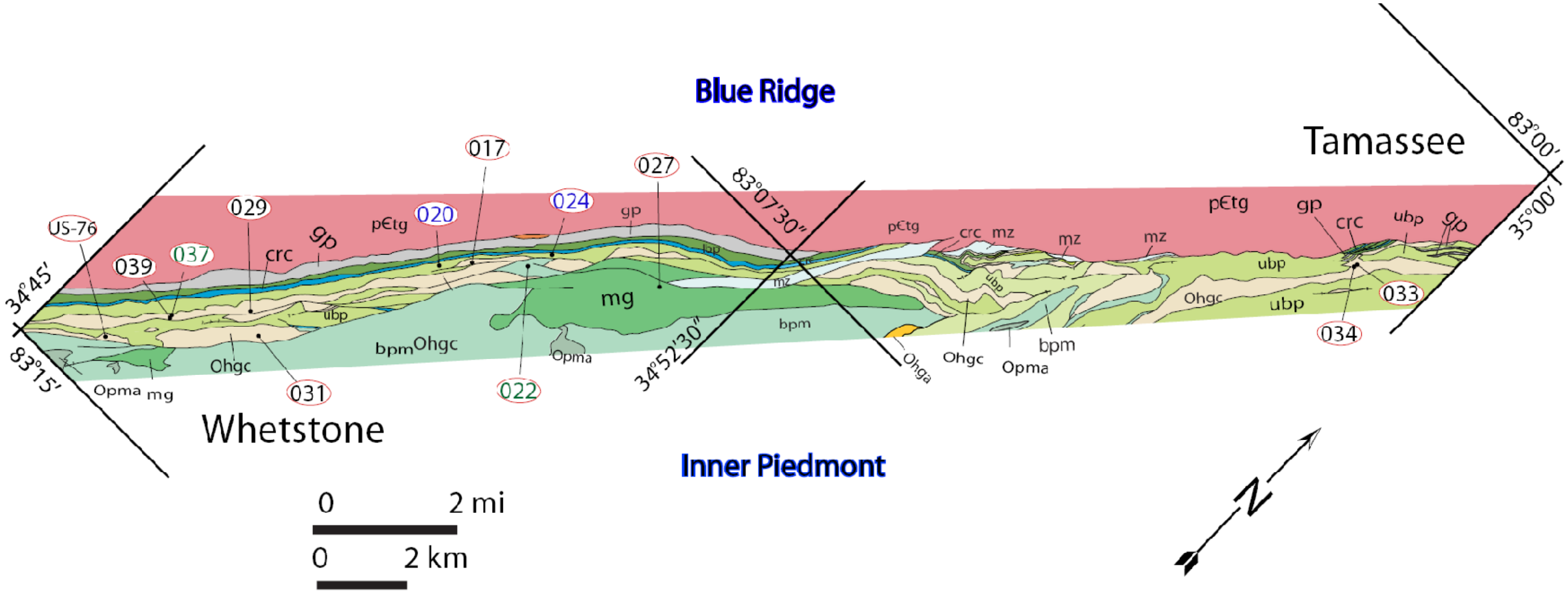

039 : RGN analysis.   024 : quartz c-axis analysis.   022 : RGN and quartz c-axis analyses.

Figure 3-1. Fifteen samples collected from twelve localities. See Figure 1-5 for explanation of map.

Figure 3-2. Photograph from Double Branch, Chauga River, Whetstone quadrangle, SC. Arrow indicates SW plunge of the dominant mineral lineation.

Table 3-1. Sample locations, rock types, and vorticity analyses.

		Sample Localities			Kinematic analyses	
Quadrangle	Sample ID	Latitude (°N)	Longitude (°W)	Rock type	Rigid grain rotation	Quartz *c*-axis analysis
TA –	033	34° 57 '29.0" N	083° 01 '12.5" W	hg	*	
TA –	034	34° 57' 29.0" N	083° 01' 12.5" W	hg	*	
WS –	027	34° 51' 05.4" N	083° 08' 24.8" W	mg	*	
WS –	022	34° 49' 00.9" N	083° 10' 15.6" W	ubp		*
WS –	024	34° 50' 07.4" N	083° 10' 24.9" W	ubp		*
WS –	017	34° 49' 28.9" N	083° 10' 52.9" W	hg	*	
WS –	020	34° 49' 14.3" N	083° 11' 14.8" W	ubp		*
WS –	029	34° 47' 15.5" N	083° 12' 34.0" W	hg	*	
WS –	031	34° 46' 51.6" N	083° 12' 34.9" W	hg	*	
WS –	037	34° 46' 34.5" N	083° 13' 24.9" W	hg	*	*
WS –	039	34° 46' 35.1" N	083° 13' 24.7" W	hg	*	
WS –	US-76	34° 45' 23.7" N	083° 14' 22.0" W	hg	*	

hg: Henderson mylonitic gneiss
mg: mylonite gneiss
qz: interlayered quartzite in Brevard-Poor Mountain (bpm) transitional metasiltstone member
ubp: Chauga River Formation phyllonite
*: different kinematic analyses methods were used on different rocks
TA – Tamassee
WS – Whetstone

Table 3-2. Modal analyses of selected MHG samples (1000 points were counted in all samples).

Samples	TA-0 33	TA-034	WS-017	WS-031	WS-037	WS-039
K-fsp	2.50	2.18		0.80	0.13	0.50
pl	13.80	11.71	10.90	17.40	2.40	2.80
qz	56.30	58.83	62.50	53.60	67.30	74.50
m	25.20	25.10	19.80	23.80	19.36	17.50
biot	2.20	2.18	3.70	4.10	6.54	3.30
ep			2.60	0.10	2.81	0.90
all			0.50		0.93	0.10
opq				0.20		
sph					0.53	0.40
Total	100.00	100.00	100.00	100.00	100.00	100.00

K-fsp: K-feldspar
pl: plagioclase
qz: quartz
m: muscovite
bt: biotite

ep: epidote
all: allanite
opq: opaque
sph: sphene

chlorite, epidote, allanite, sphene, and opaque. Some plagioclase clasts are replaced by sericite. Most myrmekite rimmed K-feldspar porphyroclasts have been retrograded, and they present evidence of earlier high temperature deformation (Fig. 3-3). MG was the only sample containing skeletal garnets and abundant mica fish (Fig. 3-4).

Phyllonite samples are characterized by an almost completely annealed quartz fabric, and a few mineral clasts in the matrices. Quartz is present in ultramylonite as small recrystallized matrix phases (regime III) and ribbons (regime I to II) (Hirth and Tullis, 1992); some contain noticeable undulose extinction, indicative of incomplete annealing or later superposed strain. D_2 deformation (Fig. 3-5) and extensional crenulation cleavage (Fig. 3-6) suggest simple shear deformation. Quartz was deformed by crystal-plastic mechanisms (dislocation glide and climb) (Hirth and Tullis, 1992). Quartz grains consist of medium to coarse grains with clear grain boundaries (Fig. 3-7); these quartz grains display regime III (Hirth and Tullis, 1992) that may have resulted from significant water participation during the deformation. Deformation lamellae are present (Fig. 3-8), which may have formed later (late Alleghanian orogeny), related to brittle deformation.

Figure 3-3. Photomicrograph of myrmekite (crossed polars). (a) and (b) (WS-037-II, from Double Branch, Whetstone quadrangle, SC). (c) and (d) retrograded myrmekite (WS-031-I, from Crooked Creek, Whetstone quadrangle, SC). chl = chlorite; m = muscovite; myr = myrmekite; Ksp = K-feldspar; pl = plagioclase; qz = quartz.

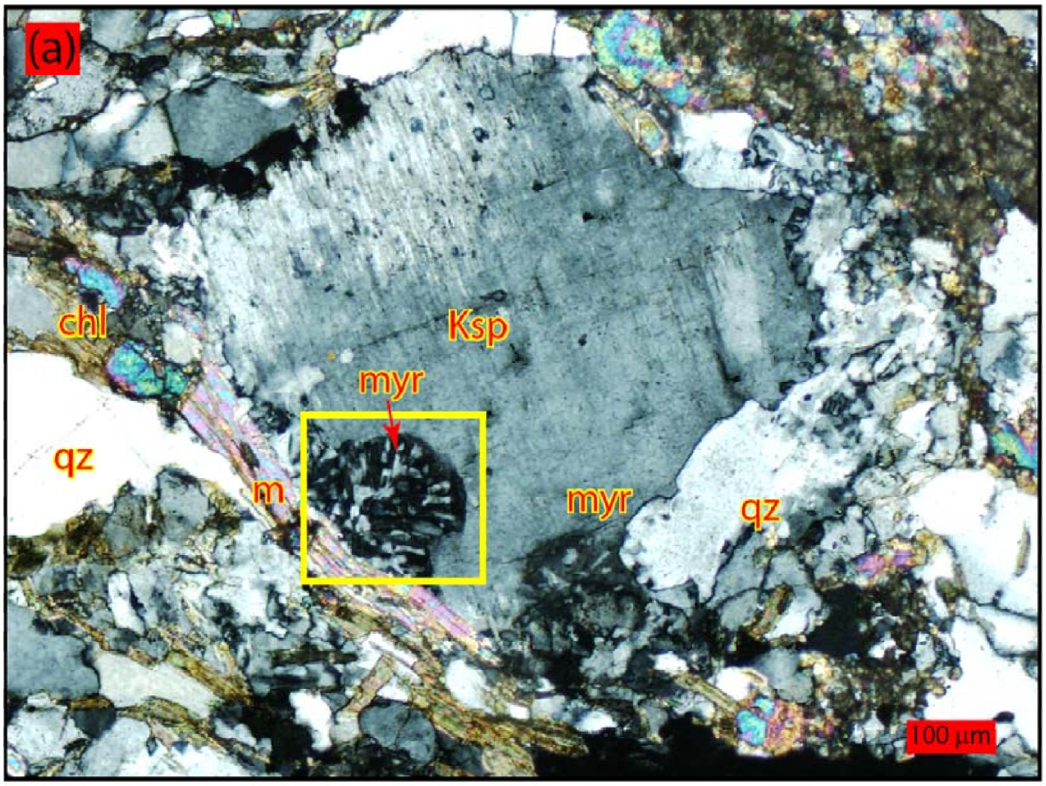
(a)
chl
Ksp
myr
qz
m
myr
qz
100 μm

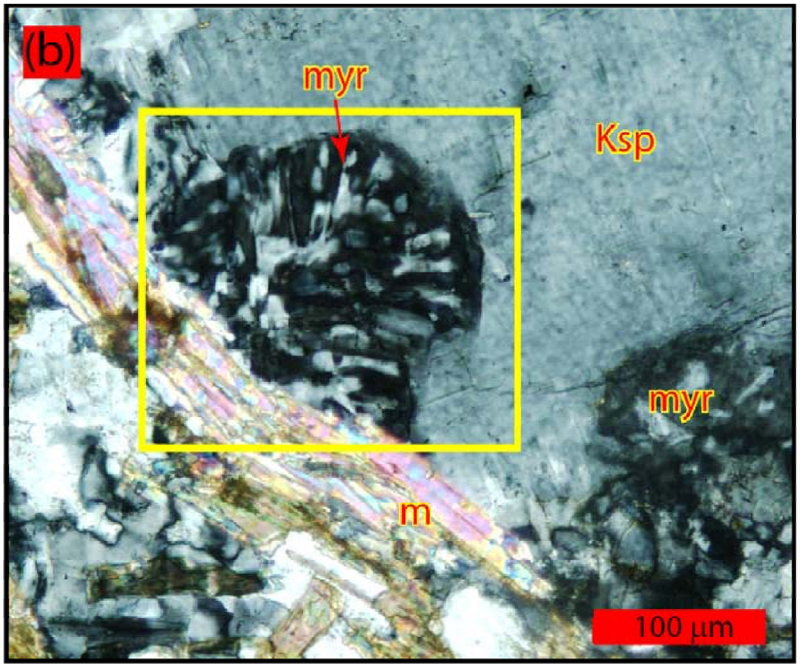
(b)
myr
Ksp
myr
m
100 μm

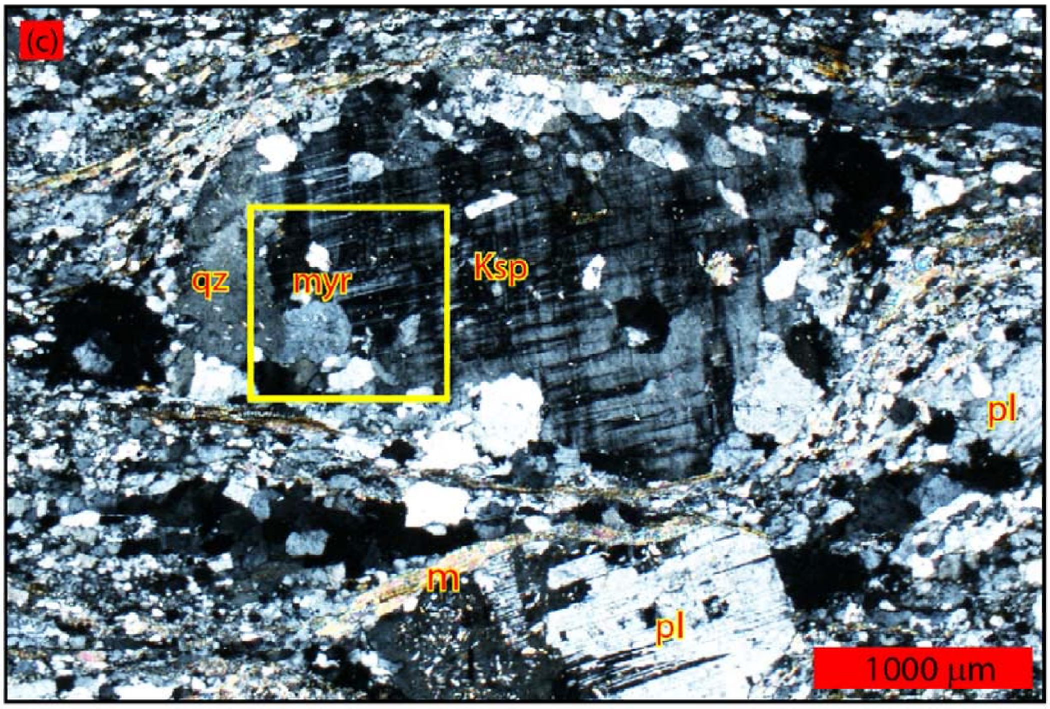
(c)
qz
myr
Ksp
pl
m
pl
1000 µm

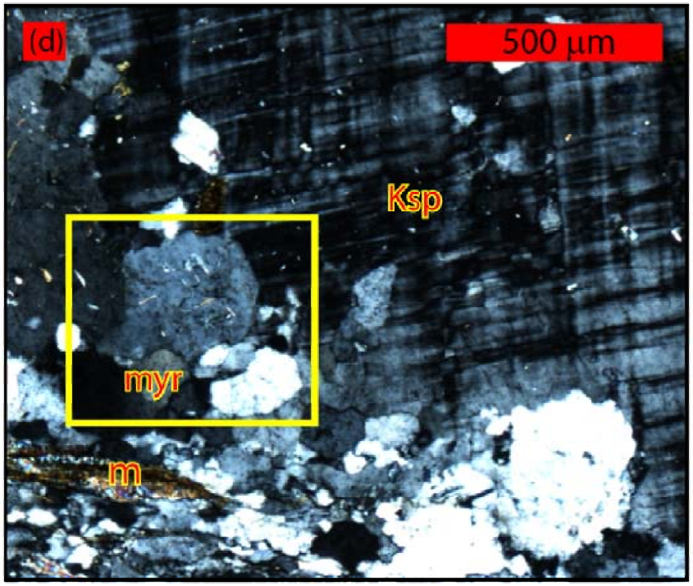
(d)
500 µm
Ksp
myr
m

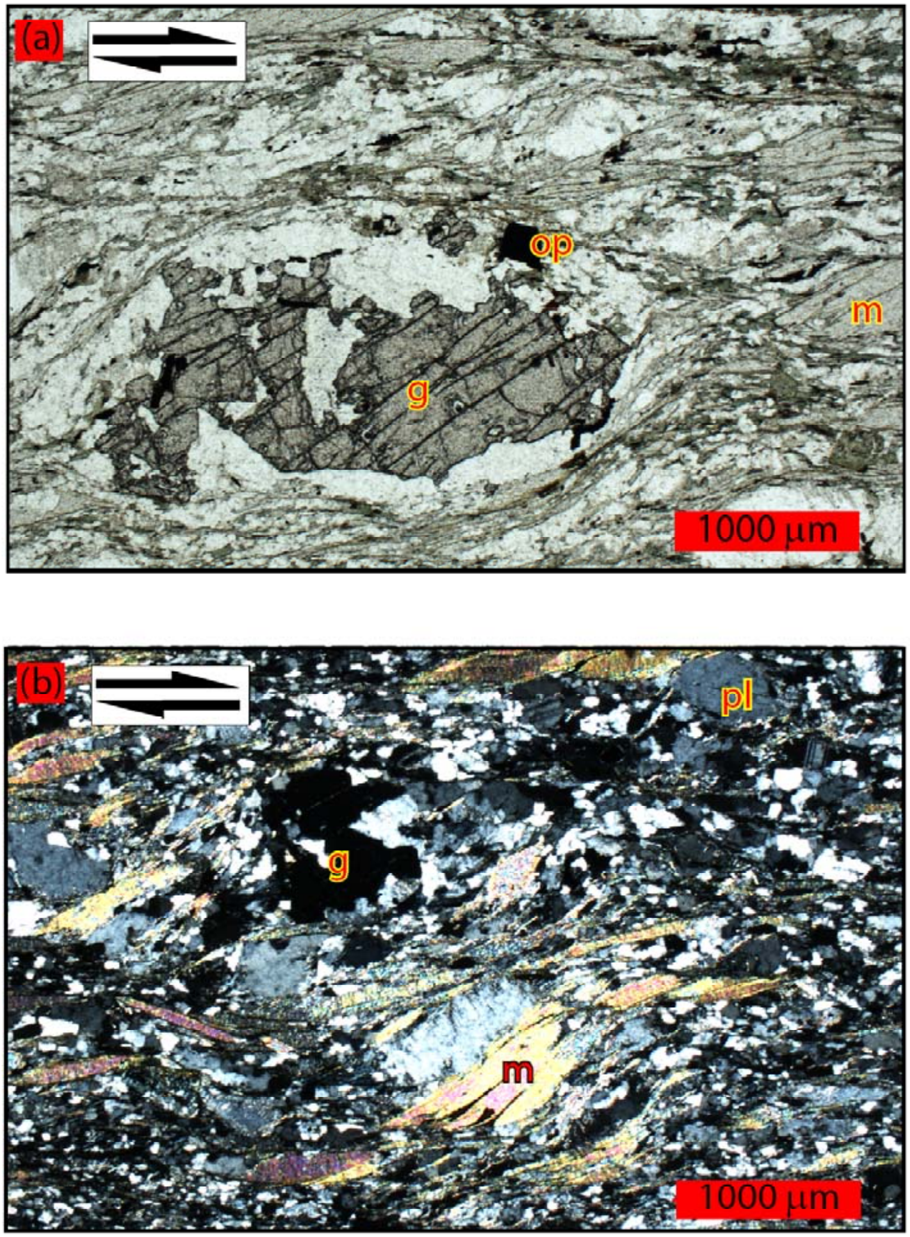

Figure 3-4. Photomicrograph of MG sample WS-027-I from SC 28, Whetstone quadrangle, SC. (a) skeletal garnet in plane light. (b) mica fish in MG (crossed polars). m = mucovite; g = garnet; pl = plagioclase; op = opaque. Shear sense is top-to-the-right.

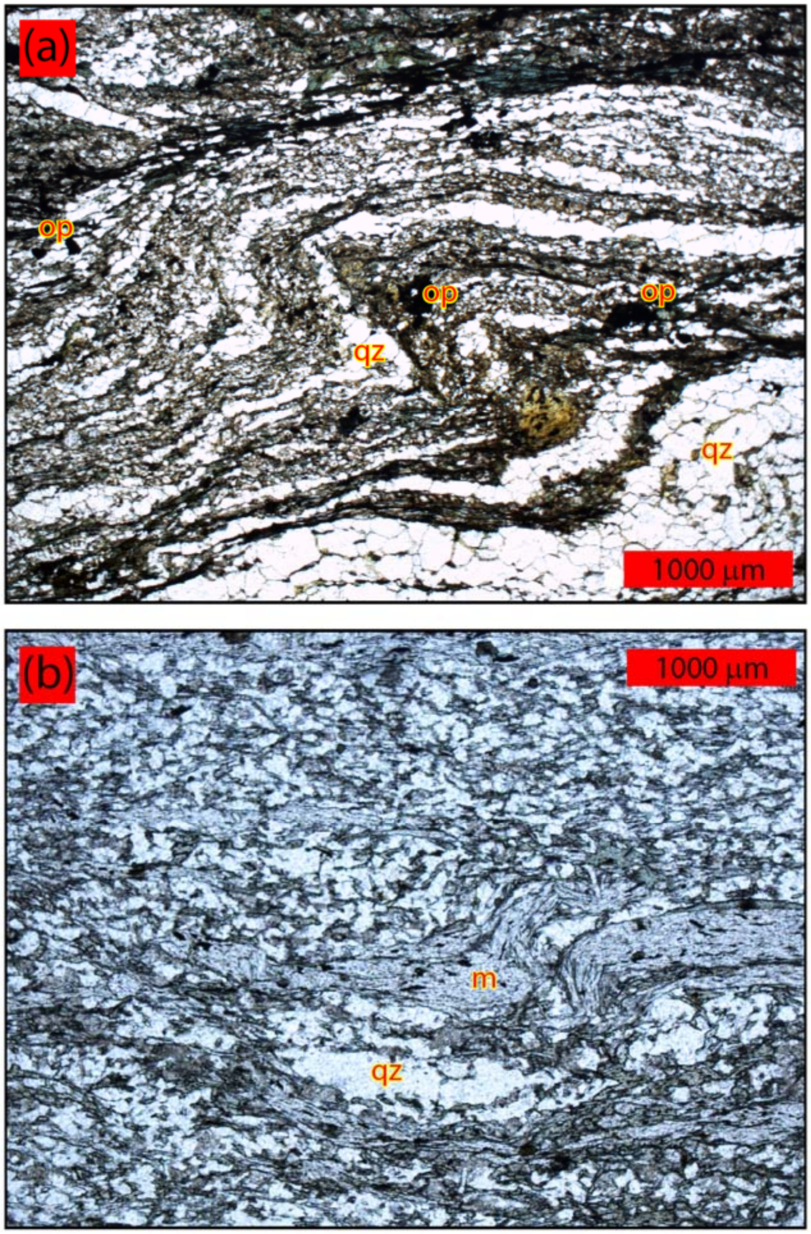

Figure 3-5. Photomicrograph of D_2 folding in plane light of (a) quartz ribbon (WS-020-I from Chauga River, Whetstone quadrangle, SC). (b) Mica and quartz lenses (WS-024-II, from Chauga River, Whetstone quadrangle, SC). m = muscovite; op = opaque mineral; qz = quartz.

Figure 3-6. Recrystallized quartz ribbon in phyllonite (a to d) (WS-020-I from Blackwell Bridge, Chauga River, Whetstone quadrangle, SC). chl = chlorite; m = muscovite; op = opaque mineral; qz = quartz; v= void. Dimensional preferred orientation shows top-to-the-SW sinistral shear sense (a and b). Muscovite extensional crenulation cleavage (green-line) in phyllonite (c and d).

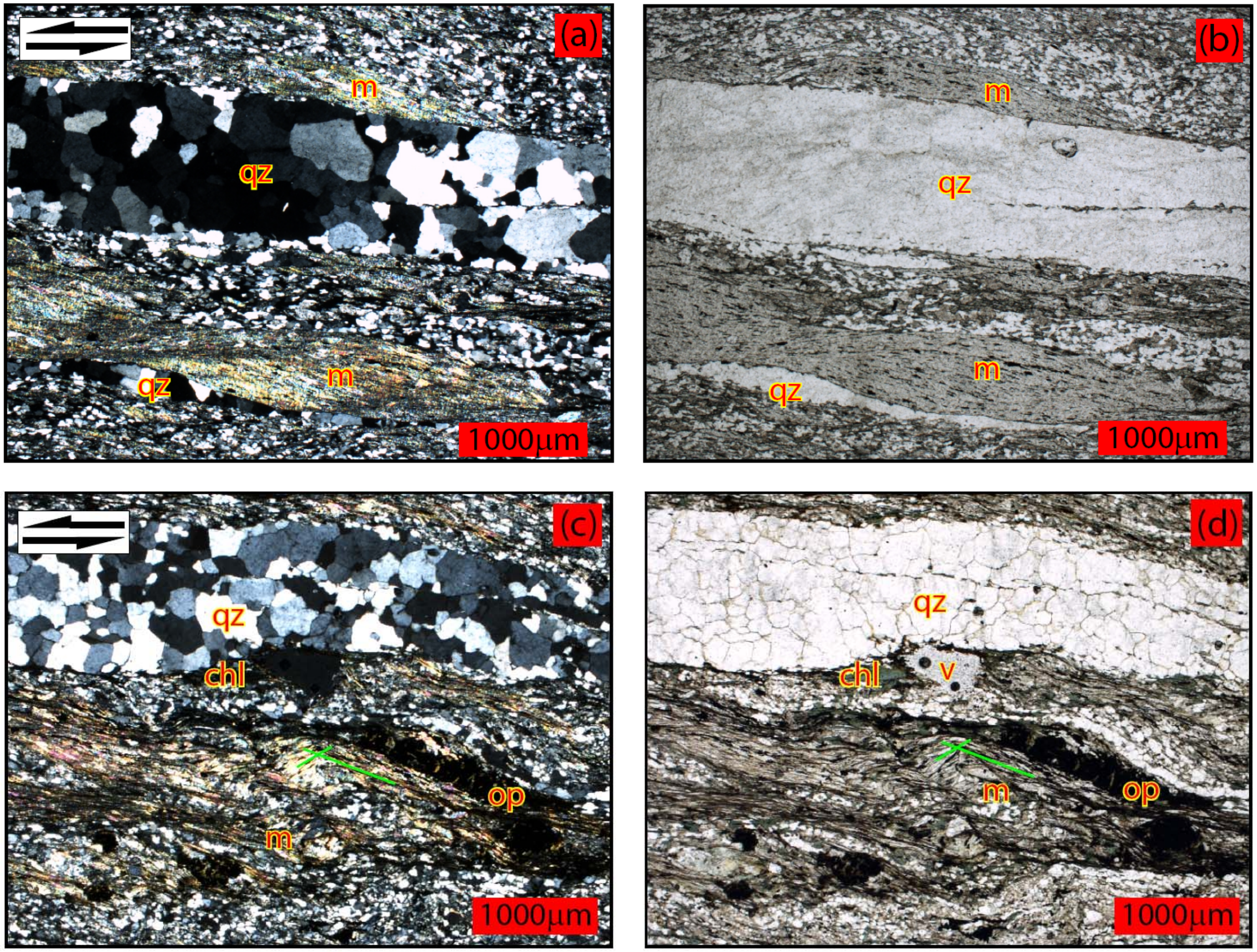
(a)
m
qz
m
qz
1000µm
(b)
m
qz
m
qz
1000µm
(c)
qz
chl
op
m
1000µm
(d)
qz
chl
v
m
op
1000µm

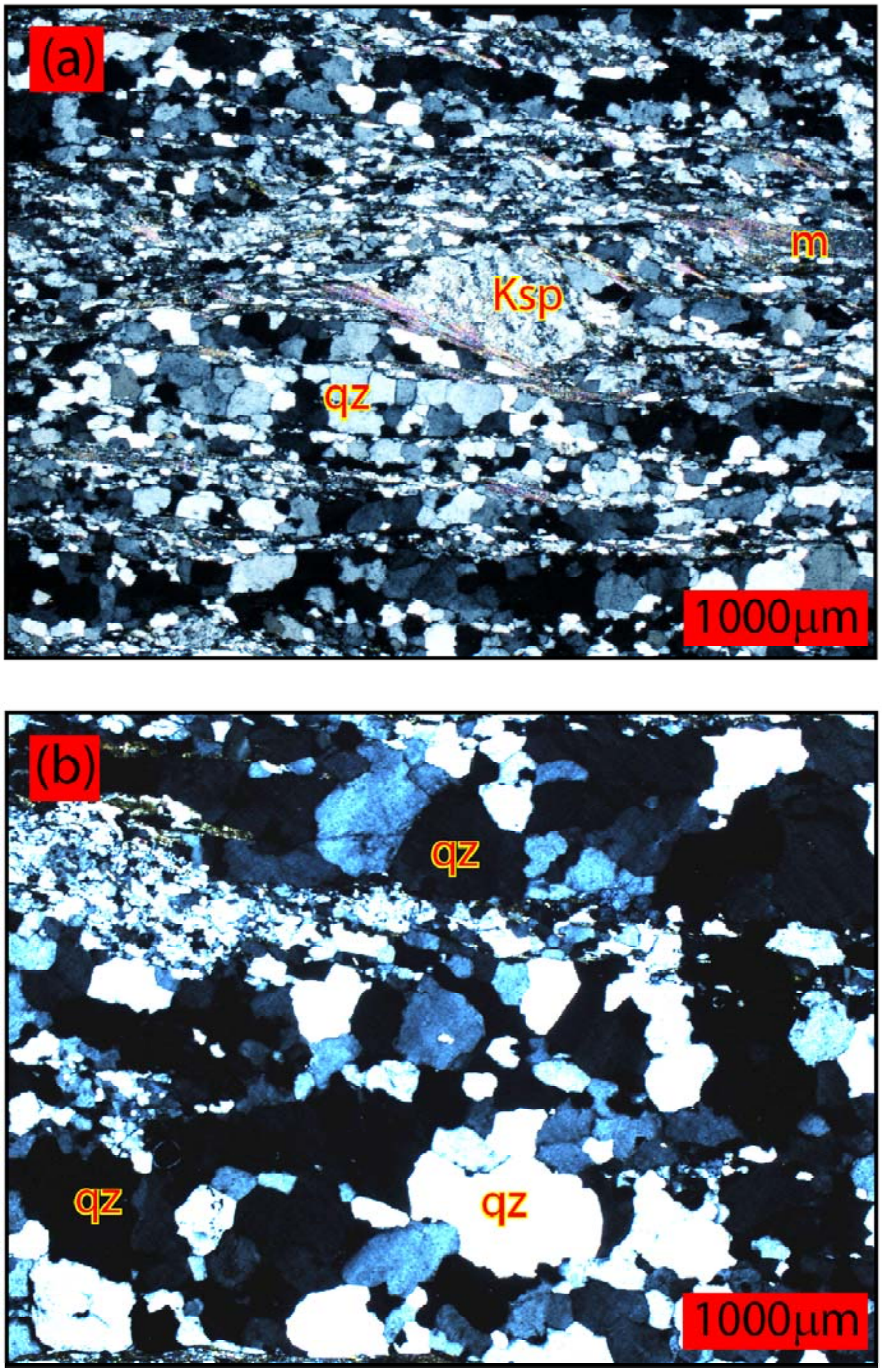

Figure 3-7. Quartz ribbons in phyllonite (a) (WS-022-II, from Blackwell Bridge, Chauga River, Whetstone quadrangle, SC). Quartz ribbon in MHG (b) (WS-037-I, from Double Branch, Whetstone quadrangle, SC). Ksp = K-feldspar; m = muscovite; qz = quartz.

Figure 3-8. Photomicrograph of deformation lamellae in phyllonite (D) oriented NW-SE in crossed polars (a and c) and plane light (b and d) (WS-024-II, from Blackwell Bridge, Chauga River, Whetstone quadrangle, SC). m = muscovite; qz = quartz.

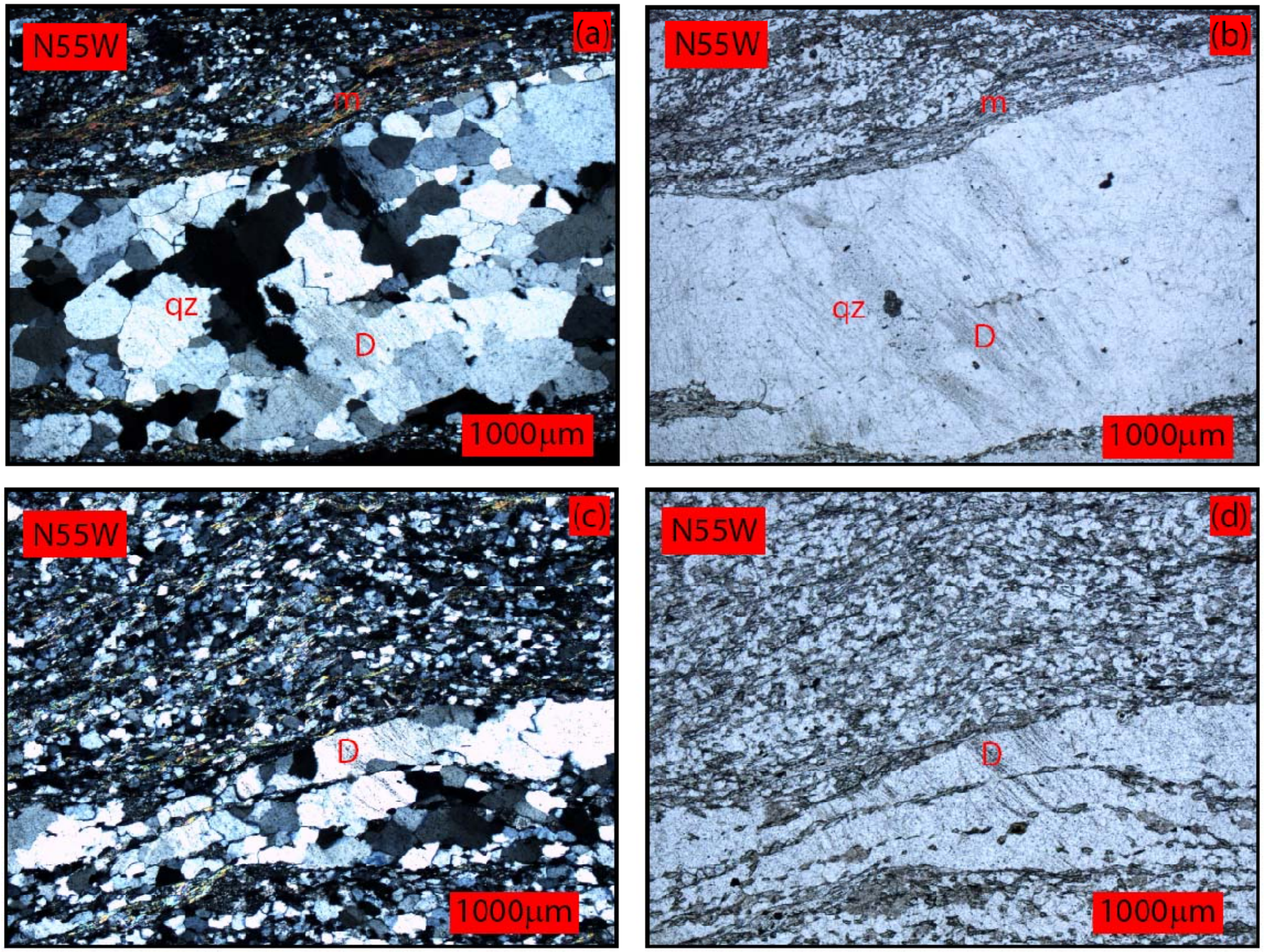
N55W
(a)
m
qz
D
1000μm
N55W
(b)
m
qz
D
1000μm
N55W
(c)
D
1000μm
N55W
(d)
D
1000μm

RGN Comparisons

Two thin sections from a single sample (G05-01 a and b) collected from the South Tibetan detachment exposed near Gondasampa, Tibet, were analyzed by myself and compared with the original data of Jessup et al. (2007). My data yielded a substantially different pattern, compared with the data from Jessup et al. (2007). Measured porphyroclasts in two thin sections were highly subjective, but the following two RGN plots (Fig. 3-9) contain a consistent range of W_m values. My calibrated W_m has a range from 0.53 to 0.60 (Fig. 3-9a). Jessup et al. (2007) reported a range of W_m from 0.57 to 0.60 (Fig. 3-9b). The two data sets have an insignificant difference of ~3.4 percent. These results demonstrate an advantage of the RGN plot in that the trend of the dataset plays a more important role in determining W_m than on relying on outlier points. Comparison revealed that, although different outliers were plotted (red circles in Fig. 3-9), the two datasets yield a similar trend by using the transition defined by a larger number of grains.

Both plots contain an obvious outlier (circled with dashed red line) with opposite signs. This raised the need for caution in measuring θ. W_m estimates are not only a constant term indicating pure and simple shear, but also a useful approach implying deformational mechanism at the micro-scale. Arbitrary assigned positive or negative angles may have affected data extrapolation to map scale.

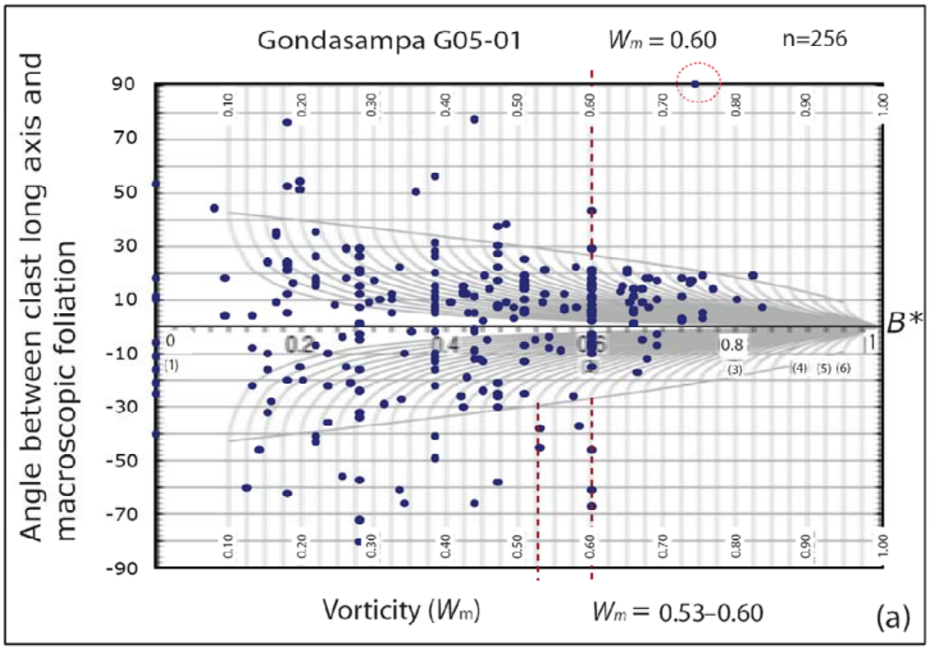

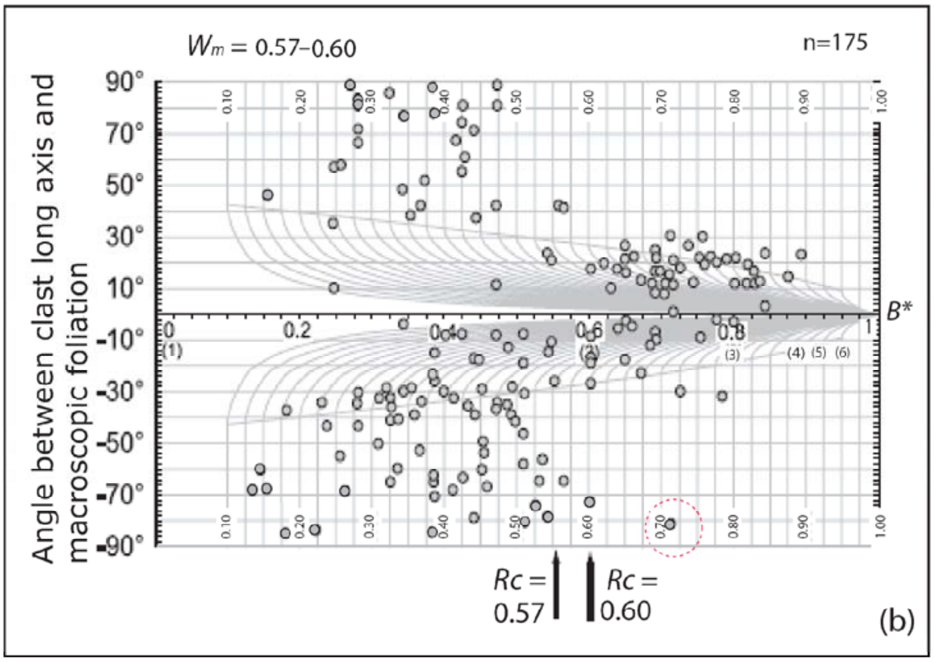

Figure 3-9. Comparison of the calibration result (a) and the result (b) from Jessup et al. (2007).

Quartz *C*-axis Calibration

Thin section R03-16(1), collected from the Rongbuk Valley, Tibet, was analyzed and compared to the original data of Jessup et al. (2006). Calibrated measurements were combined with pre-existing stereonet data (provided by M. Jessup) (Fig. 3-10). Overall, my pattern produced good agreement on shear–sense direction and data point distribution. Meanwhile, my quartz *c*-axis diagram shows a combination of basal and rhomb <*a*> slip system. Deformation temperature was estimated around 500–600 ± 50°C by estimating the open-angle of the central girdle ($360-\omega_1-\omega_2$) (Kruhl, 1998; Law et al., 2004). This result is lower than Jessup et al. (2006) reported at 525–625 ± 50°C. Figure 3-10 shows the calibrated plot with a relatively narrow open angle, and some scattered data points located in the top and bottom domains.

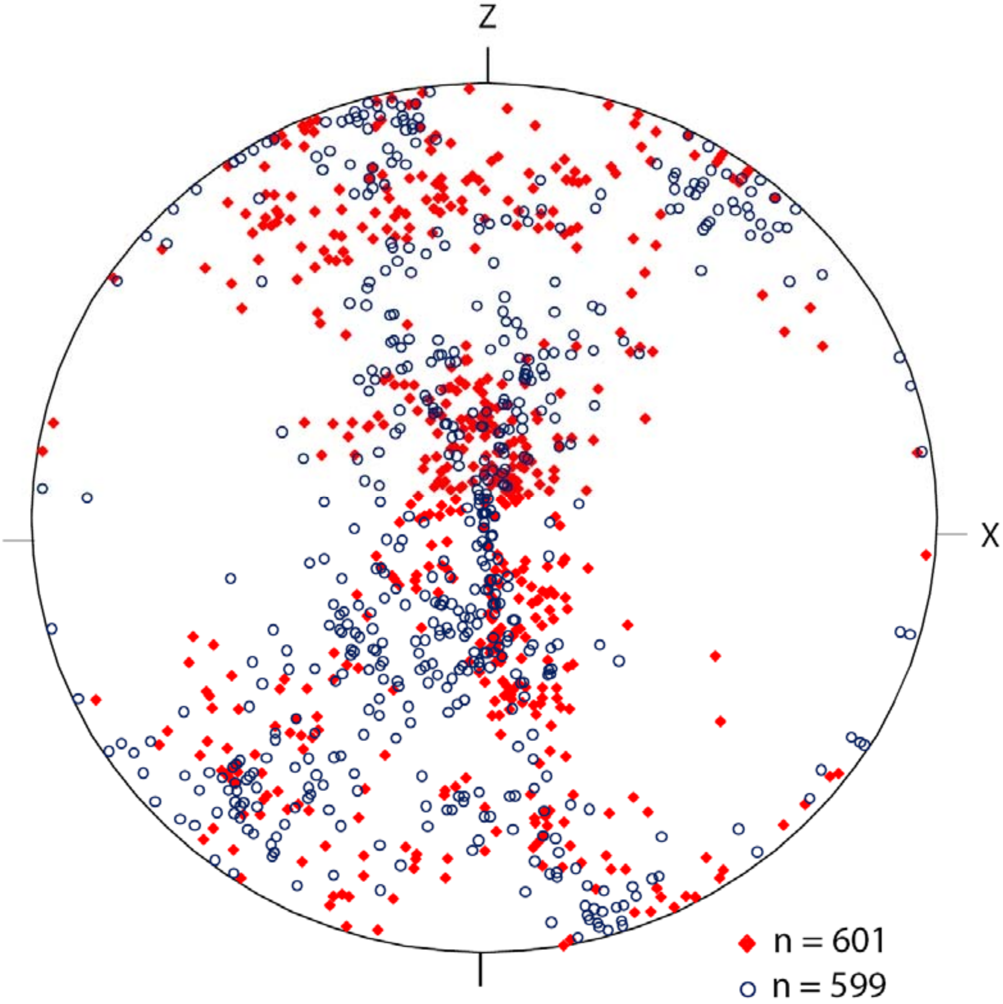

Figure 3-10. *C*-axis stereoplot (unrotated) calibration. Data points in red diamonds represent calibration; data points in blue circles from Jessup et al. (2006).

CHAPTER IV

RESULTS

RIGID GRAIN NET (RGN) PLOT W_m ANALYSES

All measurements are summarized here, including rigid body behavior analyses (the RGN plot was used) and crystallographic fabrics (quartz c-axis). In the RGN plots, the mean kinematic vorticity (W_m) is separated into two groups: higher and lower ranges of W_m. The higher W_m values are determined by comparison of W_m results when a higher W_m value is greater than five percent over a lower W_m. All measurements (M_L, M_S, and θ) were made from feldspar clasts in all thin sections; feldspar and sphene clasts were measured in WS-022. Shear sense was determined from quartz c-axis diagrams.

RGN plots were produced with two data sets identified as “I” and “II”: I (XZ-plane) indicates the sections normal to dominant foliation and parallel to lineation; II (YZ-plane) represents the sections normal to foliation and lineation. To maximize the utility of W_m estimates, orientations of each thin section were carefully recorded prior to making measurements of parameters that yield W_m.

Two examples are presented below (TA-033-I and WS-033-I), illustrating the manner of estimating W_m based on RGN plots. The same strategy was used in all plots. In order to maintain consistency, relative north and south were assigned positive and negative angles, respectively. Sections I and II were plotted separately, then W_m ranges between sections I and II were compared.

Example of W_m Interpretation Using RGN: TA-033-I

The first case, TA-033-I plot (Fig. 4-1), the upper limit of W_m ranges from 0.57 to 0.62. The upper bound ($W_m = 0.62$) was determined by two data points (highlighted yellow inside a black circle) at the vertical B^* line = 0.62, $R = 2.10$ and $|\theta| > 40^o$; data points continue to extend below the R_c curve until $|\theta| < 10^o$. The same principle was used to interpret the lower bound. Two points (in green) just exceeded R_c because they lack data points at stable positions (below R_c curve), and are regarded as outliers. The lower bound of the upper limit of W_m was defined based on a clear trend below the R_c curve located between $B^* = 0.55–0.58$, and a mid-point was used (in orange). The lower limit W_m is a positive angle with a $B^* = 0.53$ and $R = 1.89$, trending strongly below R_c. One outlier was marked in green slightly above R_c.

Example of W_m Interpretation Using RGN: WS-031-I

In the WS-031-I diagram (Fig. 4-2), the higher W_m ranges from 0.65 to 0.72 and was determined by two sets of rigid grains with $R \approx 2.25$ and 2.60, respectively. Two bounds reveal a strong trend that extends below the critical threshold (R_c). A series of data points yields a nice curve that can be traced along $10^o < |\theta| < 59^o$ at $B^* \approx 0.64–0.66$. A mid-point value was identified to draw a lower bound of the higher W_m. Although they lack a strong trend below R_c, these points substantially exceeded R_c. Hence, they were used to estimate W_m. The lower limit of W_m ranges from 0.60 to 0.70. The upper bound ($W_m = 0.7$) was determined by a well-defined trend above and below R_c. Three data points within the lower W_m range had no obvious trend below R_c; hence, the trend at $B^* = 0.60$ and $R = 2.0$ was considered more representative data with which to draw this boundary.

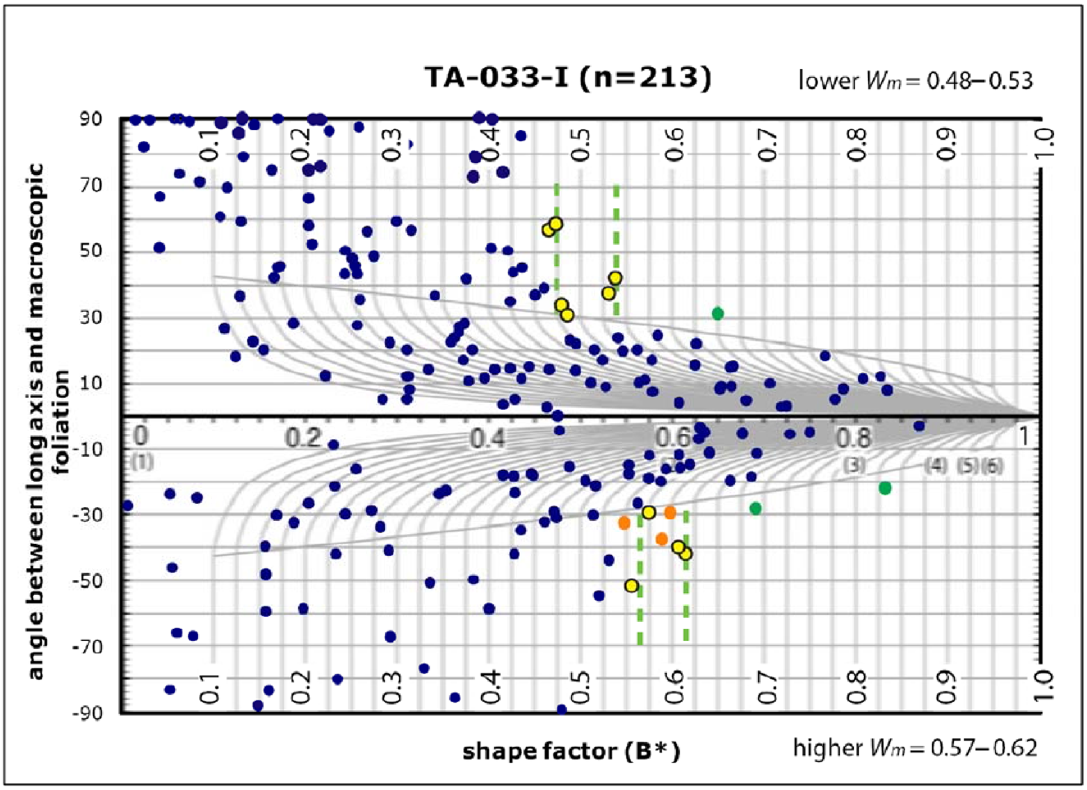

Figure 4-1. Example of estimating W_m from Tamassee quadrangle, SC sample TA-033-I. Population size (n = 213). Results indicate a pure shear domain. Measured data points are in blue. Outliers and critical data points are highlighted in different colors. Green dashed lines represent the range of W_m values. Yellow dots with black circles indicate critical data points to estimate W_m. Orange points indicate lack of trend below R_c. All data were collected from feldspar porphyroclasts.

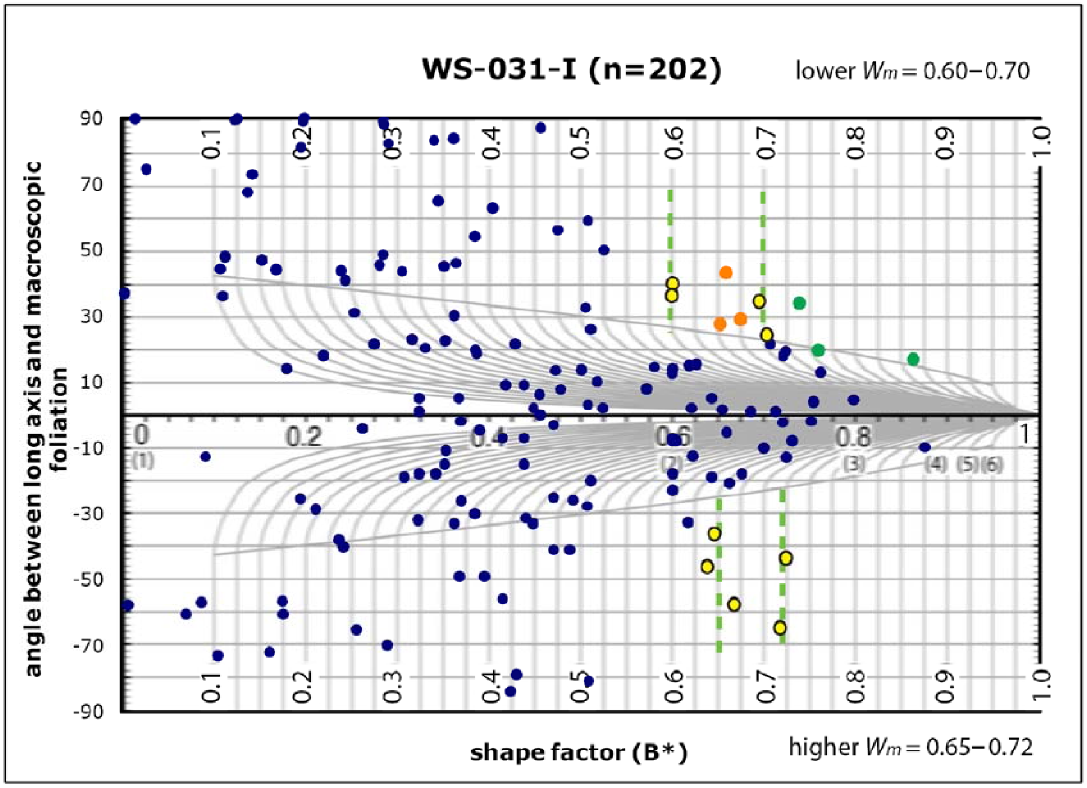

Figure 4-2. Example of estimating W_m from Whetstone quadrangle, SC sample WS-031-I. Population size (n = 202). Results indicate a pure shear domain. Outliers and critical data points are highlighted in different colors. Yellow dots with black circles indicate critical data points to estimate W_m. Orange points indicate lack of trend below R_c. All data were collected from feldspar porphyroclasts. Data points are in blue. Green dots designate outliers. Green dashed lines represent the range of W_m values.

W_m Results from Parallel- (XZ) and Perpendicular- (YZ) to Lineation Sections

Eleven MHG samples and one MG sample were analyzed using the RGN method (Appendix A). Table 4-1 summarizes the range of W_m that was estimated for the 12 samples. RGN analyses showed that W_m values are paired in high-low patterns in the BFZ along strike. Percentage of pure shear was calculated using the method of Law et al. (2004). Most samples yielded > 50 percent pure shear. The localities yielding simple shear are WS-031 from Crooked Creek, Whetstone quadrangle, SC, WS-037, and WS-039 from Double Branch, Whetstone quadrangle, SC.

The suite of plots reveals that most of the upper limit of W_m values are located in the domain of negative θ angles in RGN plots, corresponding to the SW direction geographically; the higher W_m relate to the mesoscale displacement direction (Table 4-1). W_m results of WS-022-I (from Blackwell Bridge, Chauga River, Whetstone, SC) and WS-029-I (from Cassidy Bridge, Whetstone, SC) are almost identical in both positive and negative θ angles. Note that sample WS-027-I (from SC Highway 28, Whetstone, SC) has a higher W_m to the NE; it could be a result of high pure shear and heterogeneity in small scale, which produced a higher W_m value to the NE. RGN plots of perpendicular sections (YZ) were made (Appendix B) and denoted in each sample as "II." Positive and negative angles were assigned relatively N- and W-ward, respectively. Table 4-2 summarizes all measurements, pure shear percentages, and higher W_m direction.

Table 4-1. W_m estimates for XZ sections.

Results of W_m analyses

		W_m				
Quadrangle	Samples	lower	higher	higher W_m direction	% difference between higher and lower W_m	range of % of pure shear
TA	033-I	0.48-0.53	0.57-0.62	S35W	17	61-58
TA	034-I	0.56-0.67	0.67-0.72	S35W	7.5	62-49
WS	027-I	0.51-0.62	0.67-0.72	N54E	16.1	66-49
WS	022-I	0.38-0.43	0.38-0.43	-	0	74-71
WS	017-I	0.53-0.67	0.53-0.71	S56W	6	64-50
WS	029-I	0.76-0.80	0.76-0.83	-	3.7	44-38
WS	031-I	0.60-0.70	0.65-0.75	S50W	7.1	59-46
WS	037-I	0.50-0.74	0.77-0.82	S41W	10.8	66-38
WS	039-I	0.75-0.78	0.73-0.83	S30W	6.4	48-38
WS	US-76-I	0.52-0.61	0.60-0.71	S27W	16.4	66-50

Table 4-2. W_m estimates for YZ sections.

Results of W_m analyses

Quadrangle	Samples	W_m lower	W_m higher	higher W_m direction	% difference between higher and lower W_m	range of % of pure shear
TA	033-II	0.35-0.47	0.43-0.55	S55E	17	78-65
TA	034-II	0.56-0.65	0.52-0.74	S55E	13.8	66-47
WS	027-II	0.35-0.43	0.20-0.45	-	4.7	88-70
WS	022-II	0	0.37	N51W	37	100-76
WS	017-II	0.16-0.28	0.32-0.44	N34W	57.1	90-71
WS	029-II	0.60-0.68	0.71-0.82	S60E	20.6	59-39
WS	031-II	0.42-0.65	0.55-0.70	N40W	7.7	72-50
WS	037-II	0.52-0.62	0.61-0.66	S49E	6.5	59-54
WS	039-II	0.51-0.61	0.50-0.60	-	1.7	67-59
WS	US-76-II	0.57-0.70	0.50-0.75	N63E	7.1	67-46

Unlike the results from XZ sections, the W_m estimates in the YZ-plane do not converge in one direction, and the high-low pattern of W_m values is even more pronounced. Three W_m estimates exceed 0.71, where samples TA-034-II, WS-029-II, and WS-US-76-II are dominated by simple shear. A high percentage of pure shear ($W_m < 0.71$) is obtained from others. W_m values are identical in the RGN plots of both positive and negative domains in samples WS-027-II and WS-039-II.

This high-low pattern and dominant direction variation in YZ sections is probably due to: 1) variations in lithology or strain heterogeneity; 2) triclinic deformation; and 3) combination of both factors, which may have been locally involved.

Comparisons attempted to verify if the stretching lineation is parallel to the transport direction. One assumption in a monoclinic shear system is that the instantaneous stretching axis (maximum stretching direction) is aligned parallel to transport direction. Hence, the W_m value of XZ sections would be expected to be greater than in YZ sections. Conversely, W_m of YZ sections is greater than in XZ sections, because triclinic shear may be a component of the deformation process (Forte and Bailey, 2007). In fact, this pattern also can be determined not only within microscale, but also can be defined by measuring foliation and mineral lineation at the mesoscopic scale.

All measurements from both sections (I and II) were recorded on the same RGN diagram (Appendix C). Samples TA-034 (from SC Highway 127, Tamassee quadrangle, SC) and WS-US-76 (from Whetstone quadrangle, SC) (Fig. 4-3) can be distinguished from other samples by a higher W_m value in section II than in section I. Sample TA-034-

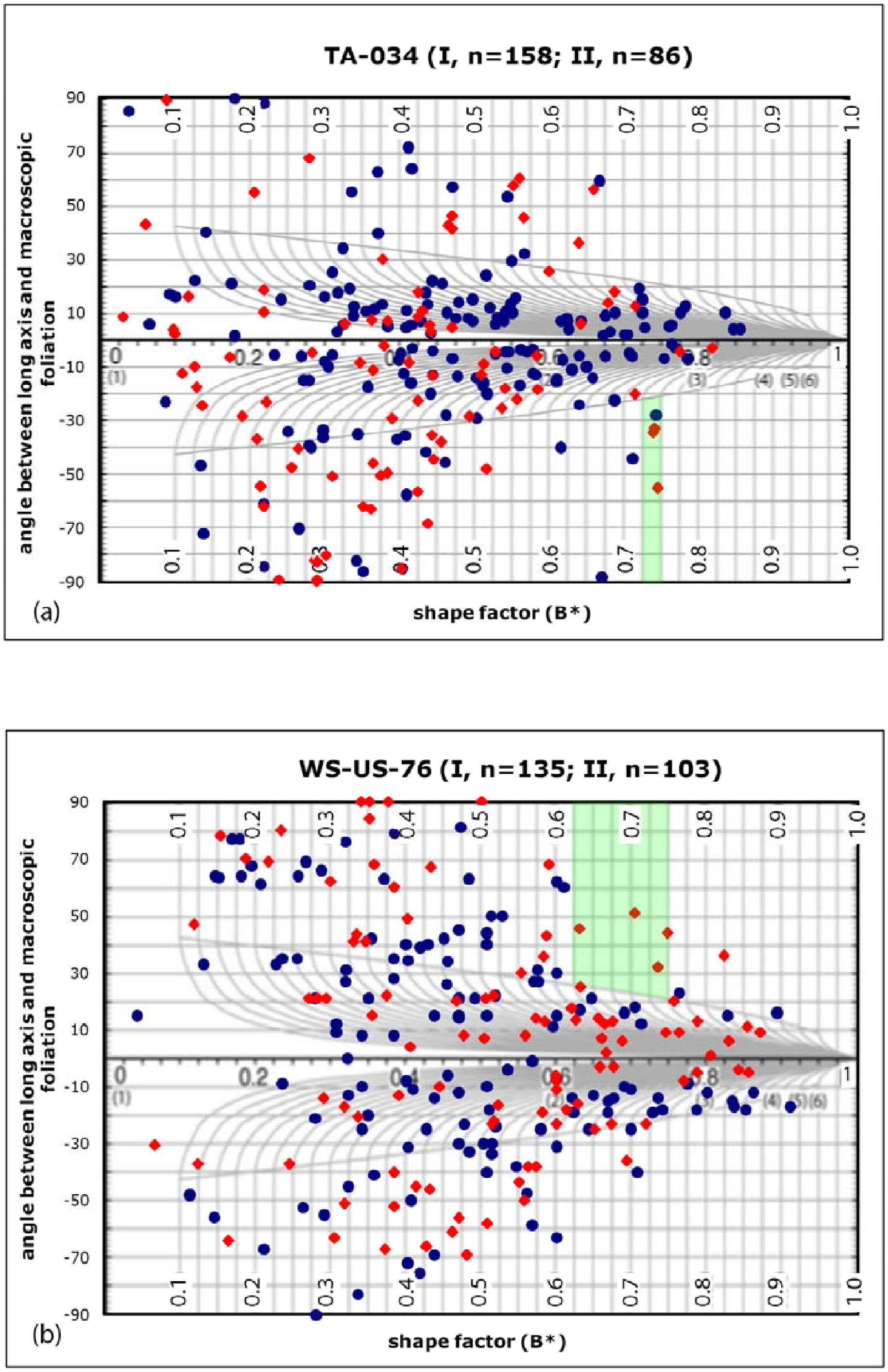

Figure 4-3. Using RGN diagrams to compare XZ- and YZ- plane. Samples TA-034 (a) and WS-US-76 (b). Blue and red dots represent W_m estimates in the XZ- and YZ-planes, respectively. Discrepancy is highlighted in green. All data were collected from feldspar porphyroclasts.

II has a negative angle of about three percent higher than TA-034-I. Sample WS-US-76-II has a W_m about 23 percent higher than the W_m of section I.

Results imply that triclinic shearing likely occurred at both of these localities. It is important to mention that the comparisons were made with uneven data points, and the effects of population distribution on interpretations remain uncertain.

Difference Comparison

W_m comparisons demonstrate the amount of strain varies across the BFZ. Samples TA-033 and TA-034 were collected 2 m apart. Samples WS-037 and WS-039 were located about 1.5 m apart. W_m range is higher along strike to the SW.

TA-033 vs. TA-034

The RGN plots of samples TA-033 and TA-034 (Figs. 4-4 and 4-5) illustrate that one sample (TA-033) collected 2 meters to the SE has a higher W_m value, in which a relatively higher component of simple shear occurred during progressive deformation. Additionally, the affinity of TA-033 and TA-034 composition suggests that mineralogy does not affect the results of W_m estimates. In a linear shear zone like the BFZ, a non-steady state mechanism is less likely to happen. Hence, the triclinic shear mechanism may have influenced the deformation pattern that differentiates W_m results at the same location. Based on this result, one can confirm the interpretation from the previous section that the higher W_m to the SE may be the result of displacement.

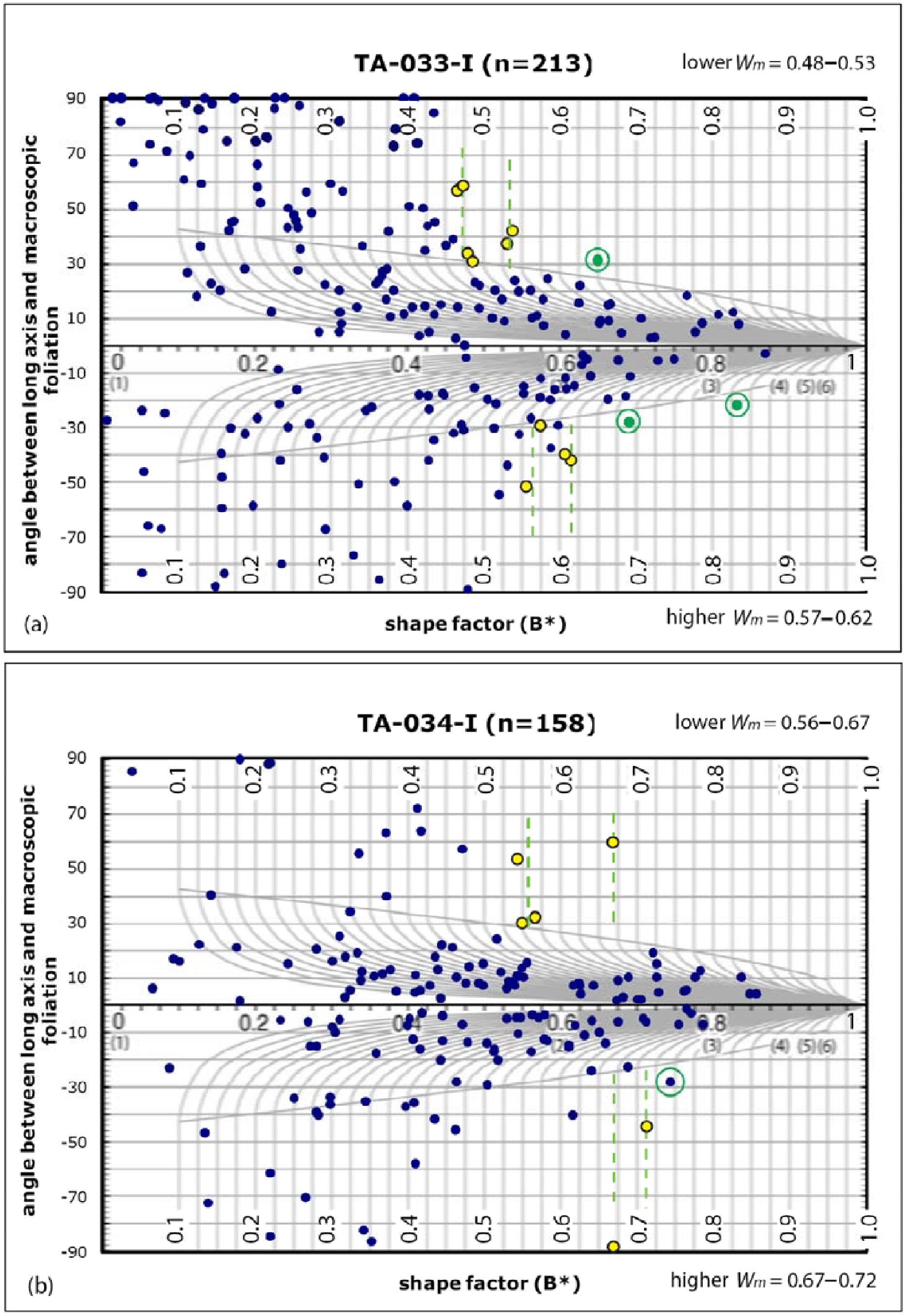

Figure 4-4. Difference comparison of TA-033-I (a) and TA-034-I (b) via RGN plot, data points in blue. Green dashed lines indicate the upper and lower range of W_m. Yellow dots encircled in black indicate the critical data points that were employed to draw the upper and lower boundaries of W_m. Outliers consist of green dots enclosed in a green circle. All data were collected from feldspar porphyroclasts.

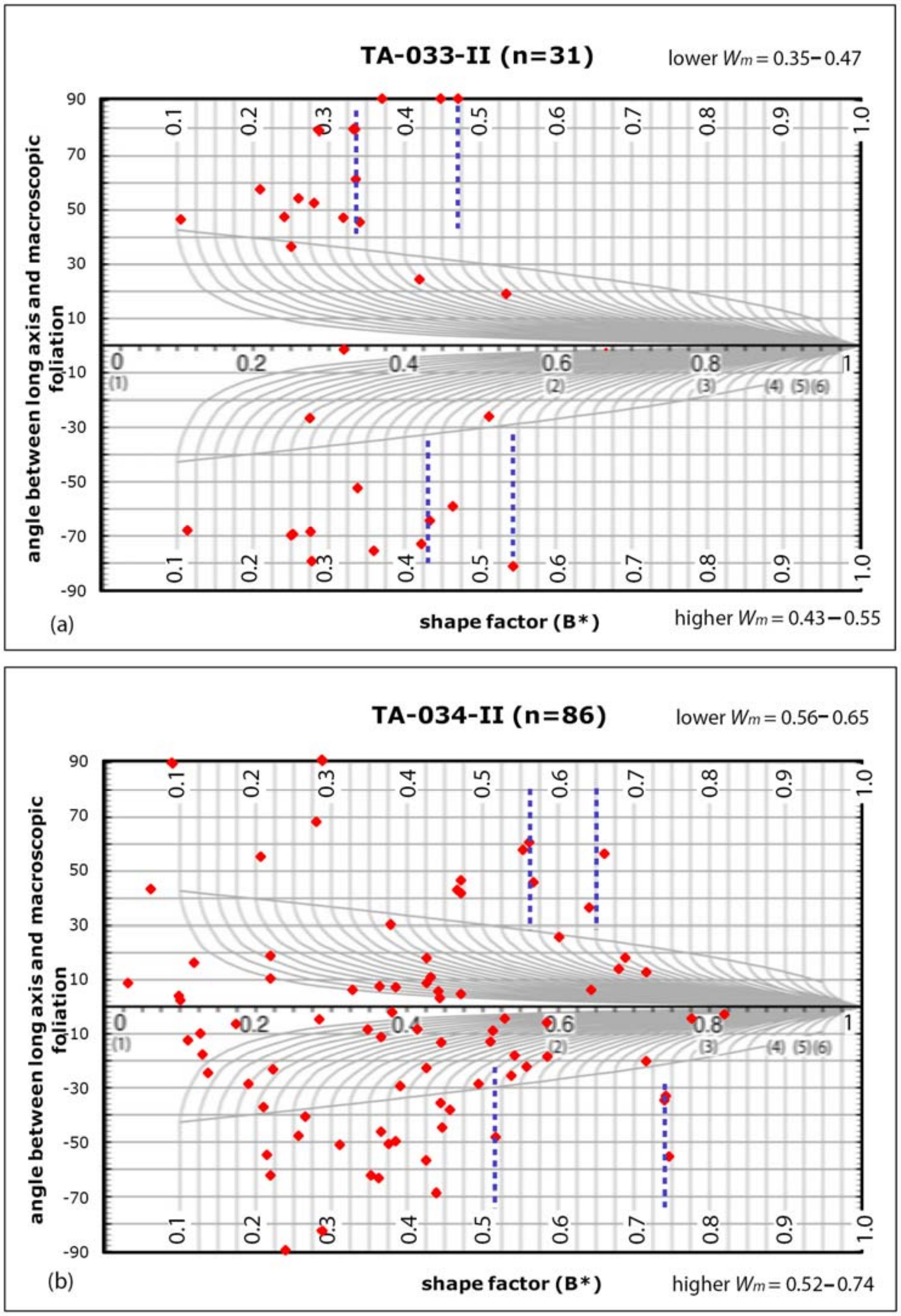

Figure 4-5. Difference comparison between TA-033-II (a) and TA-034-II (b), with red data points. Blue dashed lines indicate the upper and lower range of W_m. All data were collected from feldspar porphyroclasts.

Meanwhile, both plots display a higher W_m to the SW as well. In terms of YZ-plane, TA-034-II also shows a higher W_m value than TA-033-II. Both RGN diagrams display a higher W_m to the SE. Note that the higher W_m of TA-034-II is 0.74, about 35 percent higher than TA-033-II. One possible interpretation is that plastic diminished toward the south.

WS-037 vs. WS-039

WS-039 was collected about 1.5 m SE of WS-037 (Fig. 4-6 and 4-7). In the XZ-plane, the upper limit W_m of WS-037-I ($W_m = 0.77$–0.82) and WS-039-I ($W_m = 0.73$–0.83) is almost identical, yet the lower limit W_m of WS-037-I ($W_m = 0.50$–0.74) is estimated significantly lower than WS-039-I ($W_m = 0.75$-0.78). Meanwhile, W_m estimates in the YZ-plane are less than the XZ-plane and display a range similar to that of the XZ-plane.

Modal analyses indicate mineral compositions of WS-037 and WS-039 are almost identical (WS-037 contains a higher percentage of muscovite and biotite; WS-039 contains a higher percentage of quartz based); hence strain variation is a possible factor to differentiate the W_m value at the lower W_m.

Overall, difference comparisons from two sets of samples suggest that triclinic shear played an essential role, causing W_m estimates to vary over short distances in outcrops.

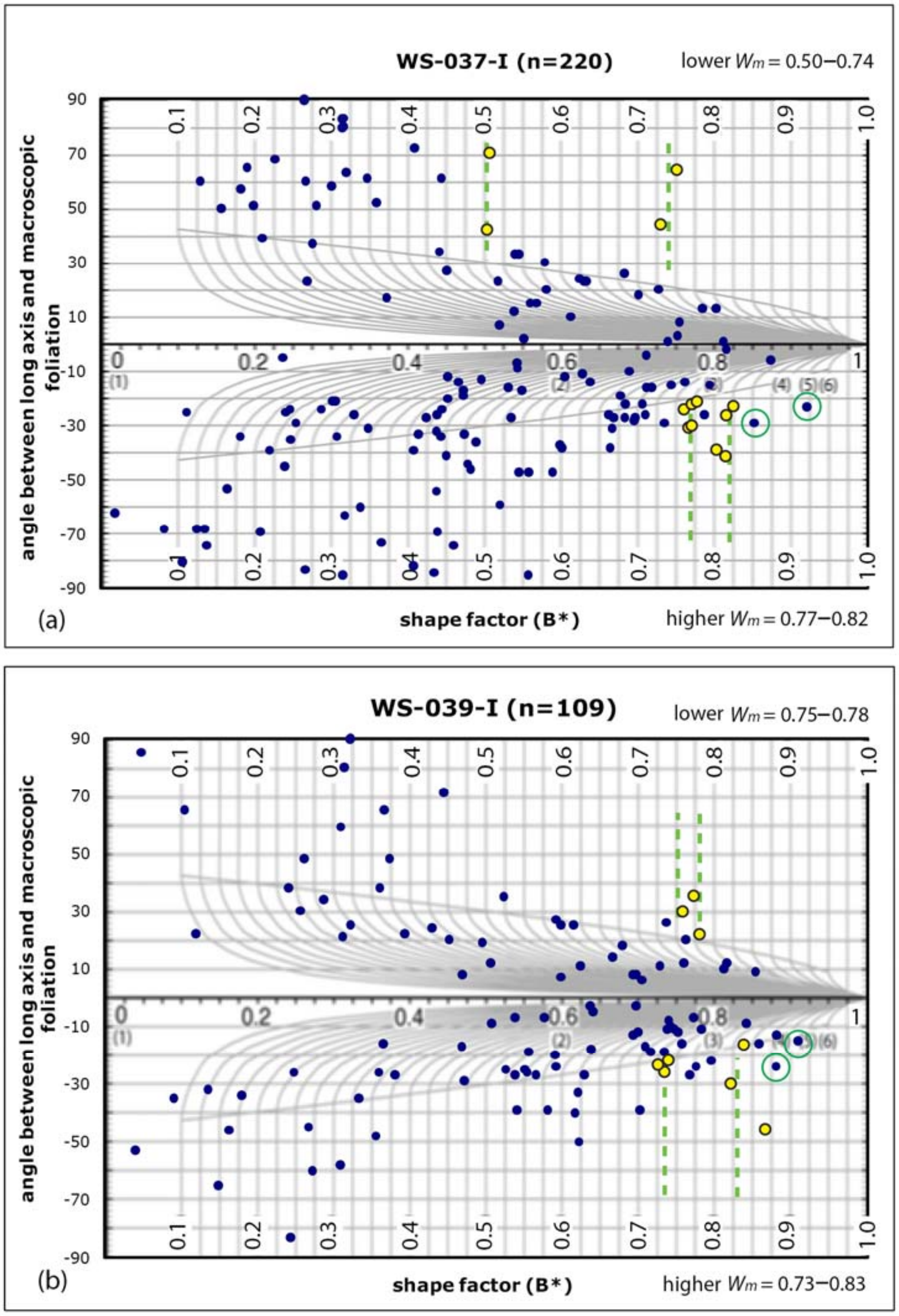

Figure 4-6. Difference comparison of WS-037-I (a) and WS-039-I (b) with blue data points. Green dashed lines indicate the upper and lower range of W_m. Yellow dots circled with black indicate the critical data points that were used to draw the upper and lower boundaries of W_m. Outliers are circled with a solid green line. All data were collected from feldspar porphyroclasts.

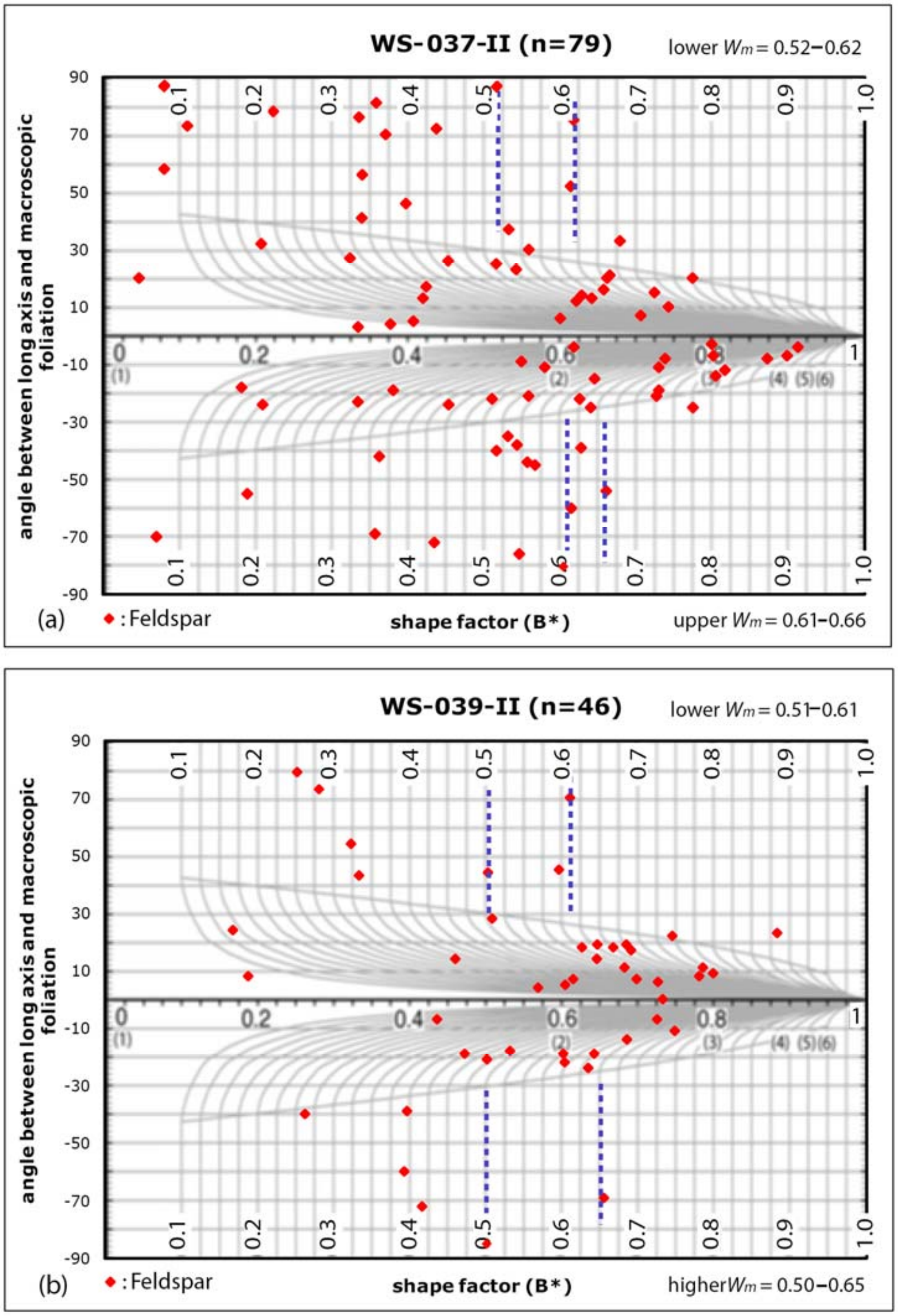

Figure 4-7. Difference comparison of WS-037-II (a) and WS-039-II (b), data points in red. Blue dashed lines indicate the upper and lower range of W_m. All data were collected from feldspar porphyroclasts.

An Average Kinematic Vorticity Value for the BFZ

As stated in Chapter II, mean kinematic vorticity is a representative elementary value, which does not consist of an average number. In order to compare with preexisting data that will be discussed in Chapter V, a range of α angles (see Equation 2-7) was calculated using higher W_m from Table 4-3 (Bobyarchick, 1986). A histogram is plotted according to the range of α angles and the average $\alpha \approx 45^o$ (Fig. 4-8). Applying Equation 2-7, an average W_m is 0.71, implying the pure and simple shear equally contributed to the deformation.

Table 4-3. Range of α angles from different localities.

Quadrangle	Samples	Higher W_m range		Range of α	
TA	033-I	0.57	0.62	55	52
TA	034-I	0.67	0.72	48	44
WS	027-I	0.67	0.72	48	44
WS	022-I	0.38	0.43	68	65
WS	017-I	0.67	0.71	48	45
WS	029-I	0.80	0.83	37	34
WS	031-I	0.70	0.75	46	41
WS	037-I	0.77	0.82	40	35
WS	039-I	0.78	0.83	39	34
WS	US-76-I	0.61	0.71	52	45

TA : Tamassee; WS: Whetstone.

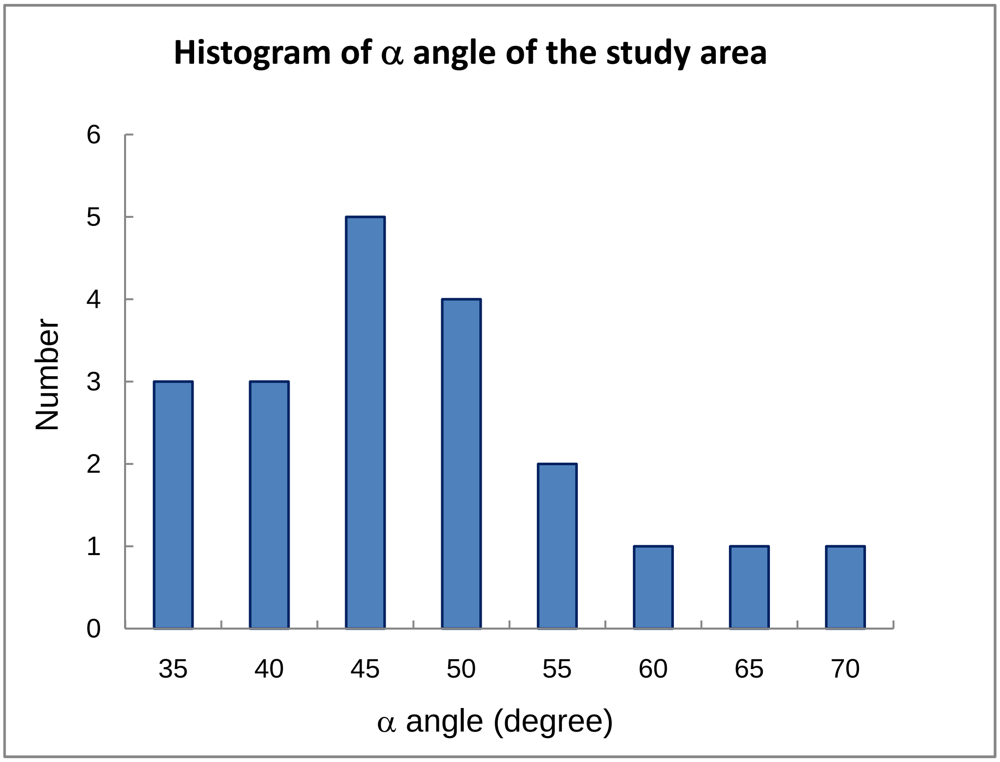

Figure 4-8. α angles converted from a range of W_m in the study area.

QUARTZ *C*-AXIS RESULTS

Five quartz *c*-axis fabric stereonets were plotted on a lower hemisphere equal-area net (Fig. 4-8). Based on density distribution, the phyllonite unit (from Blackwell, Chauga River, Whetstone quadrangle, SC) can be described as a combination of Type-I and II cross-girdles (see Fig. 3-8) (Lister and Price, 1978; Passchier and Trouw, 2005). The external pattern displays a top-to-the-SW shear sense indicates a dextral shear sense on the mesoscopic to map scale. Shear sense from quartz *c*-axis diagrams and W_m estimates are consistent. WS-037-I was taken from MHG; WS-024-I and WS-020-I, and WS-022-I quartz *c*-axis diagrams were obtained from recrystallized quartz ribbons in the phyllonite units. Quartz *c*-axis plots from phyllonite units have no clear internal girdle systems, and no specific deformation temperature can be defined. An additional measurement of WS-024-I was made from annealed quartz grains in the groundmass. All measurements are recorded in Appendix D.

WS-037-I (MGH) (Fig. 4-9a) has a clear central girdle with two defective limbs. The deformation system has involved a combination of rhomb <*a*> and minor basal <*a*> slip. The R_f (strain ratio) value was calculated at 3.14 using the method of Wallis (1995). Opening angle is 45–47 degrees; possible deformational temperature is estimated at ~360 ± 60°C (Appendix E), according to empirical curve of Kruhl (1998).

The phyllonite unit (WS-024-I, WS-022-I, and WS-020-I) contains a combination of Type-I and Type-II types of skeletons (Law, 1990), with a medium to high temperature pattern and c-axes that cluster around the Y-axis. The quartz in WS-020-I (Fig. 4-9b) contains a strong prism <*a*> slip system with a medium deformation temperature. WS-

024-I (Fig. 4-9c) quartz *c*-axis diagram from recrystallized quartz ribbon has a mixture of high-T *c*-slip and rhomb <*a*> slip system. Additional measurements from groundmass quartz grains, WS-024-I (Fig. 4-9d), show a medium temperature rhomb <*a*> slip (Y-axis cluster) and a randomly scattered pattern. Quartz grains from the groundmass may have annealed more completely than quartz grains in recrystallized quartz ribbons. WS-022-I (Fig. 4-9e) also displays a strong cluster around the Y-axis representing a prism <*a*> slip system that is very similar to WS-020-I. Moreover, quartz *c*-axis diagrams from phyllonite units show that the medium to high temperature grains were inherited from the previous high temperature event during the Neoacadian orogeny.

COMPARISON OF RGN AND WALLIS PLOTS

Although the data are identical, values of W_m may vary by using different methods. The Wallis plot emphasizes the pattern of outliers when defining the critical threshold (θ_c) that would affect W_m estimates by significantly overestimating the contribution of simple shear (Jessup, pers comm.). Hence, outliers were disregarded using the RGN technique.

Two cases are presented here that demonstrate the W_m values could vary using RGN and Wallis plots. Samples TA-033-I and WS-029-I were plotted by both the RGN and Wallis methods and a comparison was made of the results. Accordingly, one case (sample WS-029-I from Cassidy Bridge) demonstrated good agreement between two plots, and one (TA-033-I) did not.

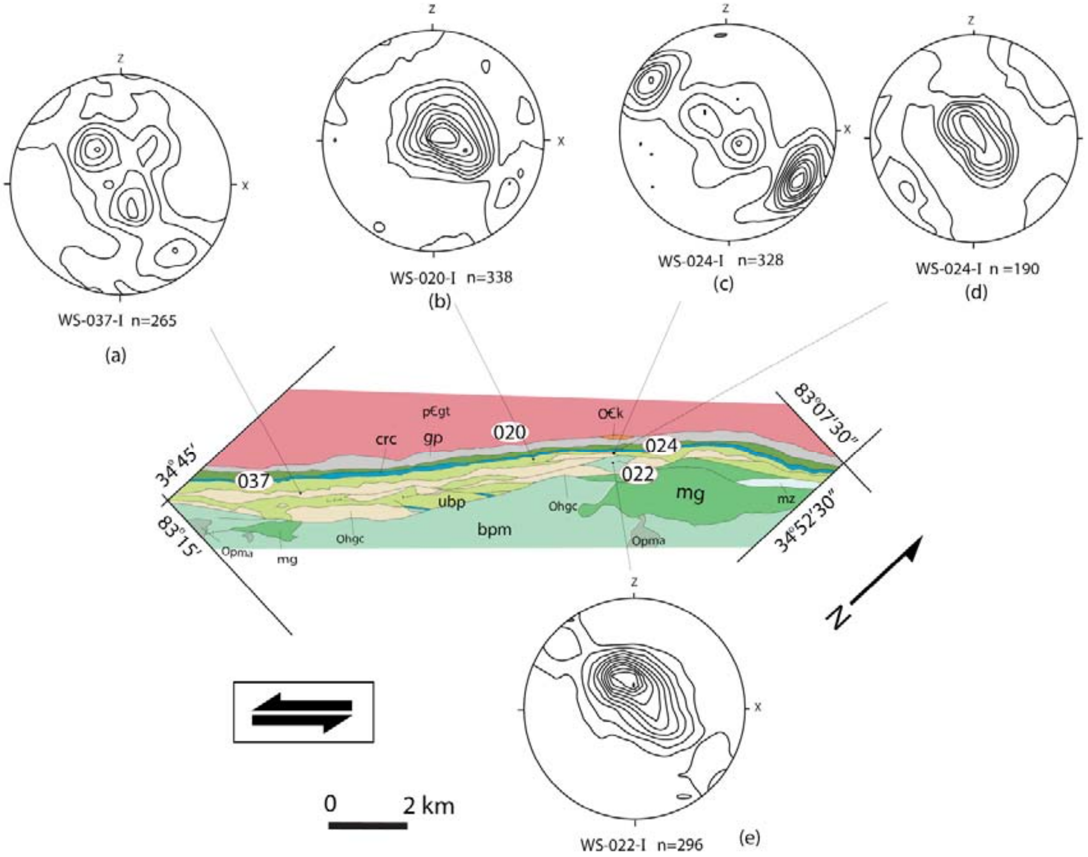

Figure 4-9. Quartz *c*-axis data from four samples in the Whetstone quadrangle, SC (geology after Hatcher et al., 2000). Explanation of rock units may be found in the Figure 1-5. (a): WS-037-I; (b): WS-020-I; (c) and (d): WS-024-I; (e): WS-022-I. Diagrams a, b, c, and e were plotted from measurements from quartz ribbons. Diagram (d) was plotted by quartz grain from the groundmass. Sinistral shear sense is top-to-the-SW.

TA-033-I and WS-029-I

A huge discrepancy between RGN and Wallis plots results occurs in the same data sets. Determining W_m values from the Wallis plot method was a challenge when the data points were scattered and do not have a clear trend. For instance, in the Wallis plot of TA-033-I (Fig. 4-10) and WS-029-I (Fig. 4-11), W_m was overestimated in the first attempt (marked by gray dashed lines). Outliers (circled with green) were difficult to identify from data points that were used to construct the envelope (solid black line); hence, the values of W_m were slightly higher. With RGN plots, on the other hand, outliers were easily distinguished from those below the critical threshold. Thus, the results were less ambiguous. After the outliers were removed, the range of W_m in the second estimate (yellow dashed lines) was close to the range estimated by the RGN plot.

If the data points had a clear pattern, both RGN and Wallis plots demonstrated good agreement. Nevertheless, no ambiguity appeared in the Wallis plot.

Figure 4-10. RGN (a) and Wallis (b) plots of sample TA-033-I. Comparison of green dashed lines in RGN diagrams indicates the W_m ranges. Solid black and green dashed envelopes in the Wallis plot represent the possible W_m ranges for first and second estimates, respectively. Red circles indicate the data used to construct critical R_c envelopes, and green circles represent outliers.

TA-033-I (n=213)

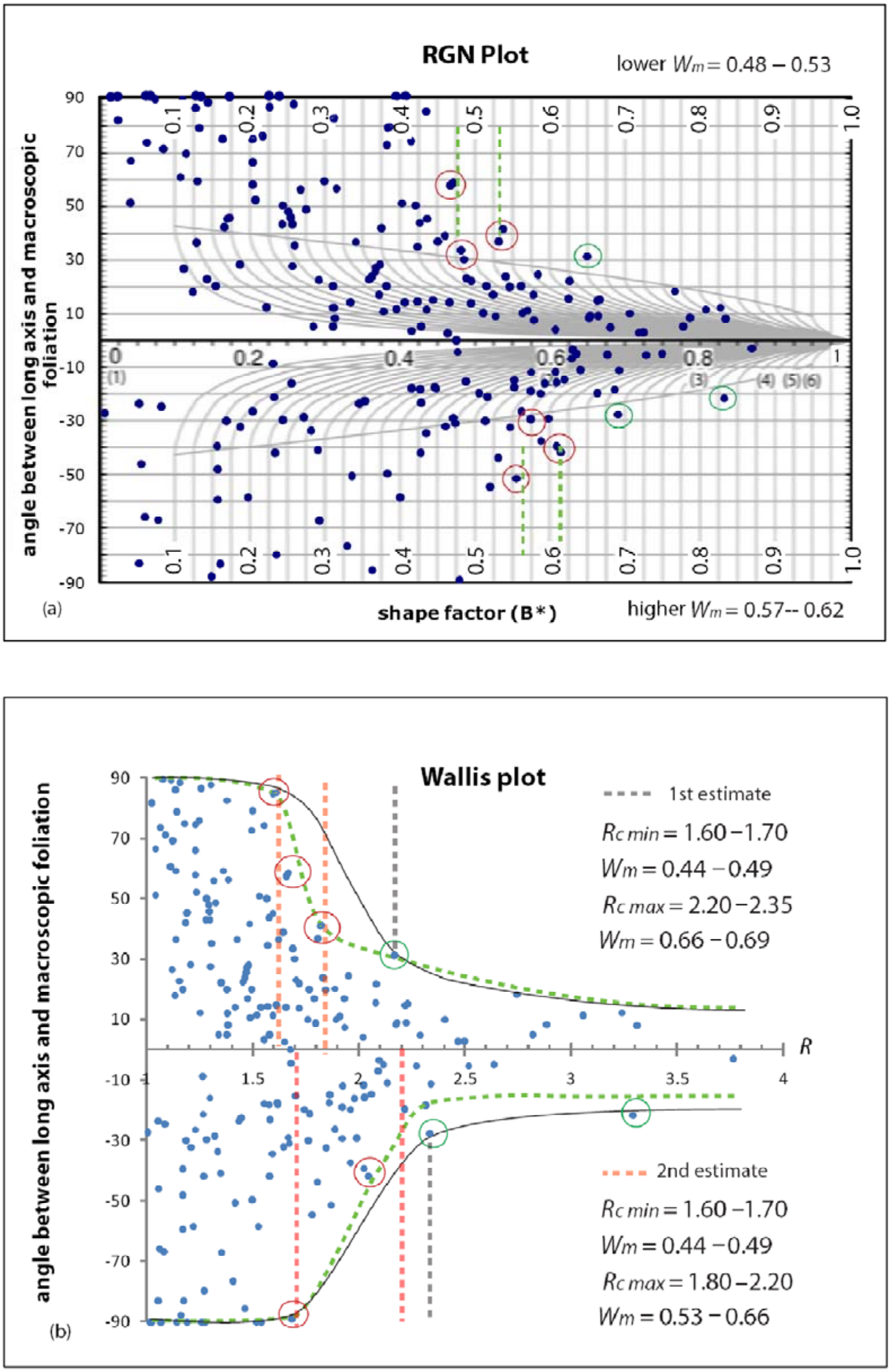
RGN Plot
lower Wm = 0.48 – 0.53
angle between long axis and macroscopic foliation
90
70
50
30
10
-10
-30
-50
-70
-90
0.1
0.2
0.3
0.4
0.5
0.6
0.7
0.8
0.9
1.0
0
0.2
0.4
0.6
0.8
1
(1)
(3)
(4) (5) (6)
(a)
shape factor (B*)
higher Wm = 0.57-- 0.62
Wallis plot
1st estimate
Rc min = 1.60 – 1.70
Wm = 0.44 – 0.49
Rc max = 2.20 – 2.35
Wm = 0.66 – 0.69
2nd estimate
Rc min = 1.60 – 1.70
Wm = 0.44 – 0.49
Rc max = 1.80 – 2.20
Wm = 0.53 – 0.66
R
1
1.5
2
2.5
3
3.5
4
(b)

Figure 4-11. Comparison of RGN (a) and Wallis (b) plots for sample WS-029-I. Comparison of green dashed lines in RGN diagrams indicates the W_m ranges. Green dashed envelopes in the Wallis plot represent possible W_m estimates. Red circles indicate the data used to construct critical R_c envelopes, while green circles represent outliers.

WS-029-I (n=129)

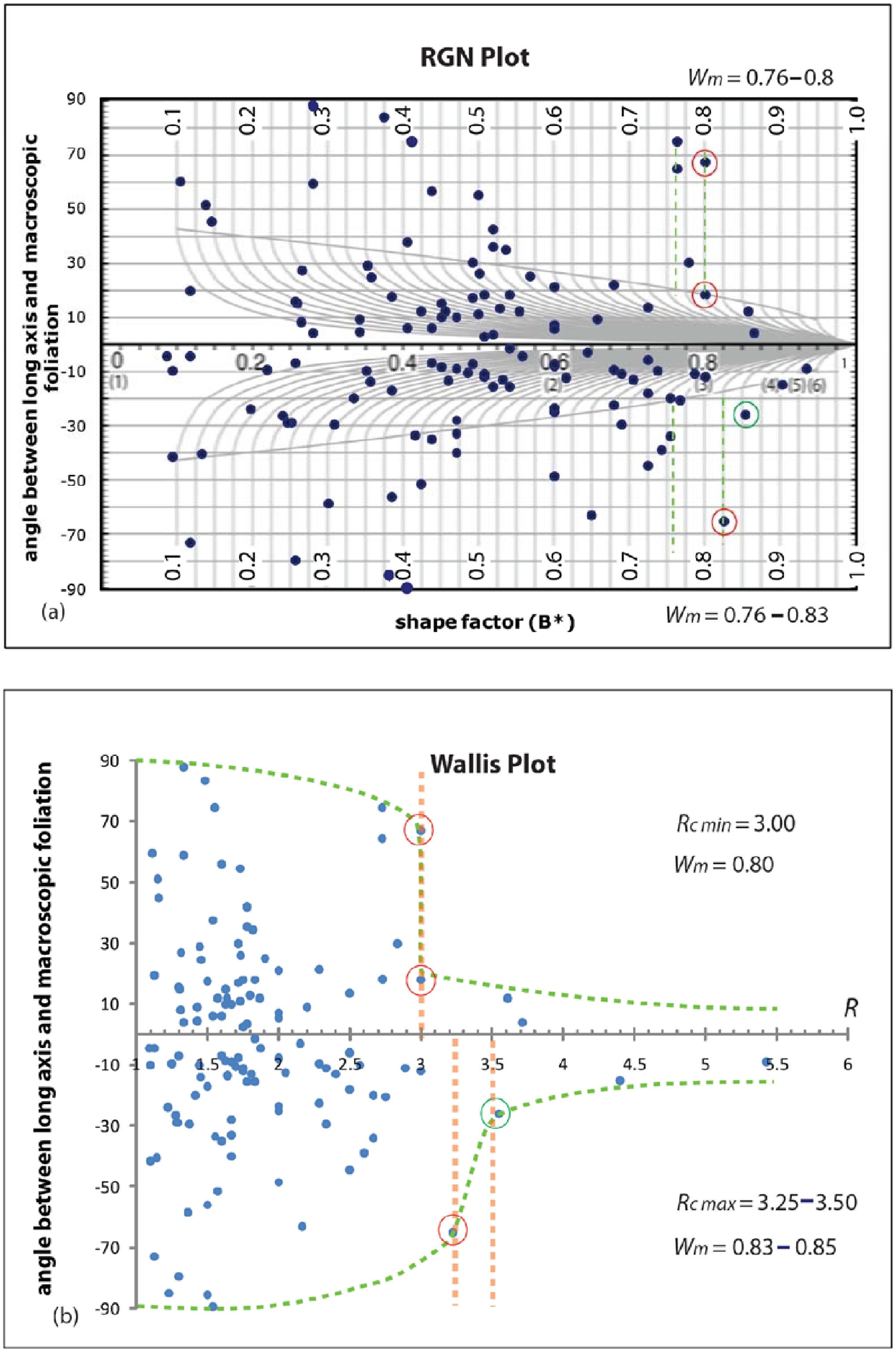
RGN Plot
Wm = 0.76–0.8
angle between long axis and macroscopic foliation
90
70
50
30
10
-10
-30
-50
-70
-90
0.1
0.2
0.3
0.4
0.5
0.6
0.7
0.8
0.9
1.0
0
(1)
(2)
(3)
(4)
(5)
(6)
1
(a)
shape factor (B*)
Wm = 0.76 – 0.83
Wallis Plot
Rc min = 3.00
Wm = 0.80
R
1
1.5
2
2.5
3
3.5
4
4.5
5
5.5
6
Rc max = 3.25–3.50
Wm = 0.83 – 0.85
(b)

CHAPTER V

DISCUSSION

RELEVANCE TO BREVARD FAULT ZONE HISTORY

Neoacadian W_k vs. Early Alleghanian W_m

Merschat et al. (2005) and Hatcher and Merschat (2006) suggested that the NBFZ is the result of tectonically forced channel flow, thus, a wider range of W_m is expected (Williams et al., 2006). W_m would be considerably lower in the center of the channel than at the flow boundaries (Jiang and White, 1995; Williams et al., 2006). Merschat et al. (2005) reported W_m ($\alpha = 42^o$; $W_k = 0.74$) using S-C and C-C' data to estimate the W_k in the NBFZ. However, the eABFZ, a buttress zone (Hatcher, 2001), experienced high simple shear (Hatcher, pers. comm.), compared to the NBFZ. Therefore, the ratio of pure and simple shear of the NBFZ should be interpreted using a "non-steady-state" curve (see Fig. 1-2). It consists of about 46 percent pure shear, but an average W_k value is not well represented by NBFZ kinematics, and it simplifies the "pattern" of deformation processes.

A kinematic vorticity pattern in the IP (Fig. 5-1a) provided by A. J. Merschat (in preparation) was plotted with respect to the distance from the BFZ. The average mesoscopic W_k pattern of the NBFZ (Fig. 5-1b) (A. J. Merschat, pers. comm. unpublished data) demonstrates a well-defined flow pattern, showing

Figure 5-1. W_k pattern of the NBFZ and IP, L_2 mineral lineation. (a) W_k was estimated from the L_2 mineral lineation (Hatcher, 2001; Merschat et al., 2005, and references therein). Purple lines represent traverses along which the W_k pattern that was determined across the NBFZ (lines provided by A. J. Merschat). Orange block indicates approximate study area. (b) X-axis: distances (in km) from BFZ buttress SE across the IP. Y-axis: mesoscopic W_k average patterns. In order to compare W_m of eABFZ in the study area and the W_k patterns in the NBFZ, different color schemes were used to differentiate lines 1 to 7. Lines 1 to 4: black lines and square points. Line 5: blue line with star symbols. Line 6: brown line with open circles. Line 7: black line with open squares. Same color scheme was used for lines 5, 6, and 7 in Figure 5-2.

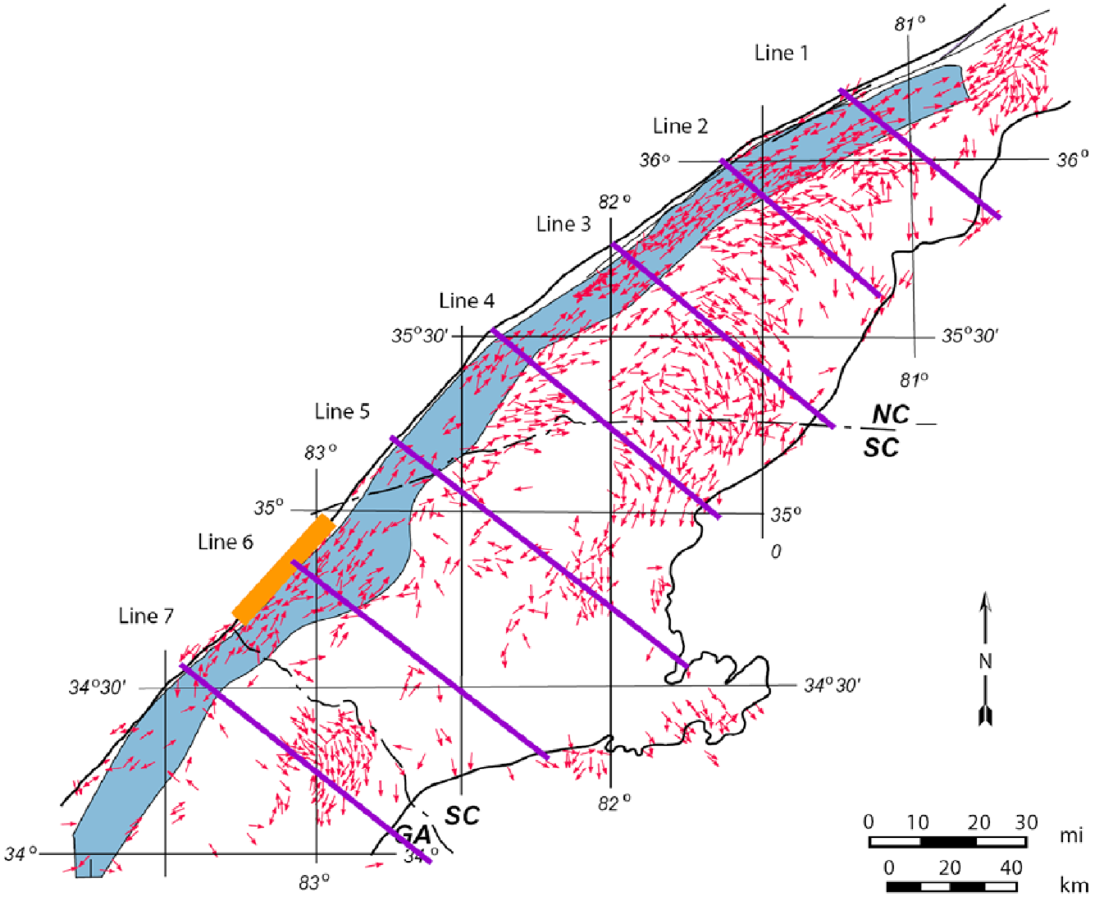

Line 1
Line 2
Line 3
Line 4
Line 5
Line 6
Line 7
81°
36°
36°
82°
35°30'
35°30'
81°
NC
SC
83°
35°
35°
0
34°30'
34°30'
82°
SC
GA
34°
34°
83°
N
0 10 20 30 mi
0 20 40 km

(a)

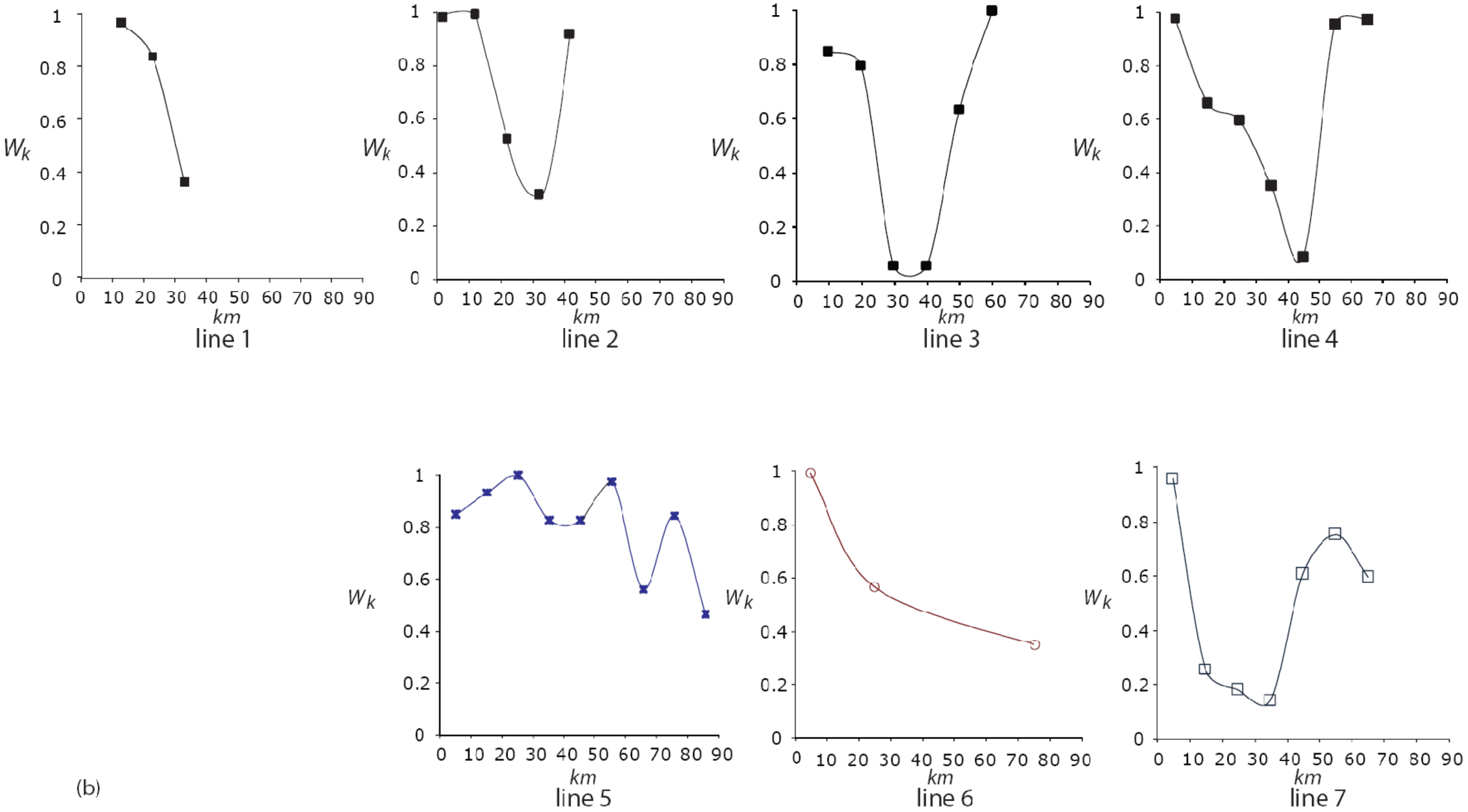

line 1

line 2

line 3

line 4

line 5

line 6

line 7

(b)

the lower W_k values at the center portion of the flow regime, and the higher W_k values in the buttress zone. These average W_k patterns display asymmetry (Fig. 5-2, lines 1, 2, 4, 6, and 7) and multiple leading edge behavior (Fig. 5-2, lines 3 and 5). The W_k curve patterns embody both heterogeneous and anisotropic behavior.

The NBFZ flow pattern, however, does not appear on the narrow eABFZ. Lines 5, 6, and 7 are close to the study area; a combination of W_m results (from this study) and average W_k patterns were plotted to demonstrate the kinematic differentiation between NBFZ and eABFZ (Fig. 5-3). The plot shows that a mesocopic average W_k pattern is close to 1 at the shear zone boundary of the NBFZ. The W_m eABFZ estimates from the study area are lower than the average W_k of the NBFZ buttress zone. The lower range of W_m of the eABFZ is the result of reactivation; the buttress zone underwent extremely high simple shear during the Neoacadian event and subsimple to simple shear during early Alleghanian reactivation. The comparison also indicates the tectonic evolution of the BFZ from the Neoacadian to the early Alleghanian.

It is essential to mention that curving lines are used to illustrate these W_k average patterns over the histogram for the following reasons. 1) The curved lines represent the continuity of the channel-flow behavior. 2) A gradually developing smooth pattern embodies the crustal evolution and it is also observed in mesoscale mineral lineation. Nevertheless, these average W_k patterns also illustrate the similarity of sheath fold features. Therefore, these smooth curves would provide a plausible interpretation. However, numerous data gaps affected

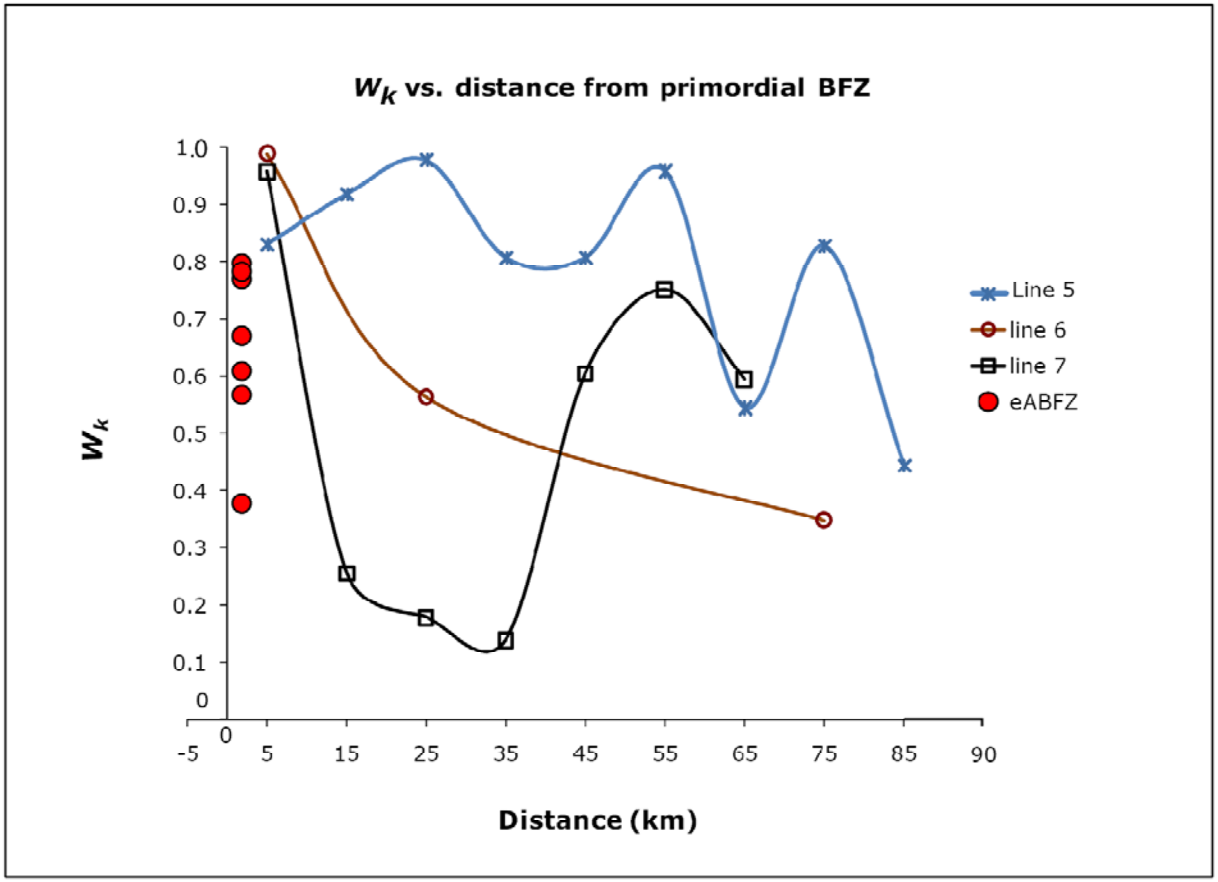

Figure 5-2. Kinematic vorticity comparison. Mesoscopic W_k lines 5, 6, and 7 and W_m estimates of eABFZ within BFZ. Red dots circled with black indicate W_m results from the study area.

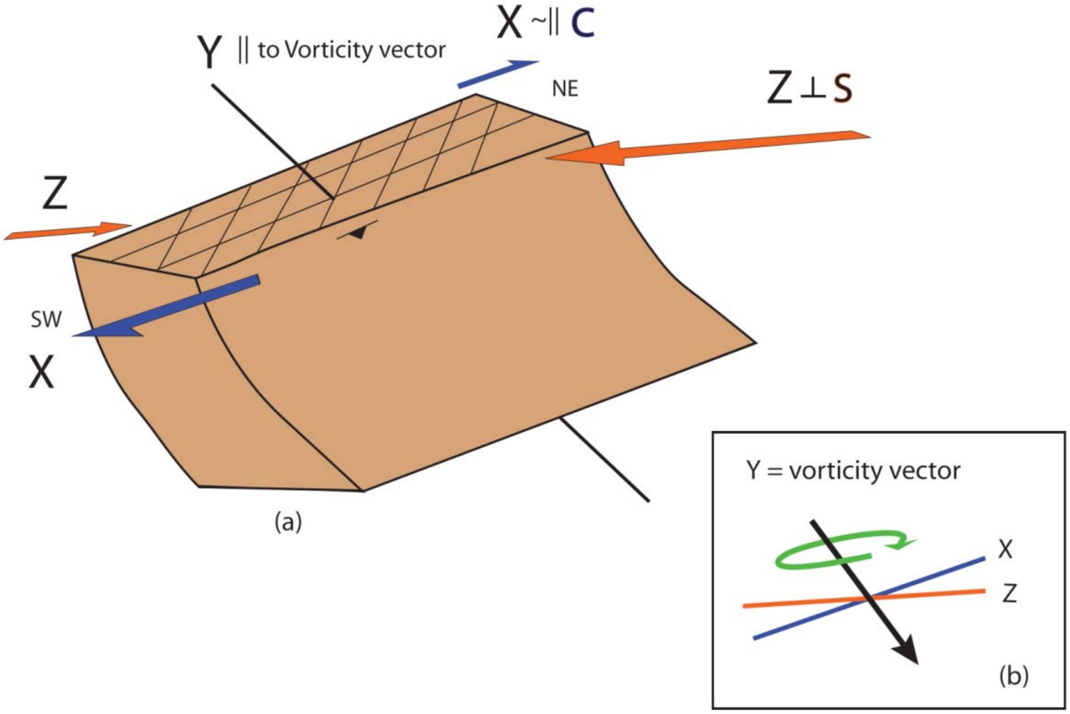

Figure 5-3. Schematic of a possible triclinic shearing system of the eABFZ. (a) Orange and blue arrows represent simple and pure shear, respectively. Pure shear (coaxial) is oriented 45° to the shear zone boundary and perpendicular to the S fabric. Simple shear (non-coaxial) is parallel to the shear zone boundary and parallel/subparallel to the C fabric. Foliation symbol trends NE-SW and dips SE. (b) Triclinic system of the BFZ. Three axes are not perpendicular to each other. Y-axis is the vorticity vector (black line, green curve rotates clockwise, arrow indicates vorticity vector). Z-axis (orange line) is perpendicular to the S-surface. X-axis is nearly parallel to C or C' surface.

the macroscale crustal flow pattern of lines 1, 2, and 6. More mesoscale field mapping needs to be completed.

Triclinic Deformation of the High-low Pattern of W_m Values and Asymmetric W_m Values

Results from this study suggest two important points. First, W_m estimates are higher parallel toward the displacement direction (SW direction). In an asymmetric kinematic framework, the active block has moved and undergone greater simple shear (Fig. 5-3). A higher W_m was recorded parallel to the displacement direction. This asymmetric W_m pattern should be examined and confirmed with other reactivated tectonic settings, such as reactivated Hebrides fault zone in Scotland (Imber et al., 1997). The possible displacement related to the difference between higher and lower W_m remains unknown.

Second, the W_m estimates occur in a high-low pattern. The most likely cause of this pattern is triclinic deformation. The mechanically heterogeneous rock types within the BFZ may trigger this triclinic shear mechanism. Also, this high-low pattern of W_m values is also reflected in lithologic units (Fig. 5-4). The kinematic framework of the eABFZ was dominated by subsimple to simple shear and steady-state flow, which occurred near the brittle–ductile transition.

A relatively symmetric and nearly constant W_m pattern would be expected in a monoclinic system. Also, W_m values in the YZ-plane would be less than the

Figure 5-4. High-low pattern of W_m values in the XZ-plane on the map (Tamassee and Whetstone quadrangles, SC) (after Hatcher et al., 2000). Blue boxes indicate samples were collected from the same localities with a 1.5 to 2 m interval. W_m value in black indicates samples were collected from the MHG unit. W_m value in blue indicates the sample was collected from the mylonitic gneiss unit. W_m value in green indicates the sample was collected from phyllonite. See Figure 1-5 for explanation of map symbols (Hatcher et al., 2000).

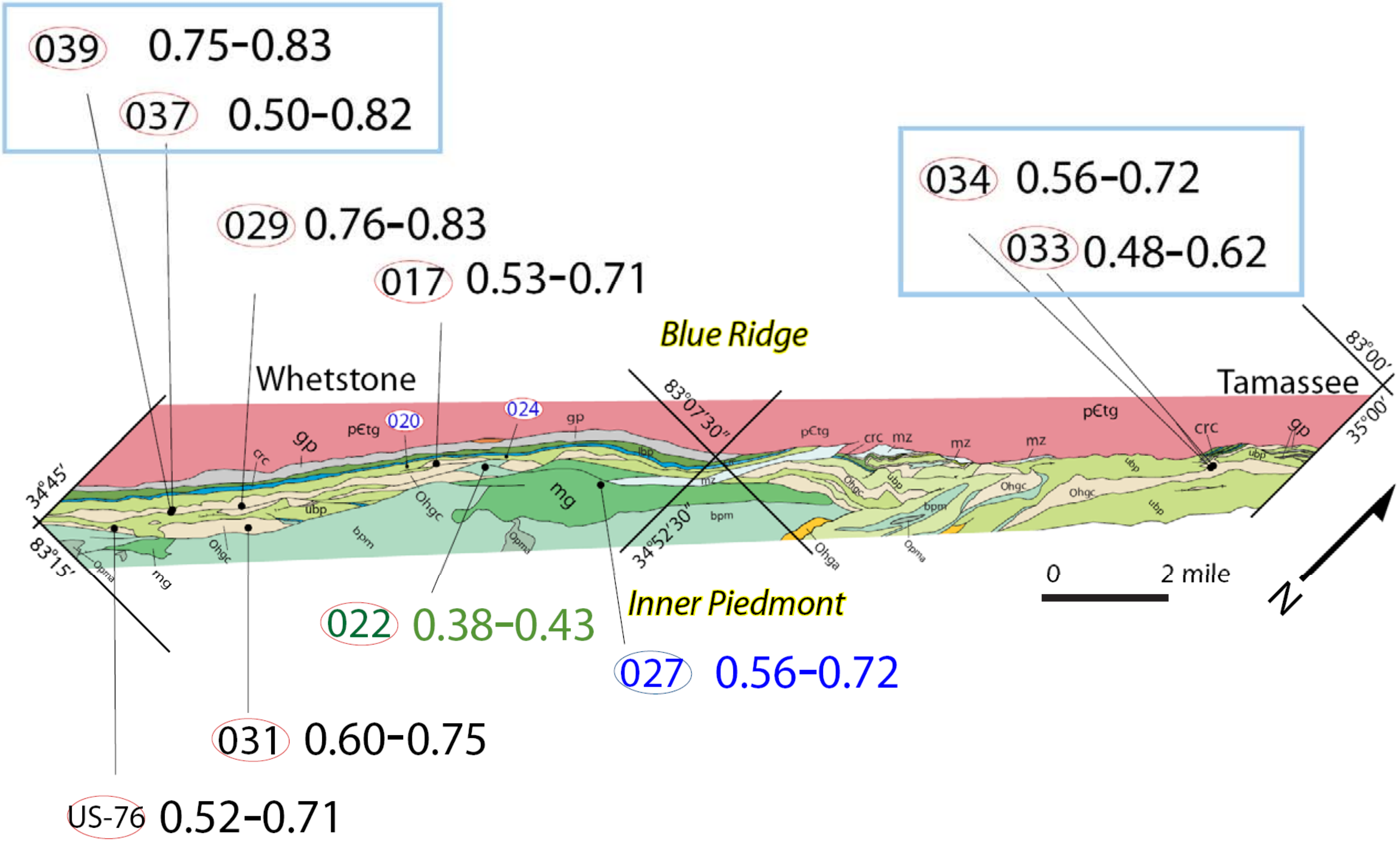
039 0.75-0.83
037 0.50-0.82
029 0.76-0.83
017 0.53-0.71
034 0.56-0.72
033 0.48-0.62
Blue Ridge
Whetstone
Tamassee
83°00′
35°00′
83°07′30″
34°52′30″
34°45′
83°15′
pЄtg
020
024
gp
crc
ubp
bpm
Ohgc
mg
Opma
ibp
mz
pCtg
Ohga
0
2 mile
N
Inner Piedmont
022 0.38-0.43
027 0.56-0.72
031 0.60-0.75
US-76 0.52-0.71

XZ-plane. To summarize, my results suggest a triclinic shear mechanism and heterogeneous lithology of the retrograde BFZ may have influenced the W_m estimates producing high-low patterns.

In contrast, polydeformation may also affect the triclinic deformation in the BFZ. Late Alleghanian brittle deformation caused an oblique thrust motion and produced the out-of-sequence Rosman thrust fault (Hatcher, 2002). The combination of early and later Alleghanian events could have yielded a “triclinic” deformation system, as seen in the mesoscopic scale as well as in the microscale.

Problems with Vorticity Estimates and Quartz *C*-axis Measurements

For the purpose of convenience, I used the terms XZ- and YZ- section to describe the section perpendicular to foliation and parallel to lineation, and perpendicular to foliation and lineation, respectively. In fact, the foliation is a C-surface, so it is not parallel to the XY-plane (Fig. 5-5). Monoclinic deformation and plane strain are invalid assumptions in a triclinic system. However, this study was completed by measuring the parameters, including long and short axes of clasts and angles between dominant foliation and long axes, which involved rotation of rigid clasts at the thin section scale. Subsequently, a monoclinic shear system and plane strain were assumed at the microscale.

Thin sections for quartz *c*-axis measurements were also prepared with the assumption of plane strain. Actually, triclinic deformation was observed on both the micro- and mesoscales. If the retrograde BFZ is a result of a monoclinic shear mechanism, all W_m estimates from the YZ-plane (the section

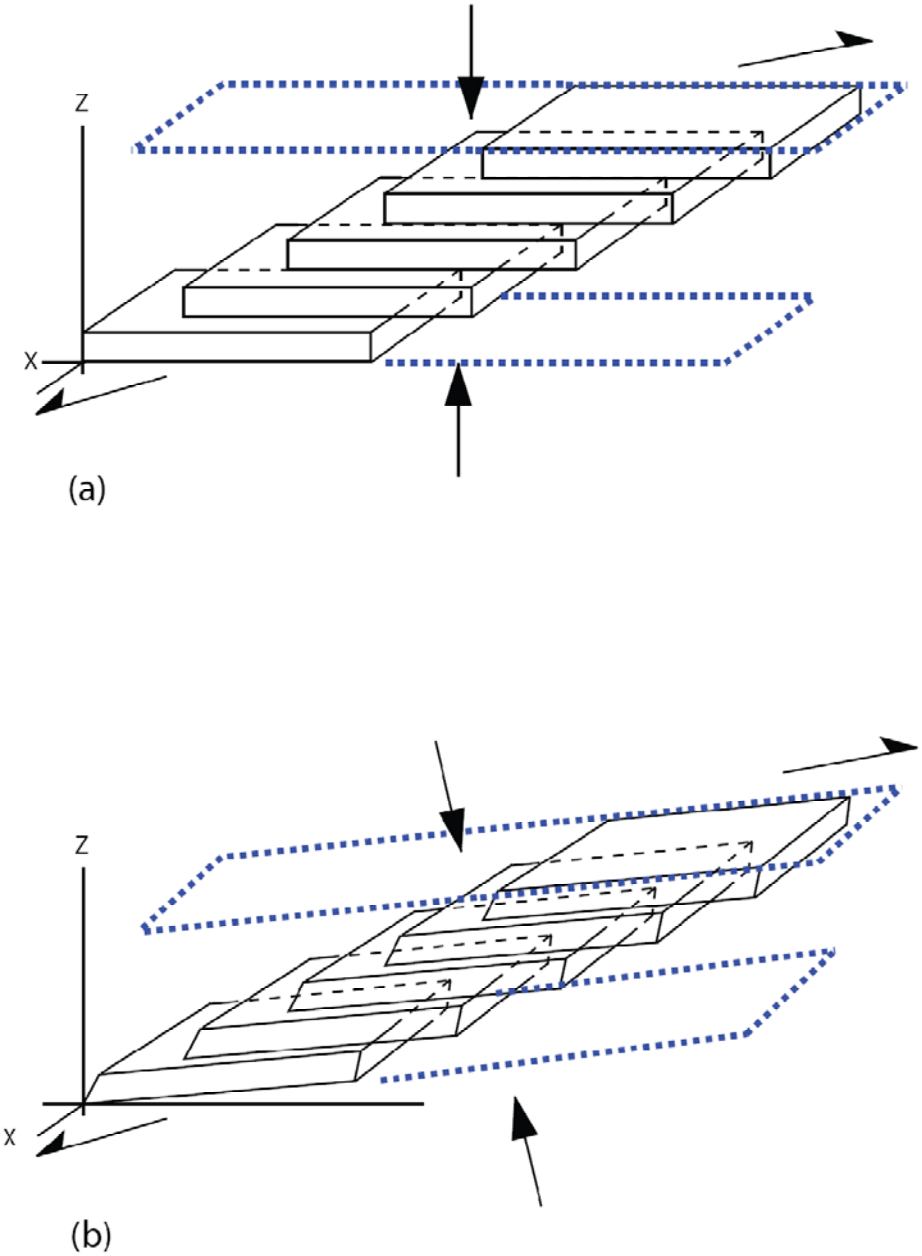

Figure 5-5. Schematic of the plane strain assumption vs. a real triclinic system. (a) Samples prepared in XZ- and YZ- plane. (b) In reality, the XY-plane is not parallel to the dominant foliation.

perpendicular to foliation and lineation) would be zero. In fact, most W_m estimates from this study are non-zero.

Additionally, two factors would affect not only vorticity measurements, but also the kinematic interpretation: 1) clast shape (e.g. oblique and irregular clasts) may also increase the uncertainty of measurements. For instance, a section may cut an oblique clast or obliquely cut through elliptical grain. These factors would affect R (aspect ratio) and the measured angles. 2) All RGN plot comparisons were not made from the same population size. In natural systems, many factors cannot be controlled, such as the number of "usable clasts." These factors all play an essential role in kinematic interpretations.

Problems with Quartz *C*-axis Opening Angles vs. Deformation Temperature

Although Kruhl (1998) and Law et al. (2004) suggested that *c*-axis opening angles were associated with deformation temperature, there are neither empirical nor theoretical equations available to confirm the deformation temperature. A sample from Rongbuk Valley, Tibet (see chapter III, quartz *c*-axis calibration) displays a high temperature at regime II to III (Hirth and Tullis, 1992). Hence, the quartz *c*-axis opening angles cannot be employed to infer the deformation temperature directly.

To estimate the deformation temperature, the petrofabric observations and *c*-axis patterns were equally essential. For instance, quartz *c*-axis opening angles (45–47 degrees) of sample WS-037-I were estimated at a low to medium temperature (~360 ± 60 ^{o}C) regime; and the quartz grains underwent nearly grain-boundary migration recrystallization related to medium temperatures (400–500 ^{o}C) (Hirth and Tullis, 1992) that were observed from thin section. Deformation lamellae were also observed, which are related to low-grade deformation conditions below 300 ^{o}C. With this evidence, the deformation temperature estimates would be meaningful. However, due to the reactivation, the deformation lamellae were possibly produced by a later Alleghanian event that consequently raised questions about the credibility of the deformation temperature estimates.

With well-controlled laboratory conditions, Hirth and Tullis (1992) employed experimental approaches to define the relationships between stress, strain rate, temperature, and water on deforming quartz grains, and they separated deformed quartz into three regimes. However, it was complicated to configure a laboratory model to match the natural deformation pathway, especially in such a polydeformed shear zone as the BFZ. Applying quartz *c*-axis opening angles and deformation regimes to establish the deformation temperature may introduce a significant error. Therefore, *c*-axis opening angles and deformation regimes data contributed to understanding the deformation history.

Mesoscopic Fabric and Quartz *C*-axis Diagrams

In order to confirm the results of the quartz *c*-axis measurements, mesoscopic fabric diagrams were plotted using foliation and lineation data from the retrograde Brevard fault zone in the Whetstone and Tugaloo Lake quadrangles, SC (Fig. 5-6 and 5-7) (Hatcher et al., 2000). Poles to the dominant mylonitic foliation yield a great circle at 33.2^{o}, 29.4^{o} E that agrees with top-to-the SW shear sense (see Fig. 4-8) obtained from quartz *c*-axis data. Results suggest that mesofabric data (S-C or C-C') are also valuable to estimate W_k, as stated in Chapter III. Ideally, data from meso- and micro-fabrics can be compared to validate measurements.

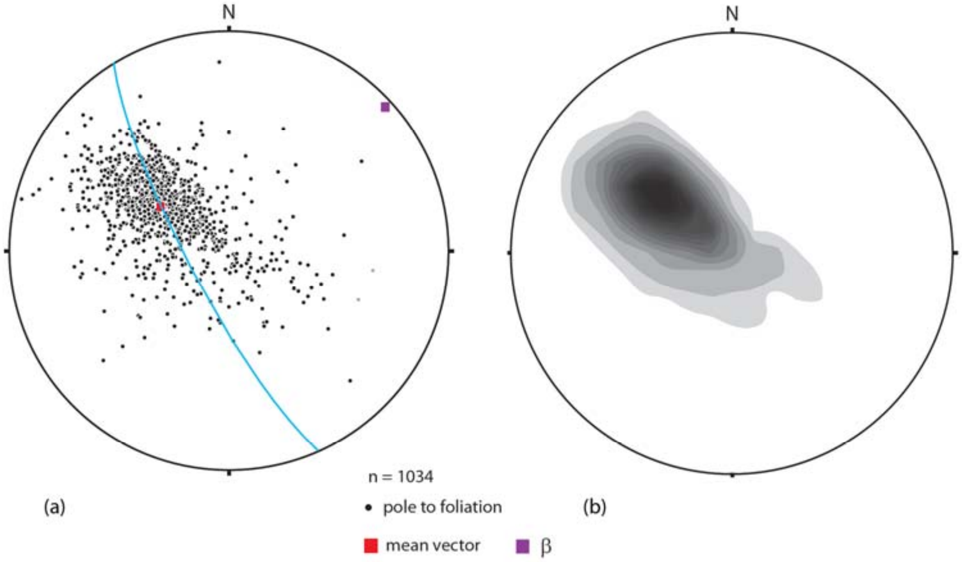

Figure 5-6. Poles to foliation of poles to foliation from Whetstone and Tugaloo Lake quadrangles, SC. (a) Scatter plot and (b) Kamb contours at an interval of 1% equal area. Solid square in red: mean vector (303.4^{o}, 61.1^{o}). Solid square in purple: β axis (36.1^{o}, 1.4^{o}).

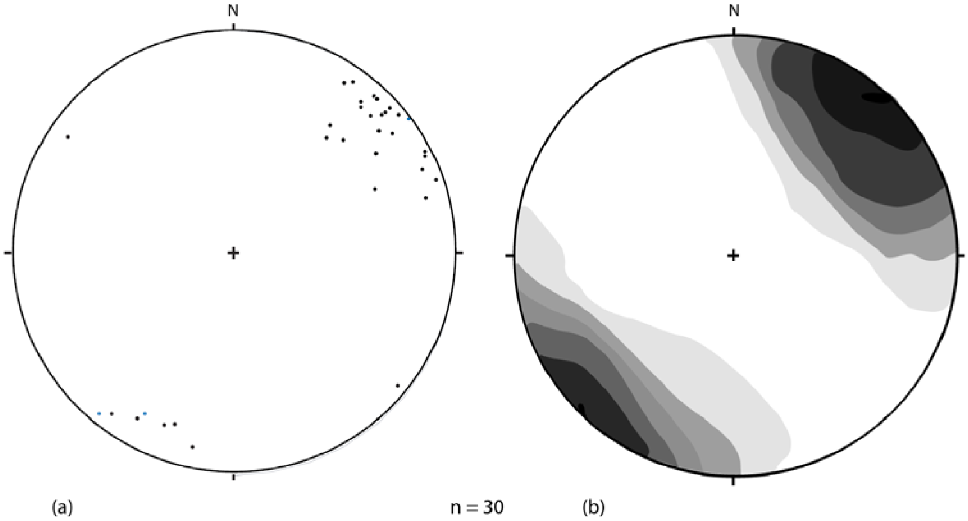

Figure 5-7. Plot of lineation data from Whetstone and Tugaloo Lake quadrangles, SC. (a) Scatter plot and (b) Kamb contour at an interval of 2σ.

CHAPTER VI

CONCLUSIONS

1. Greenschist facies rocks in the BFZ preserve evidence of reactivation during the early Alleghanian orogeny. At the same time, early Alleghanian reactivation increased the level of difficulty in deciphering the displacement and deformational geometry during this event. Kinematic analysis is a valuable method of decoding orogenic evolution.
2. Results of estimating W_m using RGN indicate the higher W_m is parallel to the transport direction. The credibility of data also has been improved by systematic measurement and well-documented sample orientation.
3. The high-low pattern of the W_m along the BFZ and additional YZ-sections, and comparison of differences, provide another line of evidence: a triclinic shear system was involved during the ductile reactivation when Gondwana collided with Laurentia.
4. Difference of mesoscopic W_k (NBFZ) patterns and the study result (eABFZ) suggest that relatively higher pure shear was involved during the early Alleghanian reactivation rather than Neoacadian.
5. Quartz *c*-axis diagrams suggest that high-T *c*-axis patterns were inherited from previous events during the Neoacadian orogeny, and retrograde deformation did not mask the evidence of previous deformation. Also, it may imply that the MHG has experienced more strain during the early Alleghanian orogeny.

FUTURE RESEARCH

Results of this research helped move us one step closer to understanding the reactivated BFZ and the parts of the BFZ deformational evolution. To complete a macroscale framework of the kinematic analysis, three lines should be emphasized in future research: (1) Systematic data collection is critical not only in the field but also in the lab. Intensive microscale research along the BFZ is needed to reconstruct the early Alleghanian orogeny and kinematic mechanisms. (2) Determination of the displacement from higher and lower W_m ranges. Kinematic vorticity analyses have been used for decades, yet no detailed solution has been made of the amount of displacement relative to W_m ranges. It is important to link estimates of W_m values with the possible displacement using both empirical and theoretical approaches. (3) Kinematic analyses should be compared to other similar tectonic settings. This project was the first application of kinematic vorticity to a multiply-reactivated large fault zone. To improve conceptual models, kinematic analyses results and comparisons are needed from reactivated regions.

REFERENCES CITED

Bailey, C. M., and Eyster, E. L., 2003, General shear deformation in the Pinaleno Mountains metamorphic core complex, Arizona: Journal of Structural Geology, v. 25, p. 1883-1892.

Bailey, C. M., Francis, B. E., and Fahrney, E. E., 2004, Strain and vorticity analysis of transpressional high-strain zones from the Virginia Piedmont, USA, *in* Alsop, G. I., Holdsworth, R. E., McCaffrey, K. J. W., and Hand, M., eds., Flow processes in faults and shear zones: Geological Society of London, Special Publications 224, p. 249-264.

Behrmann, J. H., and Platt, J. P., 1982, Sense of nappe emplacement from quartz *c*-axis fabrics; an example from the Betic Cordilleras (Spain): Earth and Planetary Science Letters, v. 59, p. 208-215.

Bobyarchick, A. R., 1986, The eigenvalues of steady flow in Mohr space: Tectonophysics, v. 122, p. 35-51.

Bretherton, F. P., 1962, The motion of rigid particle in shear flow at low Reynolds number: Journal of Fluid Mechanics, v. 14. p. 284-301.

Condie, K. C., and Sinha, A. K., 1996, Rare earth and other trace element mobility during mylonitization: a comparison of the Brevard and Hope Valley shear zones in the Appalachian Mountains, USA: Journal of Metamorphic Geology, v. 14, p. 213-226.

de Paor, D.G., 1988, R_f/ϕ_f strain analysis using an orientation net: Journal of Structural Geology, v. 10, p. 323-333.

Edelman, S. H., Liu, A., and Hatcher, R. D., Jr., 1987, Brevard zone in South Carolina and adjacent area: an Alleghanian orogen-scale dextral shear zone reactivated as a thrust fault: Journal of Geology, v. 95, p. 793-806.

Forte A. M., and Bailey, C. M., 2007, Testing the utility of the porphyroclast hyperbolic distribution method of kinematic vorticity analysis: Journal of Structural Geology, v. 29, p. 983-1001.

Gatewood, M. P., 2007, Tectonics of the northeastern Inner Piedmont, northwestern NC, from detailed geologic mapping, geochronologic, geochemical, and petrologic studies with structural analyses of ductile fault zone [M.S. thesis]: Knoxville, University of Tennessee, 263 p.

Griffin, V. S., Jr., 1971, The Inner Piedmont belt of the southern crystalline Appalachians: Geological Society of America Bulletin, v. 82, p. 1885-1898.

Hatcher, R. D., Jr., 1971, The geology of Rabun and Habersham counties, Georgia: Georgia Survey Bulletin 83, p. 48.

Hatcher, R. D., Jr., 2001, Rheological partitioning during multiple reactivation of the Palaeozoic Brevard fault zone, southern Appalachians, USA, *in* Holdsworth, R. E., Strachan, R. A., Magloughlin, J. F., and Knipe, R. J., eds., The nature and tectonic significance of fault zone weakening: Geological Society of London, Special Publications 186, p. 257-271.

Hatcher, R. D., Jr., 2002, Alleghanian (Appalachian) orogeny, a product of zipper tectonics: Rotational transpresive continent-continent collision and closing of ancient oceans along irregular margins, *in* Martinez Catalan, J. R., Hatcher, R. D., Jr., Arenas, R., and Diaz Garacia, F., eds., Variscan-Appalachian dynamics: The building of the late Paleozoic basement: Boulder, Colorado, Geological Society of America Special Paper 364, p. 199-208.

Hatcher, R. D., Jr., and Merschat, A. J., 2006, The Appalachian Inner Piedmont: an exhumed strike-parallel, tectonically forced orogenic channel, *in* Law, R. D., Searle, M. P., and Godin, L., eds., Channel flow, ductile extrusion and exhumation in continental collision zones: Geological Society of London, Special Publications 268, p. 517-541.

Hatcher, R. D., Jr., Acker, L. L., and Liu, A., 2000, (unpublished) Bedrock geology of the Brevard fault zone, Rainy Mountain, Whetstone, Tugaloo Lake, and Holly Springs 7.5 minute quadrangles, Georgia and South Carolina, scale 1:24,000.

Hatcher, R. D., Jr., Bream, B. R., and Merschat, A. J., 2007, Tectonic map of the southern and central Appalachians: A tale of three orogens and a complete Wilson cycle, *in* Hatcher, R. D., Jr., Carlson, M. P., McBride, J. H., and Martinez Catalan, J. R., eds., 4-D framework of continental crust: Geological Society of America Memoir 200, p. 595-632.

Hirth, G., and Tullis, J, 1992, Dislocation creep regimes in quartz aggregates: Journal of Structural Geology, v. 14, p. 145-159.

Imber, J., Holdsworth, R. E., Butler, C. A., and Lloyd, G. E., 1997, Fault-zone weakening processes along the reactivated Outer Hebrides Fault Zone, Scotland: Journal of The Geological Society, London, v. 154, p. 105-109.

Jessup, M. J., Law, R. D., and Frassi, C., 2007, The rigid grain net (RGN): An alternative method for estimating mean kinematic vorticity number (W_m): Journal of Structural Geology, v. 29, p. 411-421.

Jessup, M. J., Law, R. D., Searle, M. P., and Hubbard, M. S., 2006, Structural evolution and vorticity of flow during extrusion and exhumation of the Greater Himalayan Slab, Mount Everest Massif, Tibet/Nepal: implications for orogen-scale flow partitioning, *in* Law, R. D., Searle, M. P., and Godin, L., eds., Channel flow, ductile extrusion and exhumation in continental collision zones: Geological Society of London, Special Publications 268, p. 379-413.

Jiang, D., and White, J. C., 1995, Kinematics of rock flow and the interpretation of geological structures, with particular reference to shear zone: Journal of Structural Geology, v. 17, p. 1249-1265.

Kruhl, J. H.,1998, Reply: Prism- and basal-plane parallel subgrain boundaries in quartz: a microstructural geothermobarometer: Journal of Metamorphic Geology, v. 16, p. 142-146.

Law, R. D., 1986, Relationships between strain and quartz crystallographic fabrics in the Roche Maurice quartzites of Plougastel, western Brittany: Journal of Structural Geology, v. 8, p. 493-515.

Law, R. D., 1987, Heterogenerous deformation and quartz crystallographic fabric transitions: natural examples from the Moine Thrust zone at the stack of Glencoul, northern Assynt: Journal of Structural Geology, v. 9, p. 819-833.

Law, R. D., 1990, Crystallographic fabrics: a selective review of their applications to research in structural geology, *in* Knipe, R. J., and Rutter, E. H., eds., Deformation mechanisms, rheology and tectonics: Geology Society of London, Special Publication 54, p. 335-352.

Law, R. D., Schmid, S. M., and Wheeler, J., 1990, Simple shear deformation and quartz crystallographic fabrics: a possible natural example from the Torridon area of NW Scotland: Journal of Structural Geology, v. 12, p. 29-45.

Law, R. D., Searle, M. P., and Simpson, R. L., 2004, Strain, deformation temperatures and vorticity of flow at the top of the Greater Himalaya slab, Everest Massif, Tibet: Journal of the Geological Society of London, v. 161, p. 305-320.

Law, R. D., Morgan, S. S., Casey, M., Sylvester, A. G., and Nyman, M., 1992, The Papoose Flat Pluton of eastern California: a reassessment of its emplacement history in the light of new microstructural and crystallographic fabric observations: Transactions of the Royal Society of Edinburgh Earth Sciences, v. 83, p. 361-375.

Lin, S., Jiang, D., and Williams, P. F., 1998, Transpression (or transtension) zones of triclinic symmetry: natural example and theoretical modeling, *in* Holdsworth, R. E., Strachan, R. A., and Dewey, J. F. eds., Continental transpressional and transtensional tectonics: Geological Society of London, Special Publications 135, p. 41-57.

Lister, G. S., and Hobbs, B.E., 1980, The simulation of fabric development during plastic deformation and its application to quartzite: the influence of deformation history: Journal of Structural Geology, v. 2, p. 335-370.

Lister, G. S., and Price, G. P.,1978, Fabric development in a quartz feldspar mylonite: Tectonophysics, v. 49, p. 37-48.

Lister, G. S., and Williams, P. F., 1979, Fabric development in shear zones: theoretical controls and observed phenomena: Journal of Structural Geology, v. 4, p. 283-297.

Lister, G. S., and Williams, P. F., 1983, The portioning of deformation in flowing rock masses: Tectonophysics, v. 92, p. 1-33.

McKenzie, D. P., 1979, Finite deformation during fluid flow: Geophysical Journal International, v. 58, p. 689-715.

Means, W. D., Hobbs, B. E., Lister, G., S., and Williams, P. F., 1980, Vorticity and non-coaxiality in progressive deformation: Journal of Structural Geology, v. 2, p. 371-378.

Merschat, A. J., Hatcher, R. D., Jr., and Davis, T. L., 2005, The northern Inner Piedmont, southern Appalachians, USA: Kinematics of transpression and SW-directed mid-crustal flow: Journal of Structural Geology, v. 27, p. 1252-1281.

Passchier, C., 1987, Stable positions of rigid objects in non-coaxial flow—study in vorticity analysis: Journal of Structural Geology, v. 9, p. 679-690.

Passchier, C. W., 1988, The use of Mohr circle to describe non-coaxial progressive deformation: Tectonophysics, v. 149, p. 323-338.

Passchier, C. W., and Trouw, R. A. J., 2005, Microtectonics, 2nd ed.: Berlin Heidelberg, Springer, Inc., 394 p.

Ramberg, H., 1975, Particle paths, displacement and progressive strain applicable to rocks: Tectonophysics, v. 28, p. 1-37.

Ramsay, J. G., and Huber, M. I., 1983, The techniques of modern structural geology Vol. 1: New York, Academic Press Inc., 307 p.

Reed, J. C., Jr., and Bryant, B., 1964, Evidence for strike-slip faulting along the Brevard zone in North Carolina: Geological Society of America Bulletin, v. 75, p. 1177-1196.

Roper, P. J., and Dunn, D. E., 1973, Superposed deformation and polymetamorphism, Brevard zone, South Carolina: Geological Society of America Bulletin, v. 84, p. 3373-3386.

Simpson, C., and de Paor, D. G., 1993, Strain and kinematic analysis in general shear zones: Journal of Structural Geology, v. 15, p. 1-20.

Simpson, C., and de Paor, D. G., 1997, Practical analysis of general shear zones using the porphyroclast hyperbolic distribution method: An example from the Scandinavian Caledonides, *in* Sengupta, S., ed., Evolution of geological structure in micro- to macro-scales: London, Chapman & Hall, p. 169-184.

Sinha, A. K., and Glover, L. III, 1978, U/Pb systematics of zircons during dynamic metamorphism: Contributions to Mineralogy and Petrology, v. 66, p. 305-310.

Sinha, A. K., Hewitt, D. A., and Rimstidt, J. D., 1988, Metamorphic petrology and strontium isotope geochemistry associated with the development of mylonites: an example from the Brevard fault zone, North Carolina: American Journal of Science, v. 288, p. 115-147.

Tikoff, B., and Fossen, H., 1995, The limitations of three-dimensional kinematic vorticity analysis: Journal of Structural Geology, v. 17, p. 1771-1784.

Truesdell, C., 1954, The kinematic vorticity: Indiana University Press, Bloomington.

Wallis, S. R., 1992, Vorticity analysis in metachert from the Sanbagawa Belt, SW Japan: Journal of Structural Geology, v. 14, p. 271-280.

Wallis, S., 1995, Vorticity analysis and recognition of ductile extension in the Sanbagawa, SW Japan: Journal of Structural Geology, v. 17, p. 1077-1093.

Wells, L. M., 2001, Rheological control on the initial geometry of the Raft River detachment fault and shear zone, western United States: Tectonics, v. 20, p. 435-458.

Williams, P. F., Jiang, D., and Lin, S., 2006, Interpretation of deformation fabrics of infrastructure zone rocks in the context of channel flow and other tectonic models, *in* Law, R. D., Searle, M. P., and Godin, L., eds., Channel flow, ductile extrusion and exhumation in continental collision zones: Geological Society of London, Special Publications 268, p. 221-235.

Xypolias, P., and Doutsos, T., 2000, Kinematics of rock flow in a crustal-scale shear zone: Implication for the orogenic evolution of the southwestern Hellenides: Geologic Magazine, v. 137, p. 81-96.

Xypolias, P., and Koukouveals, I. K., 2001, Kinematic vorticity and strain patterns associated with ductile extrusion in the Chelmos shear zone (External Hellenides, Greece): Tectonophysics, v. 338, p. 59-77.

APPENDICES

Appendix A: RGN Plots for the XZ-section

Appendix B: RGN Plots for the YZ-section

Appendix C: RGN Plots for combination of XZ- and YZ- section

Appendix D: Measurements of Quartz c-axes (Trend and Plunge) from
sample WS-024-I, WS-20-I, WS-022-I, and WS-037-I

Appendix E: Deformation Temperature of WS-037-I

APPENDIX A

RGN Plots for the XZ-section

- TA-033-I
- TA-034-I
- WS-027-I
- WS-022-I
- WS-017-I
- WS-029-I
- WS-031-I
- WS-037-I
- WS-039-I
- WS-US-76-I

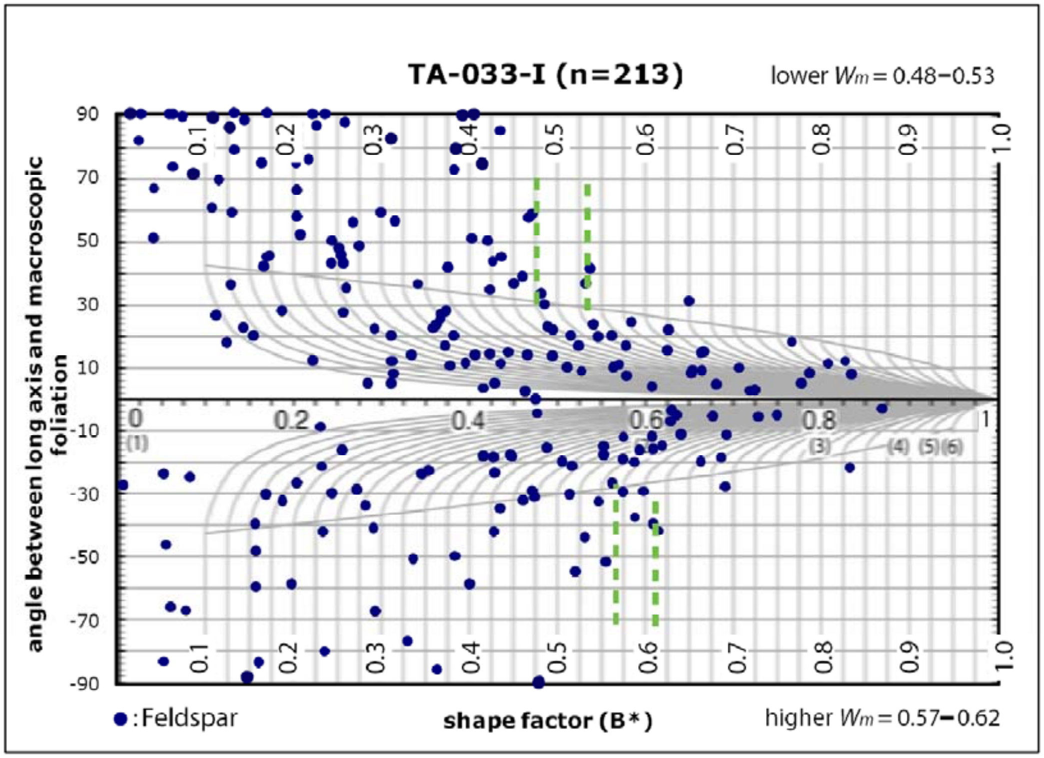

pure shear

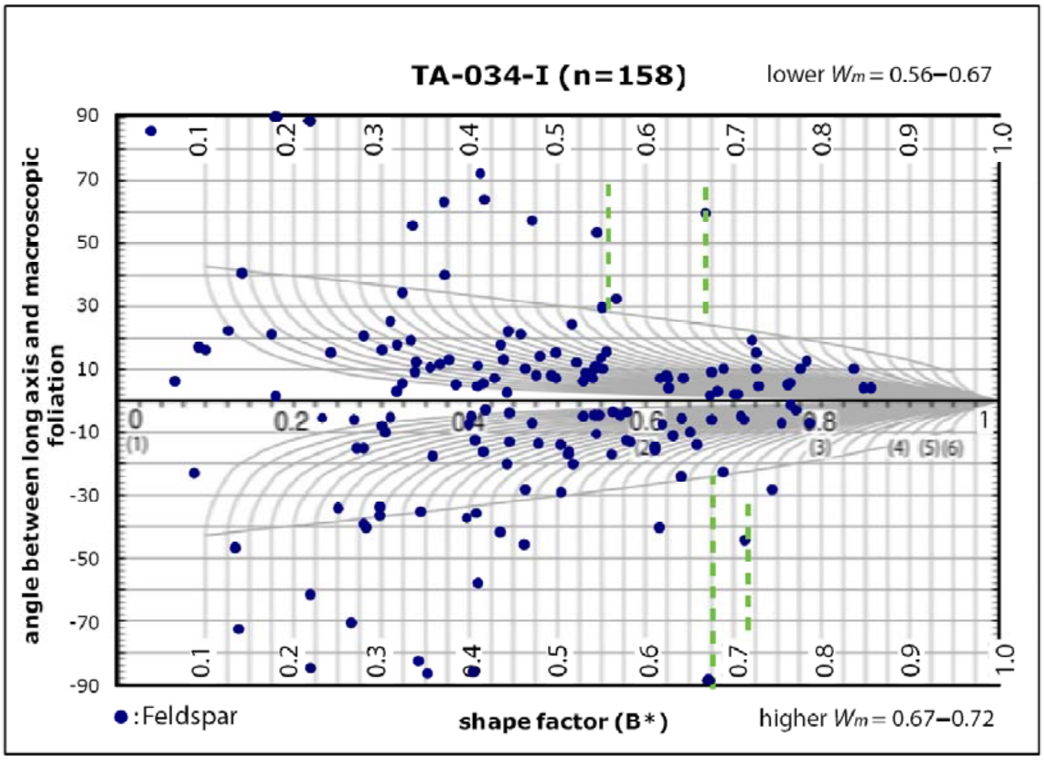

pure to sub-simple

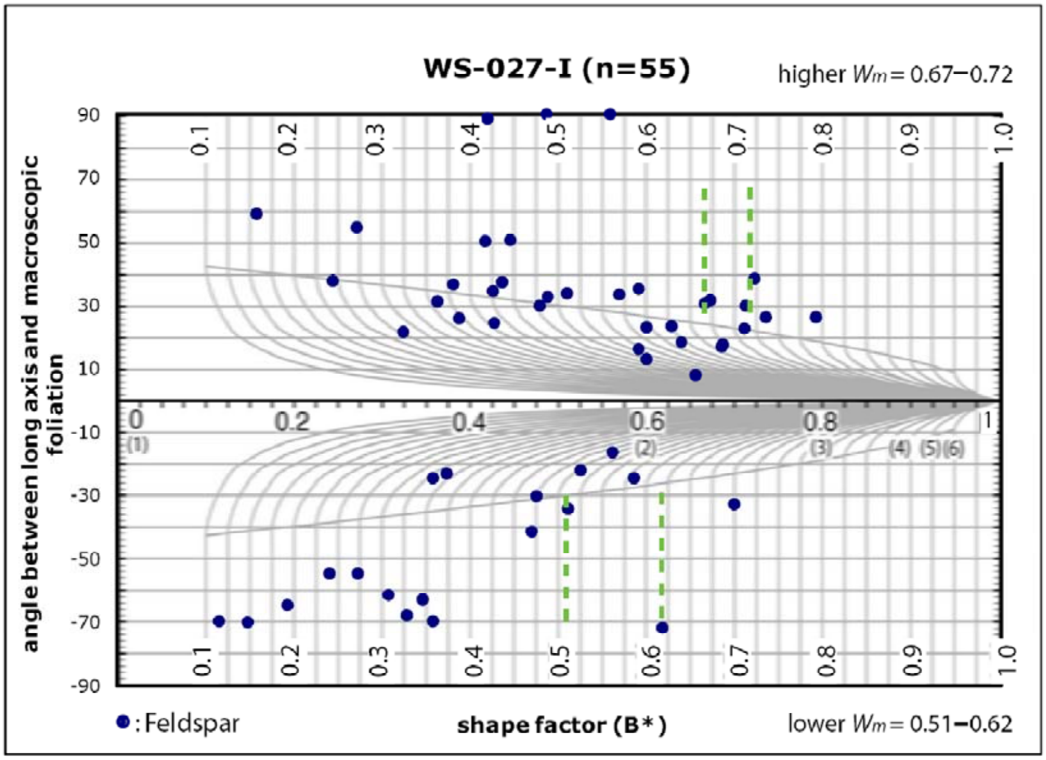

pure to sub-simple

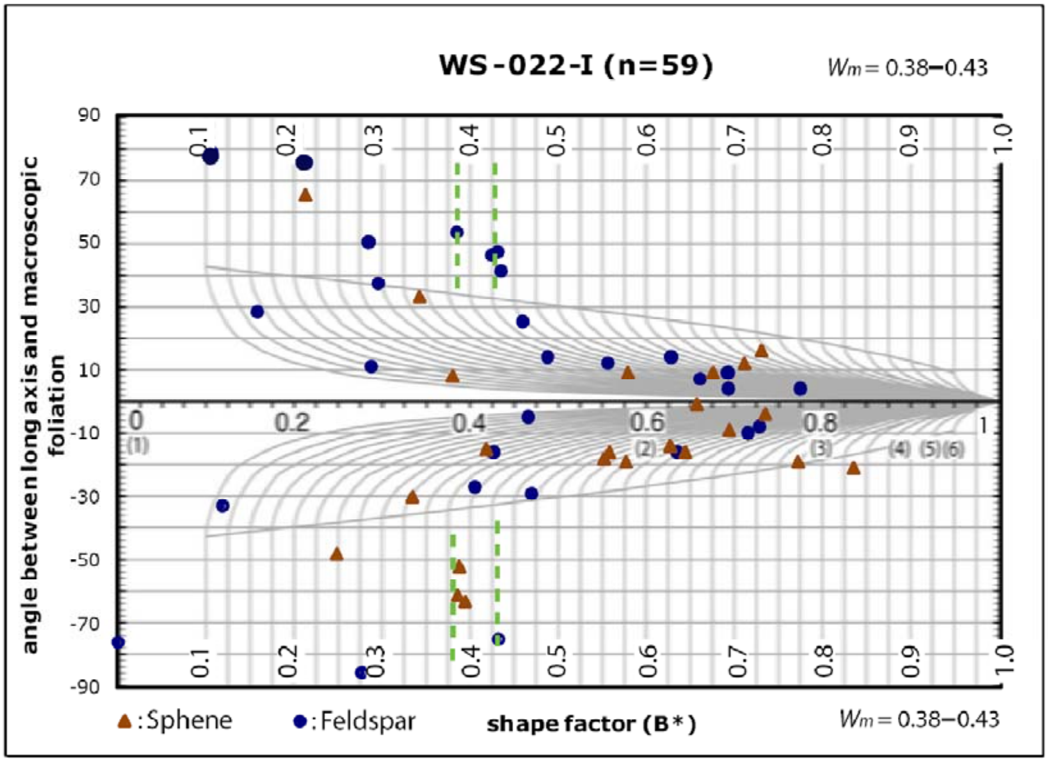

pure

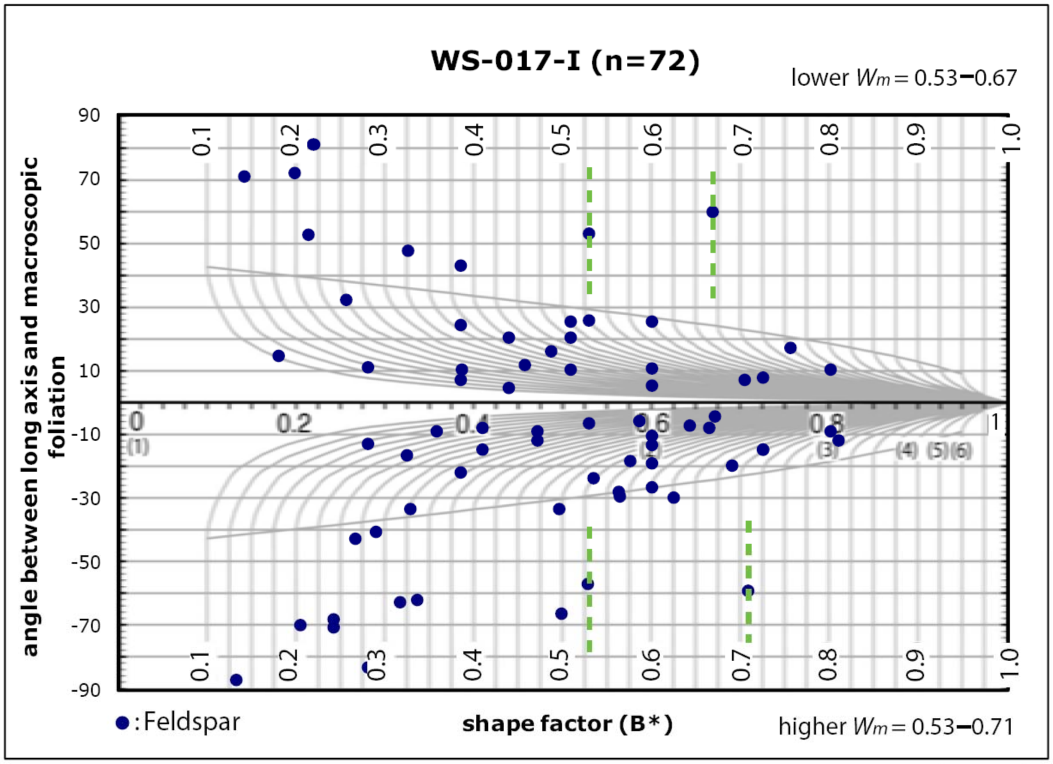

pure to sub-simple

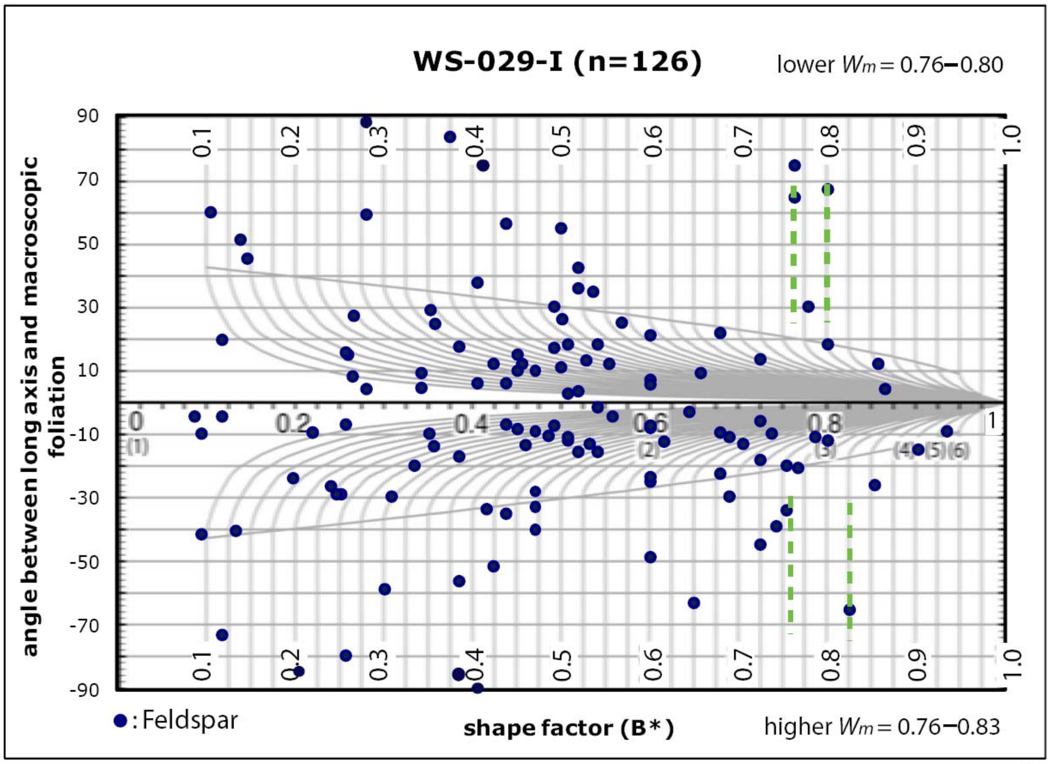

simple

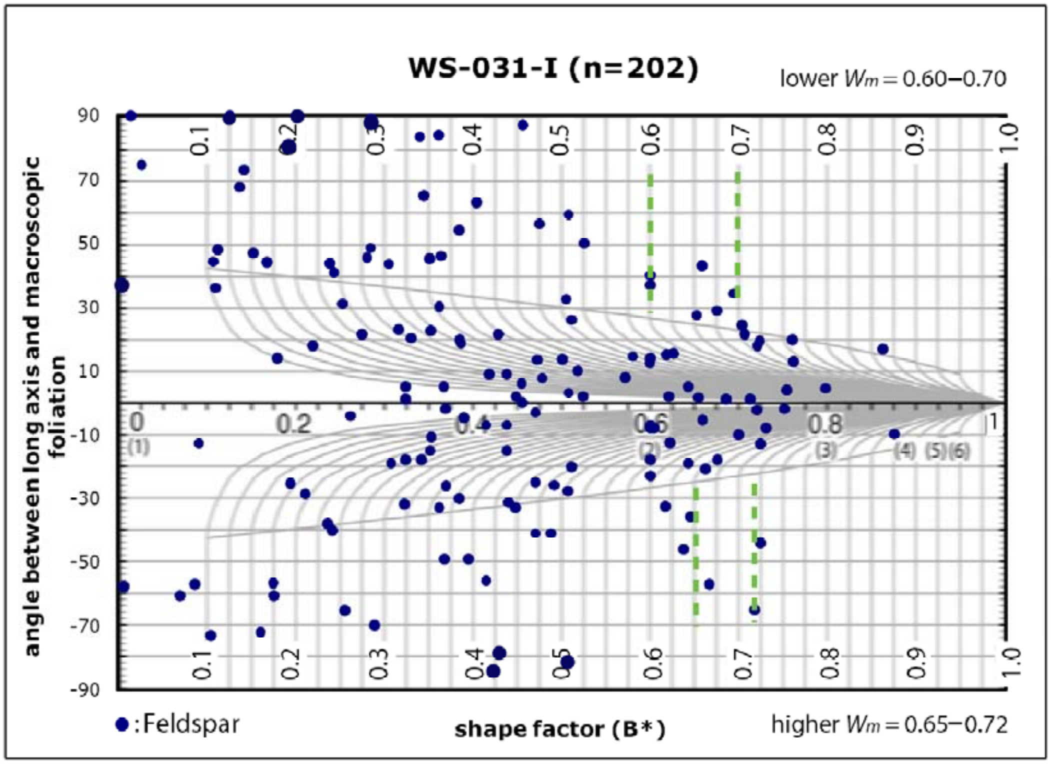

sub-simple

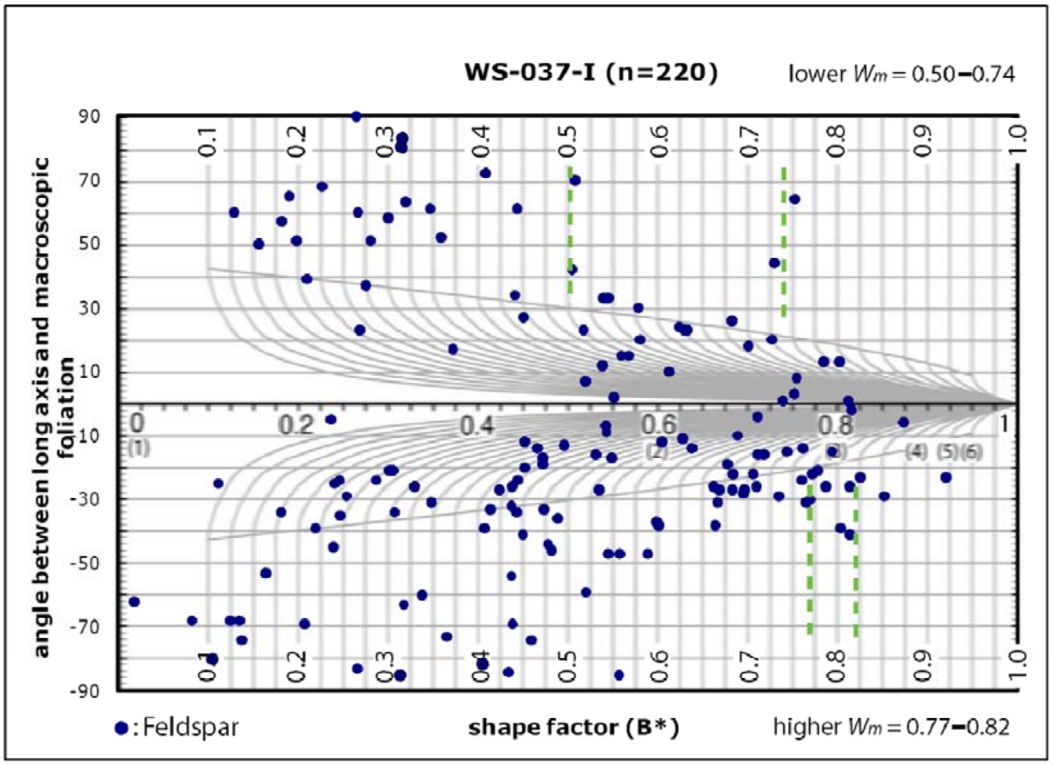

simple

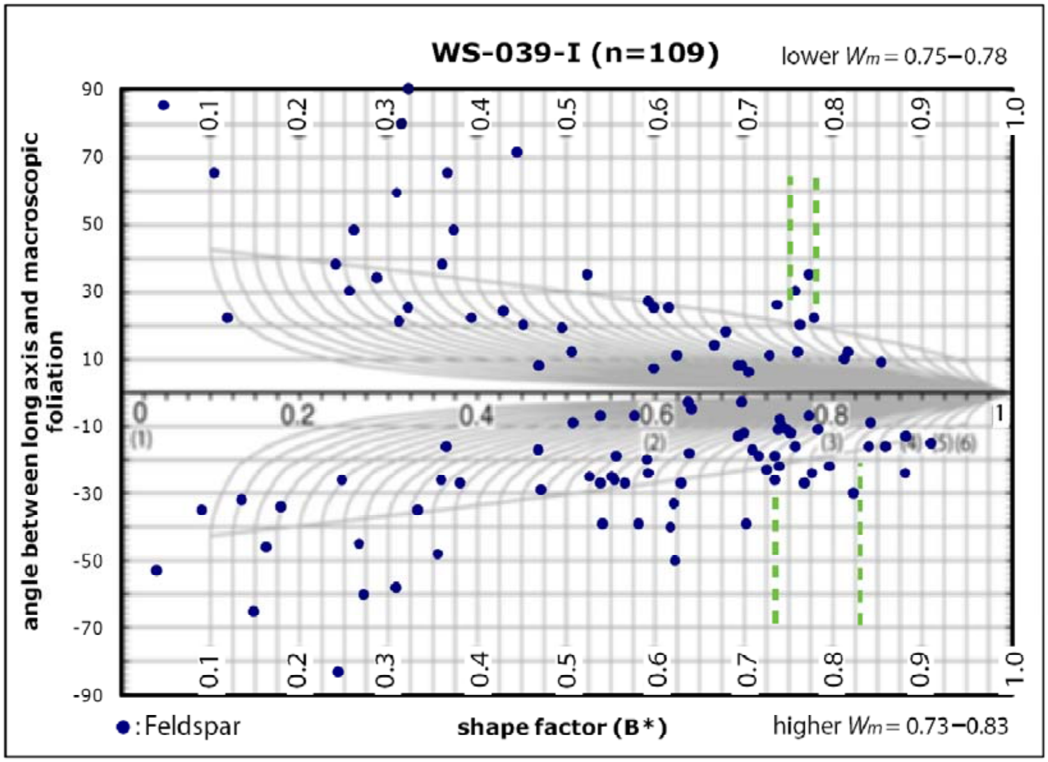

simple

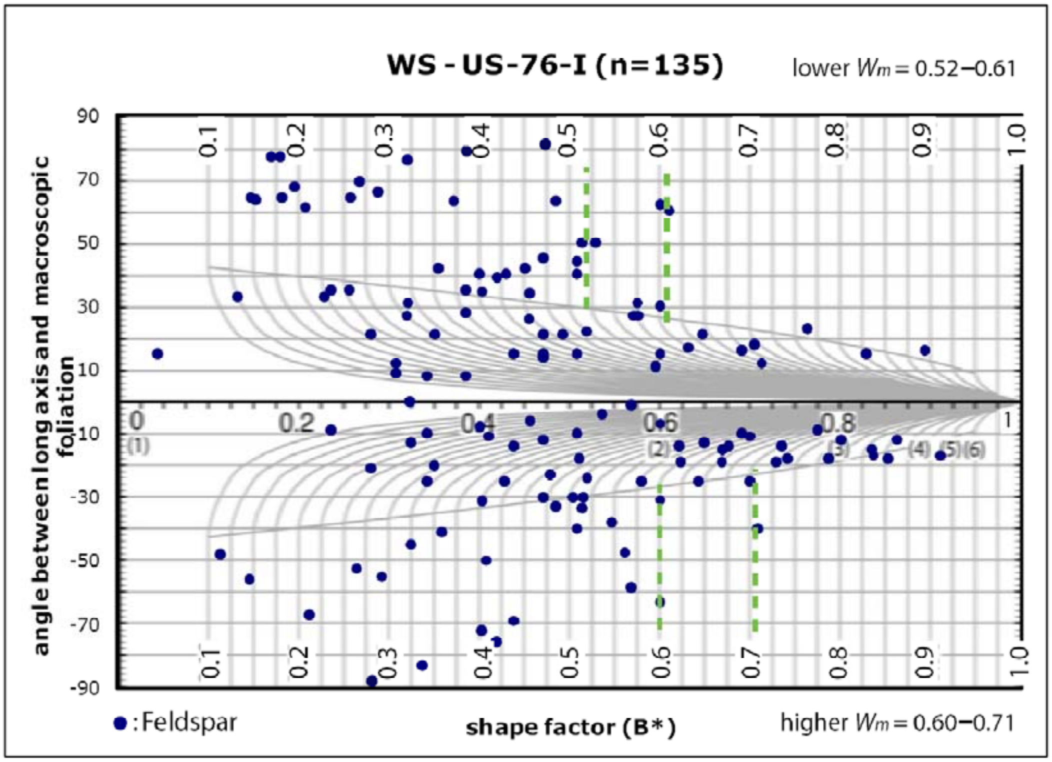

sub-simple

APPENDIX B

RGN Plots for the YZ-section

- TA-033-II
- TA-034-II
- WS-027-II
- WS-022-II
- WS-017-II
- WS-029-II
- WS-031-II
- WS-037-II
- WS-039-II
- WS-US-76-II

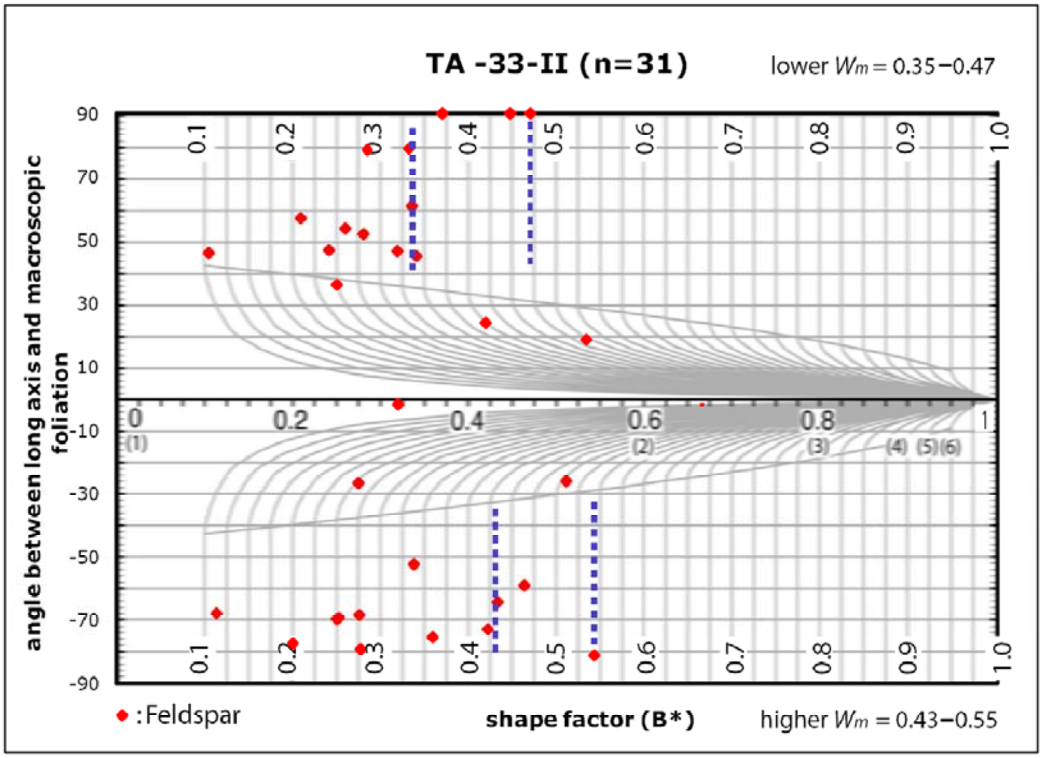

pure

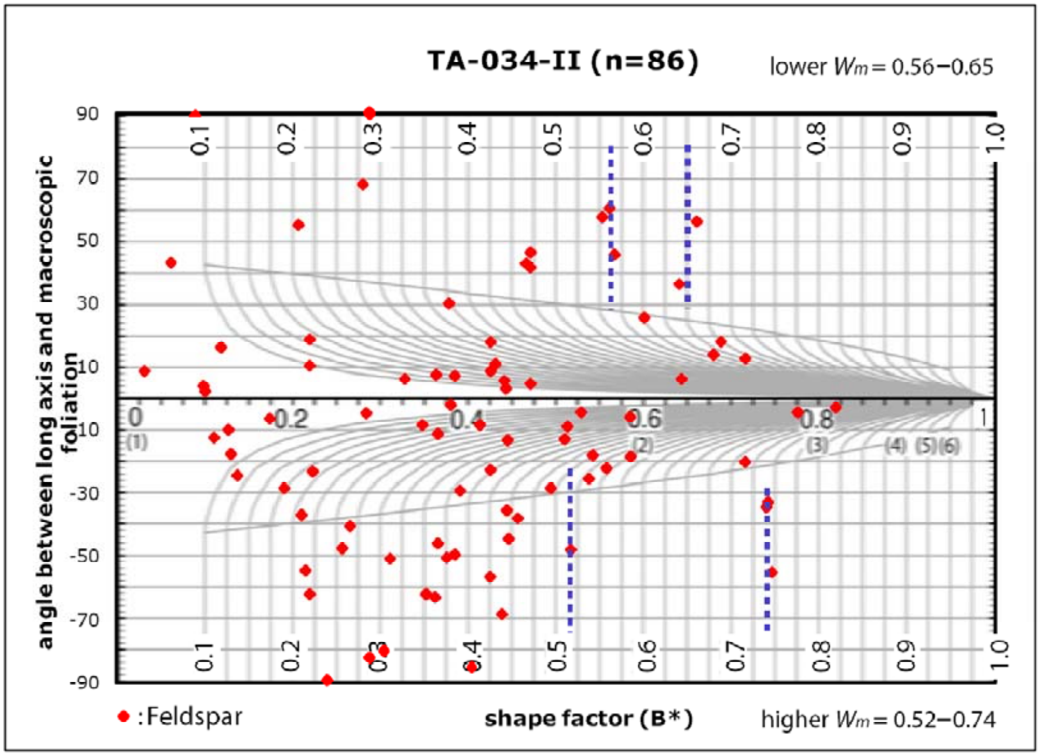

pure to sub-simple

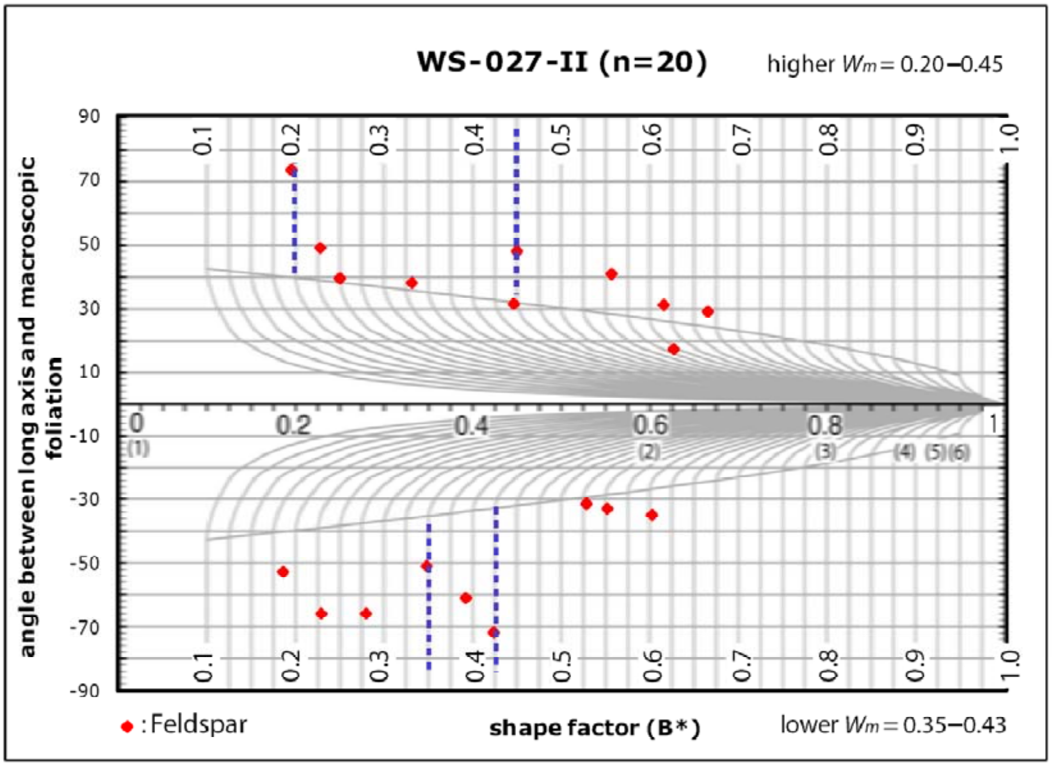
WS-027-II (n=20)
higher *Wm* = 0.20–0.45
angle between long axis and macroscopic foliation
90
70
50
30
10
-10
-30
-50
-70
-90
0.1
0.2
0.3
0.4
0.5
0.6
0.7
0.8
0.9
1.0
0
0.2
0.4
0.6
0.8
1
(1)
(2)
(3)
(4) (5) (6)
◆ : Feldspar
shape factor (B*)
lower *Wm* = 0.35–0.43

pure

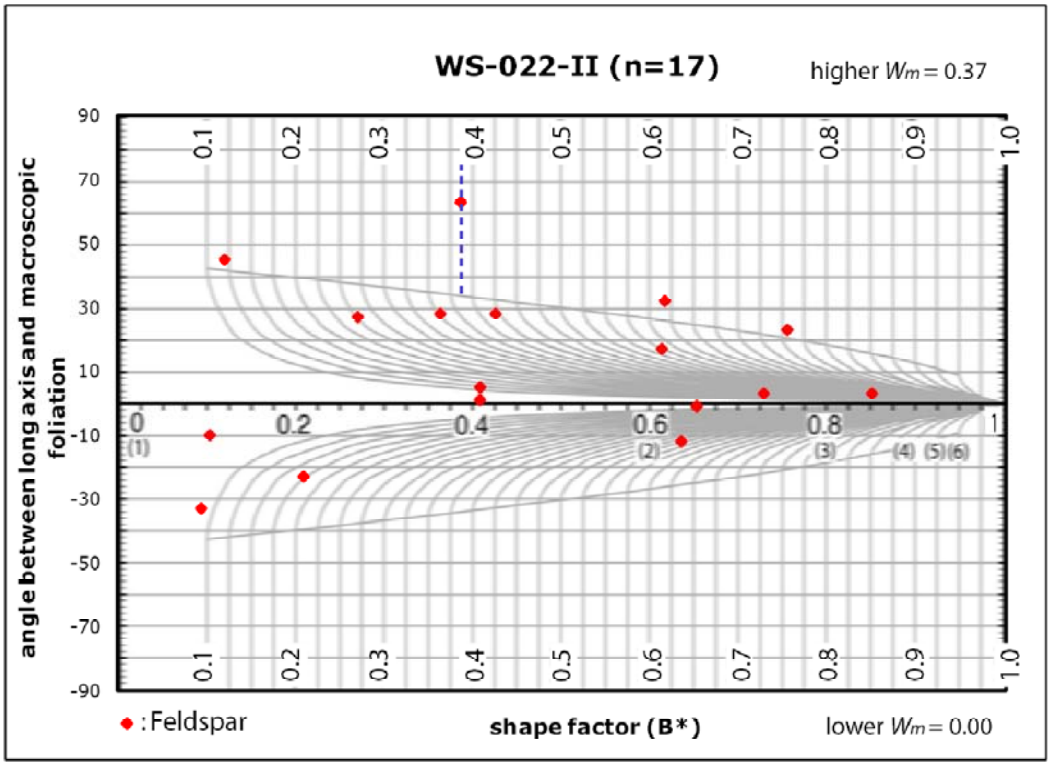
WS-022-II (n=17)
higher *Wm* = 0.37
angle between long axis and macroscopic foliation
90
70
50
30
10
-10
-30
-50
-70
-90
0.1
0.2
0.3
0.4
0.5
0.6
0.7
0.8
0.9
1.0
0
0.2
0.4
0.6
0.8
1
(1)
(2)
(3)
(4) (5) (6)
◆ : Feldspar
shape factor (B*)
lower *Wm* = 0.00

pure

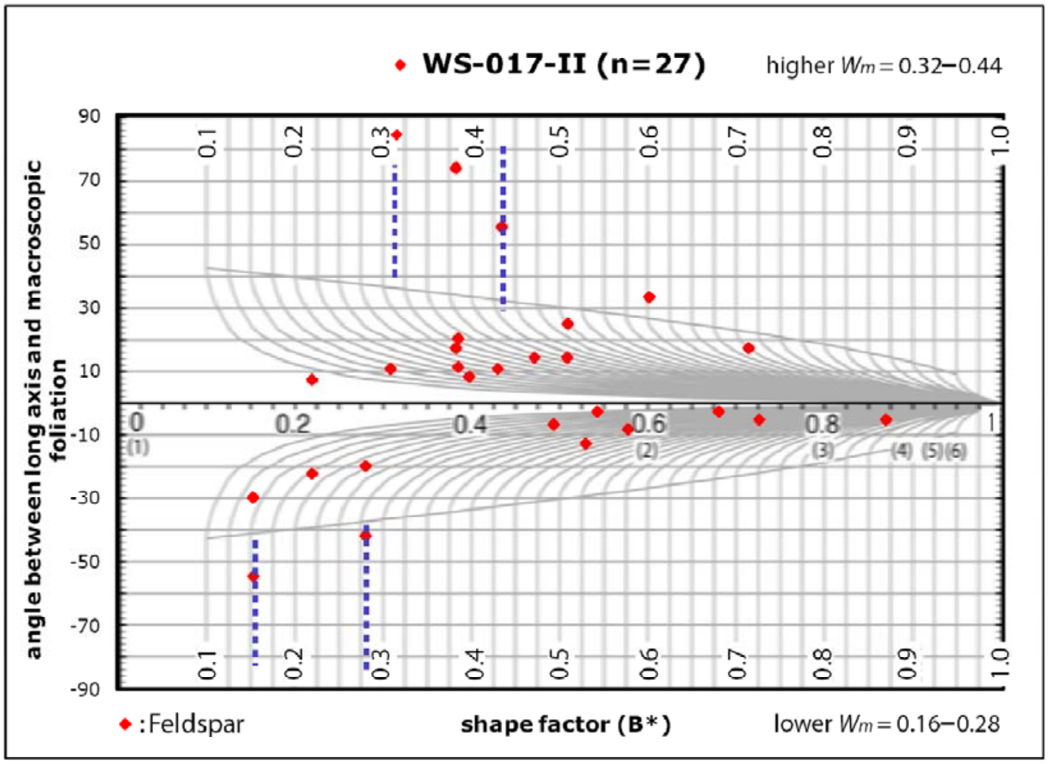

pure

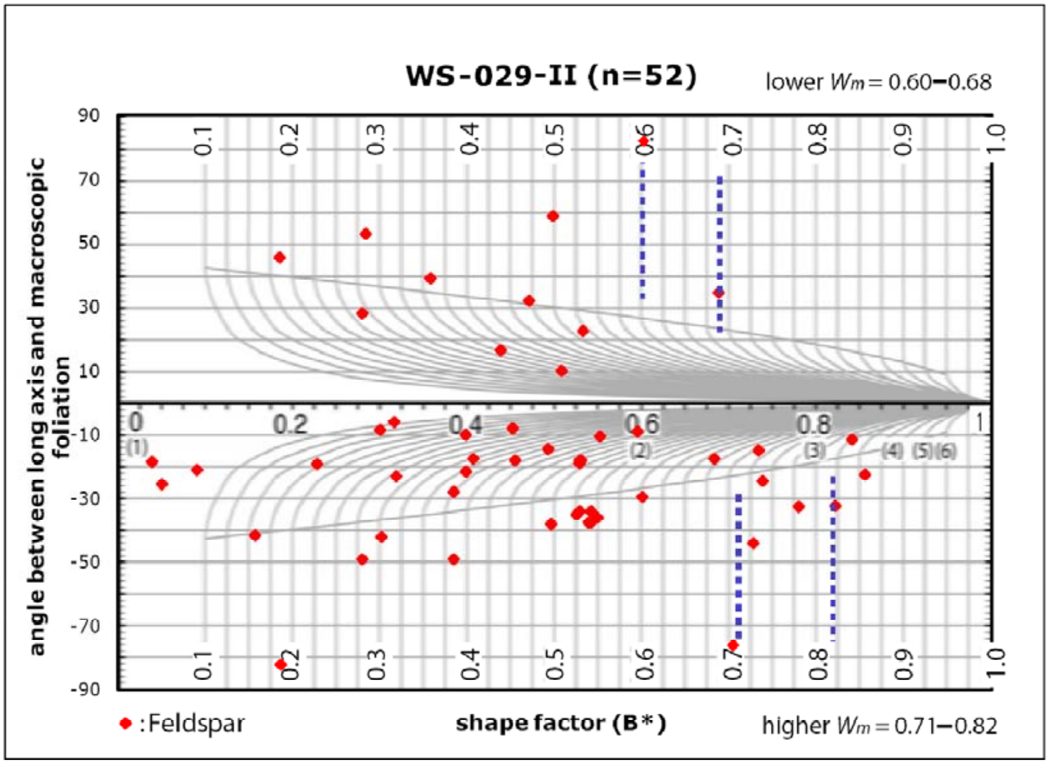

sub-simple to simple

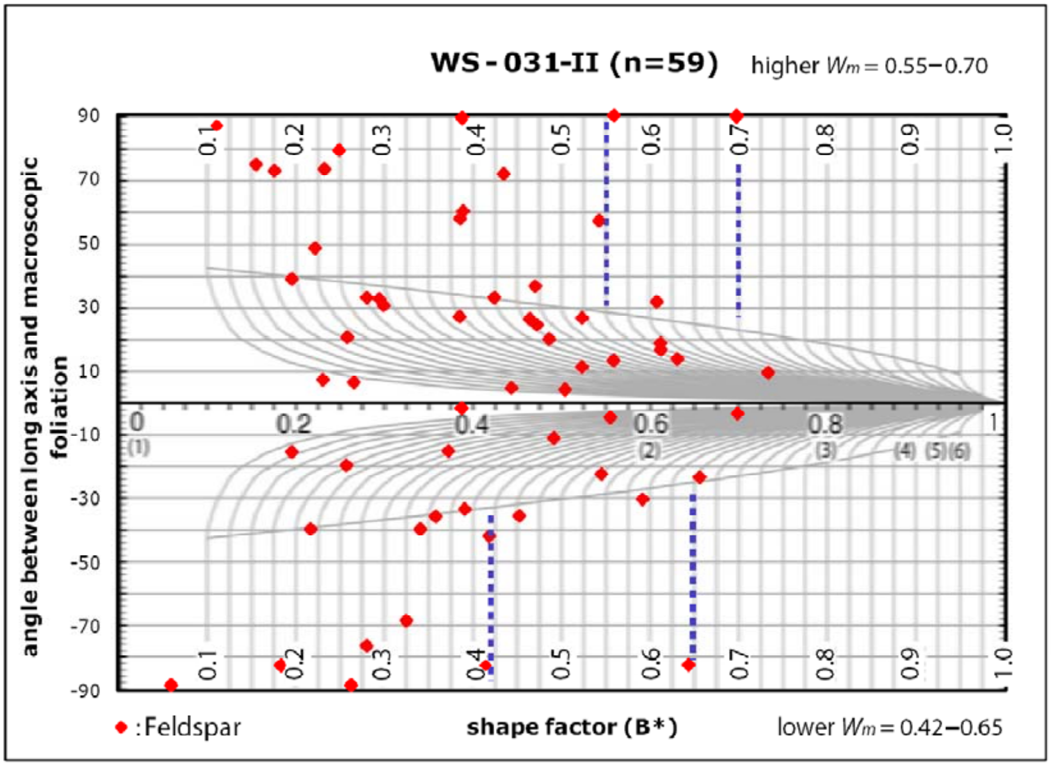

pure to sub-simple

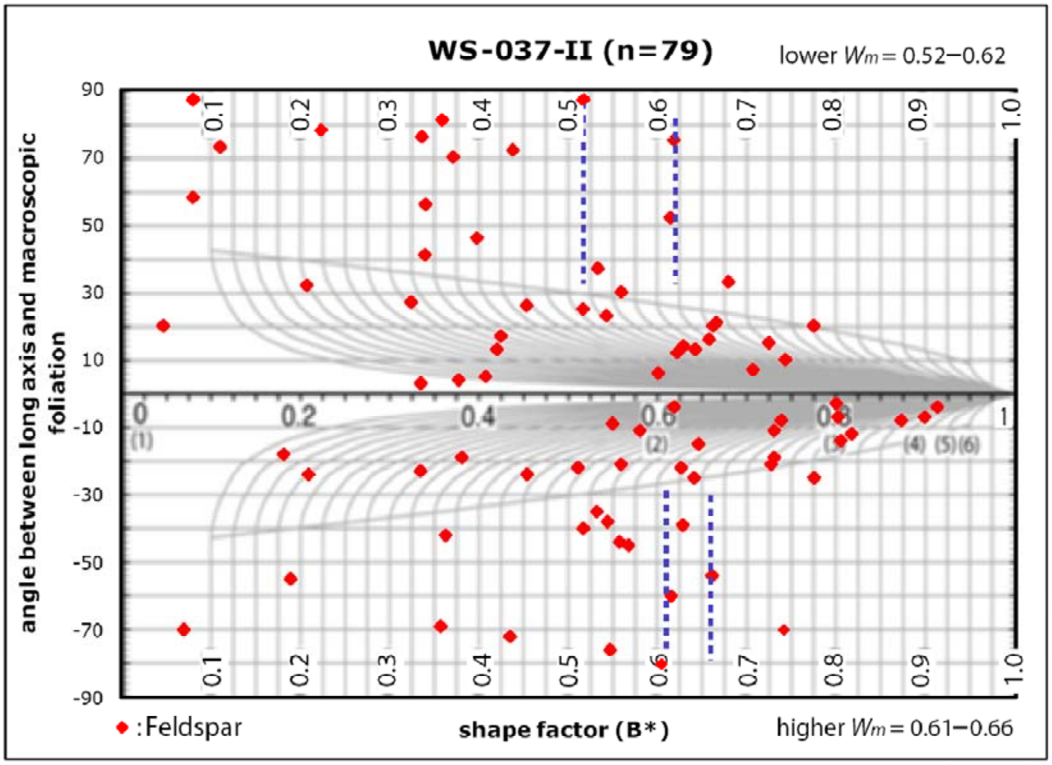

sub-simple

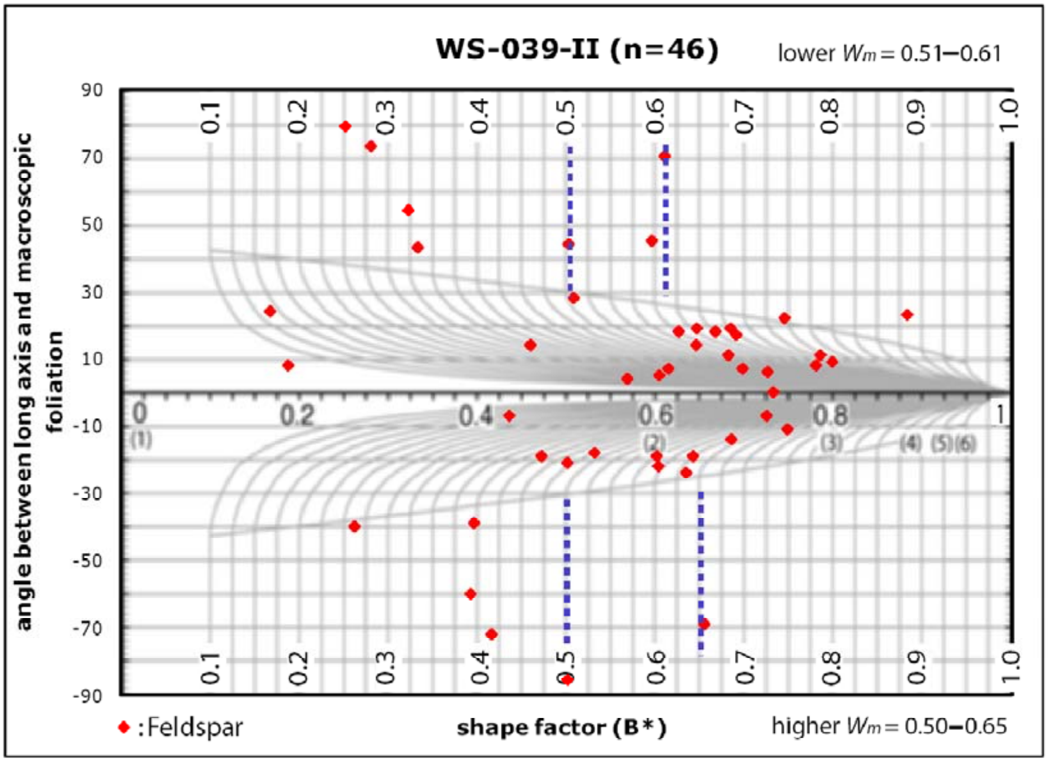

pure to sub-simple

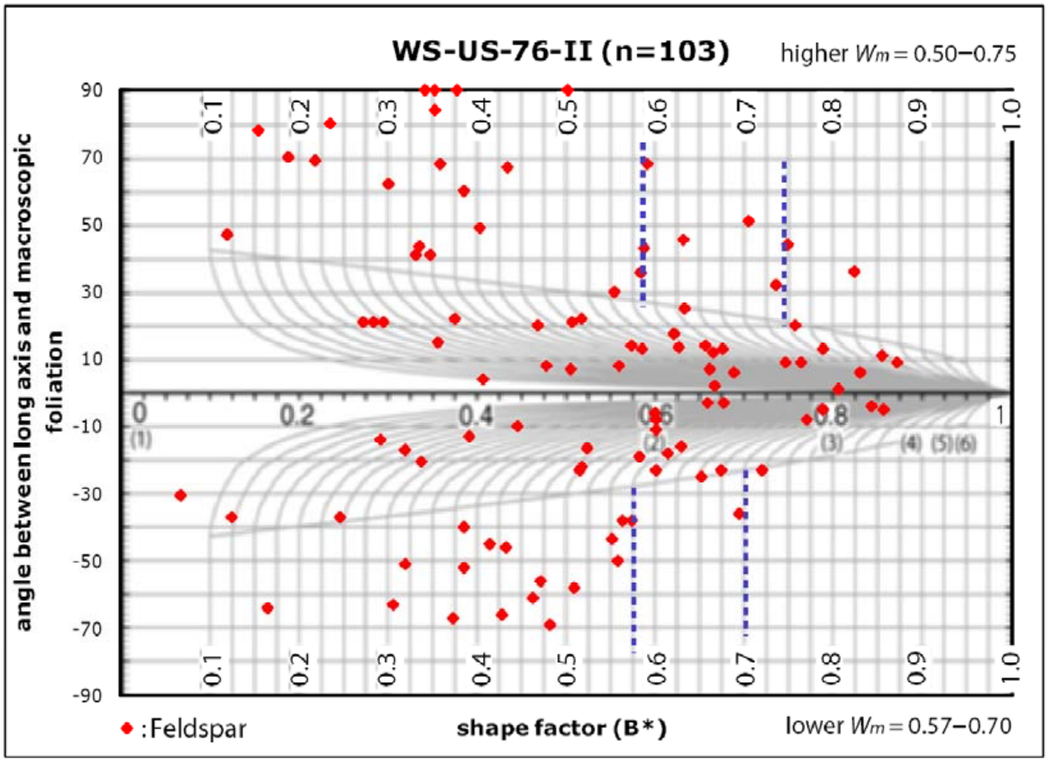

pure to sub-simple

APPENDIX C

Combination of RGN Plots fir XZ- and YZ- section

Blue dots: XZ-section

Red diamond: YZ-section

- TA-033-I and II
- TA-034-I and II
- WS-027-I and II
- WS-022-I and II
- WS-017-I and II
- WS-029-I and II
- WS-031-I and II
- WS-037-I and II
- WS-039-I and II
- WS-US-76-I and II

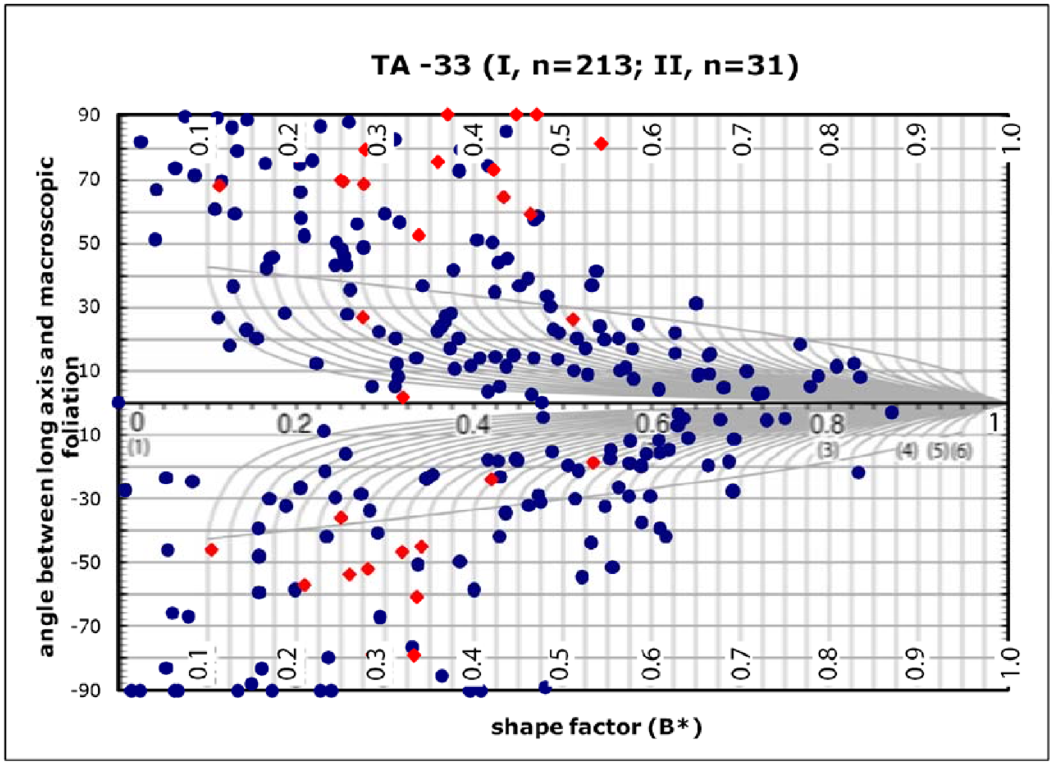
TA -33 (I, n=213; II, n=31)
angle between long axis and macroscopic foliation
shape factor (B*)
90
70
50
30
10
-10
-30
-50
-70
-90
0.1
0.2
0.3
0.4
0.5
0.6
0.7
0.8
0.9
1.0
0
0.2
0.4
0.6
0.8
1
(1)
(3)
(4) (5) (6)

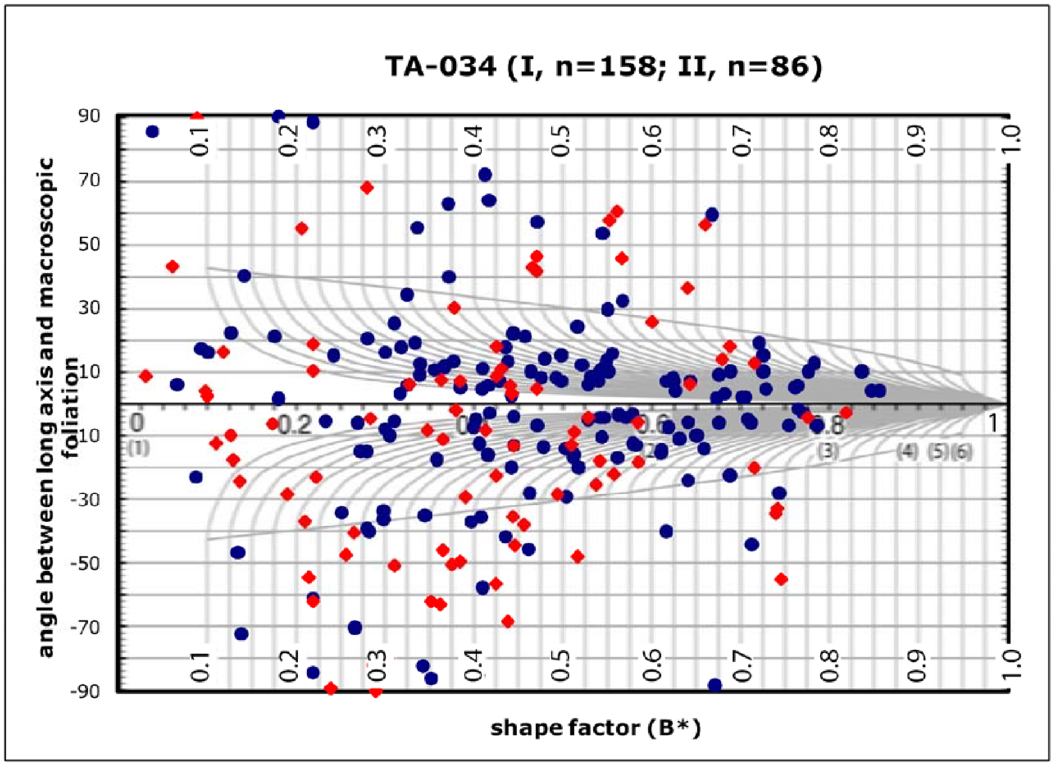
TA-034 (I, n=158; II, n=86)
angle between long axis and macroscopic foliation
shape factor (B*)
90
70
50
30
10
-10
-30
-50
-70
-90
0.1
0.2
0.3
0.4
0.5
0.6
0.7
0.8
0.9
1.0
0
0.2
0.8
1
(1)
(3)
(4) (5) (6)

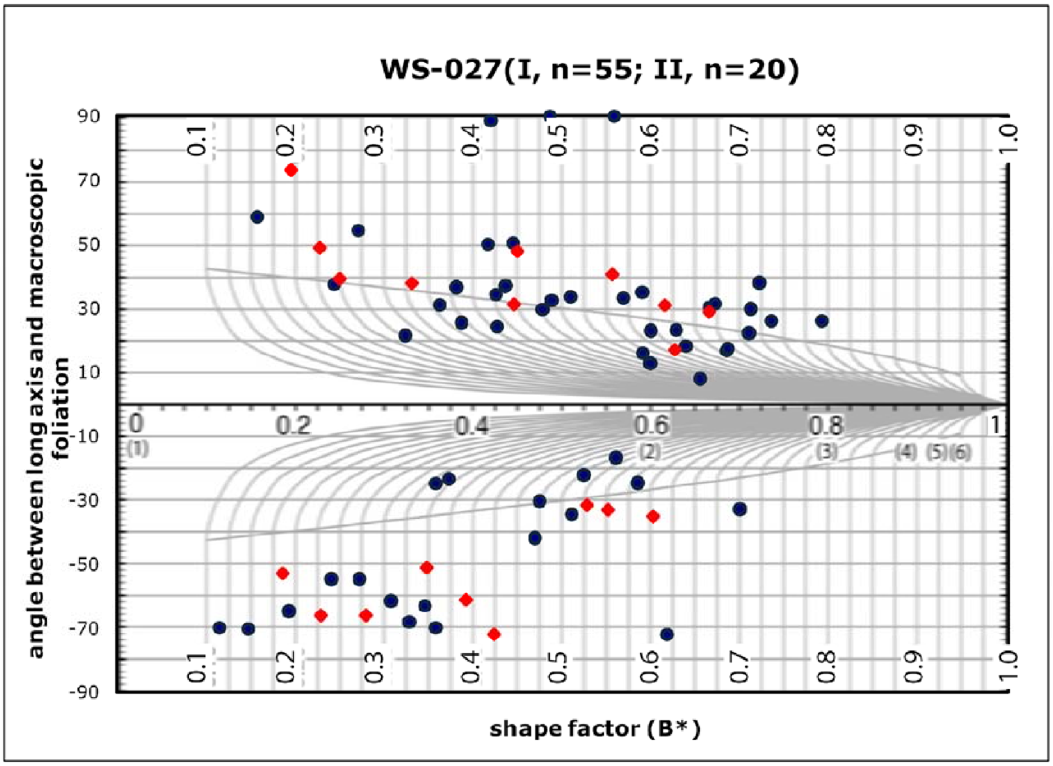
WS-027(I, n=55; II, n=20)
angle between long axis and macroscopic foliation
shape factor (B*)
90
70
50
30
10
-10
-30
-50
-70
-90
0.1
0.2
0.3
0.4
0.5
0.6
0.7
0.8
0.9
1.0
0
0.2
0.4
0.6
0.8
1
(1)
(2)
(3)
(4) (5) (6)

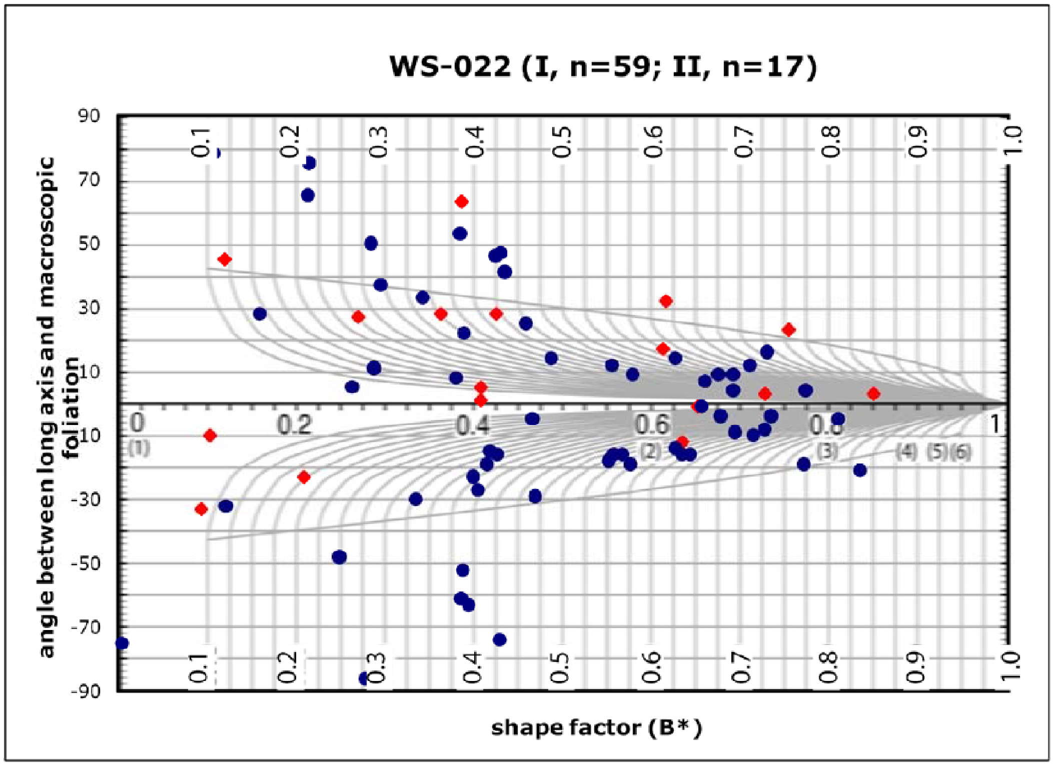
WS-022 (I, n=59; II, n=17)
angle between long axis and macroscopic foliation
shape factor (B*)
90
70
50
30
10
-10
-30
-50
-70
-90
0.1
0.2
0.3
0.4
0.5
0.6
0.7
0.8
0.9
1.0
0
0.2
0.4
0.6
0.8
1
(1)
(2)
(3)
(4) (5) (6)

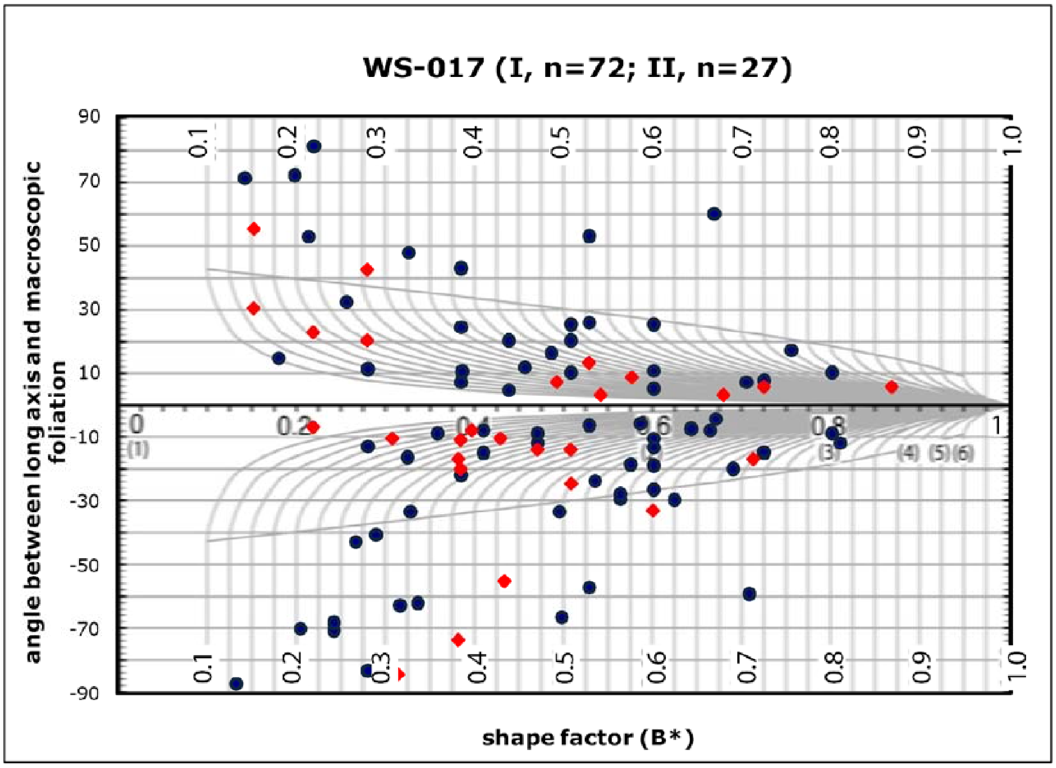
WS-017 (I, n=72; II, n=27)
angle between long axis and macroscopic foliation
shape factor (B*)
90
70
50
30
10
-10
-30
-50
-70
-90
0.1
0.2
0.3
0.4
0.5
0.6
0.7
0.8
0.9
1.0
0
0.2
0.4
0.6
0.8
1
(1)
(2)
(3)
(4)
(5)
(6)

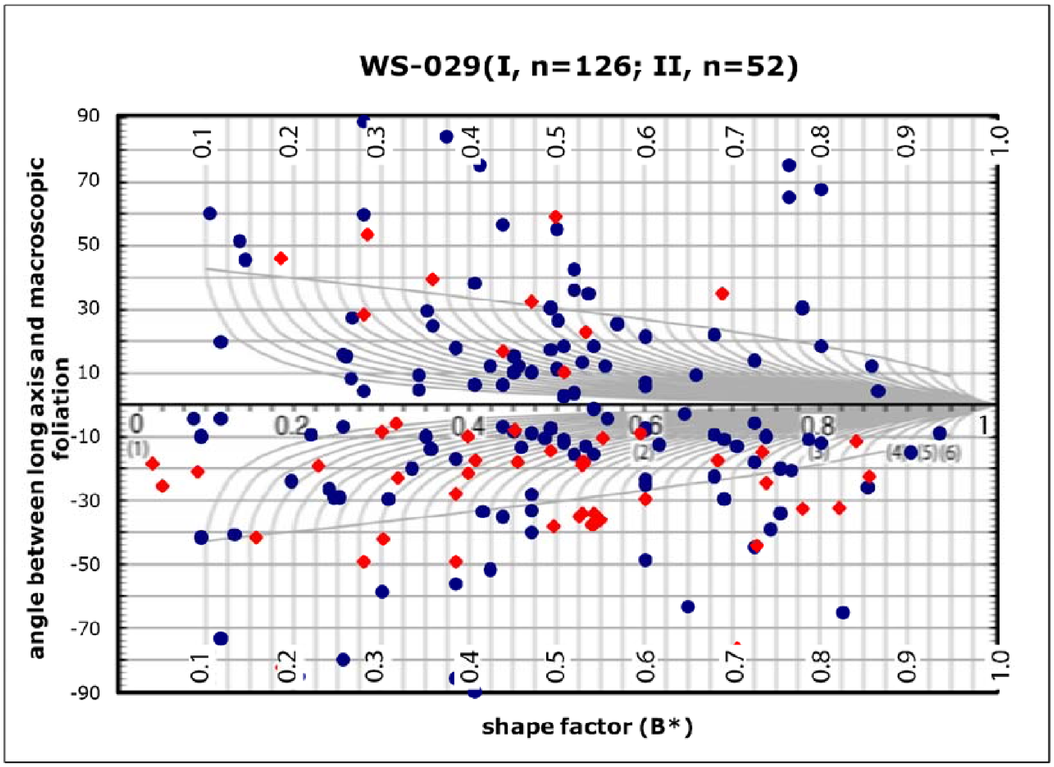
WS-029(I, n=126; II, n=52)
angle between long axis and macroscopic foliation
shape factor (B*)
90
70
50
30
10
-10
-30
-50
-70
-90
0.1
0.2
0.3
0.4
0.5
0.6
0.7
0.8
0.9
1.0
0
0.2
0.4
0.6
0.8
1
(1)
(2)
(3)
(4)
(5)
(6)

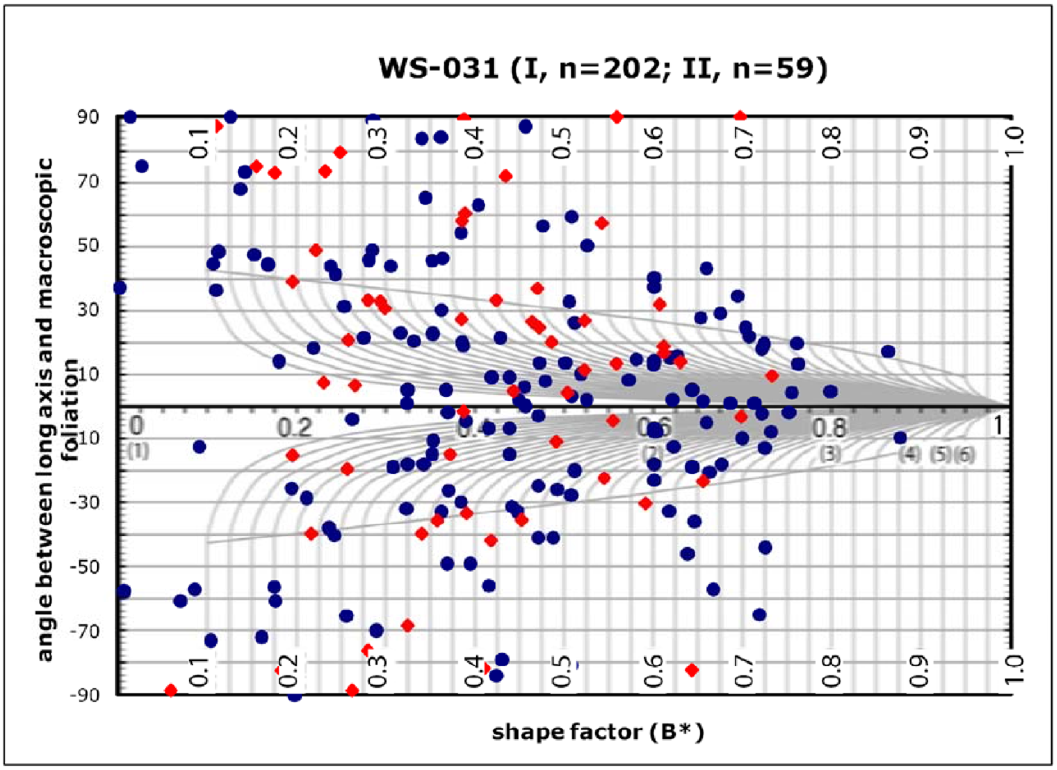
WS-031 (I, n=202; II, n=59)
angle between long axis and macroscopic foliation
shape factor (B*)
90
70
50
30
10
-10
-30
-50
-70
-90
0.1 0.2 0.3 0.4 0.5 0.6 0.7 0.8 0.9 1.0
0 0.2 0.4 0.6 0.8 1
(1) (2) (3) (4) (5) (6)

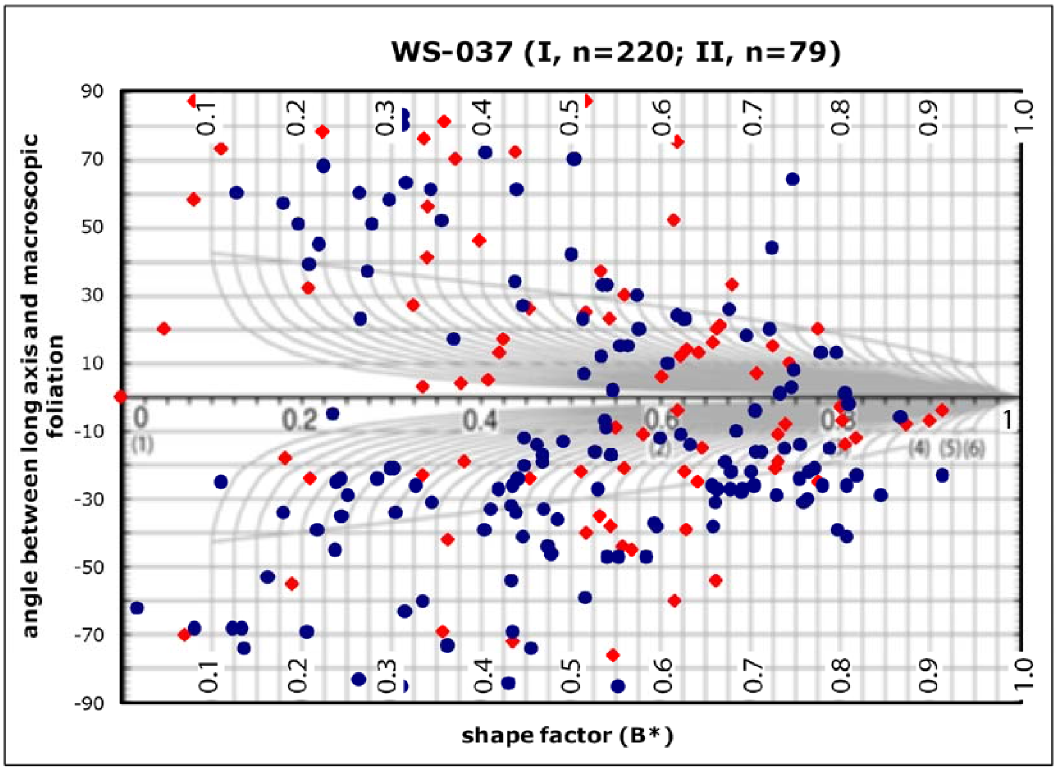
WS-037 (I, n=220; II, n=79)
angle between long axis and macroscopic foliation
shape factor (B*)
90
70
50
30
10
-10
-30
-50
-70
-90
0.1 0.2 0.3 0.4 0.5 0.6 0.7 0.8 0.9 1.0
0 0.2 0.4 0.6 0.8 1
(1) (2) (3) (4) (5) (6)

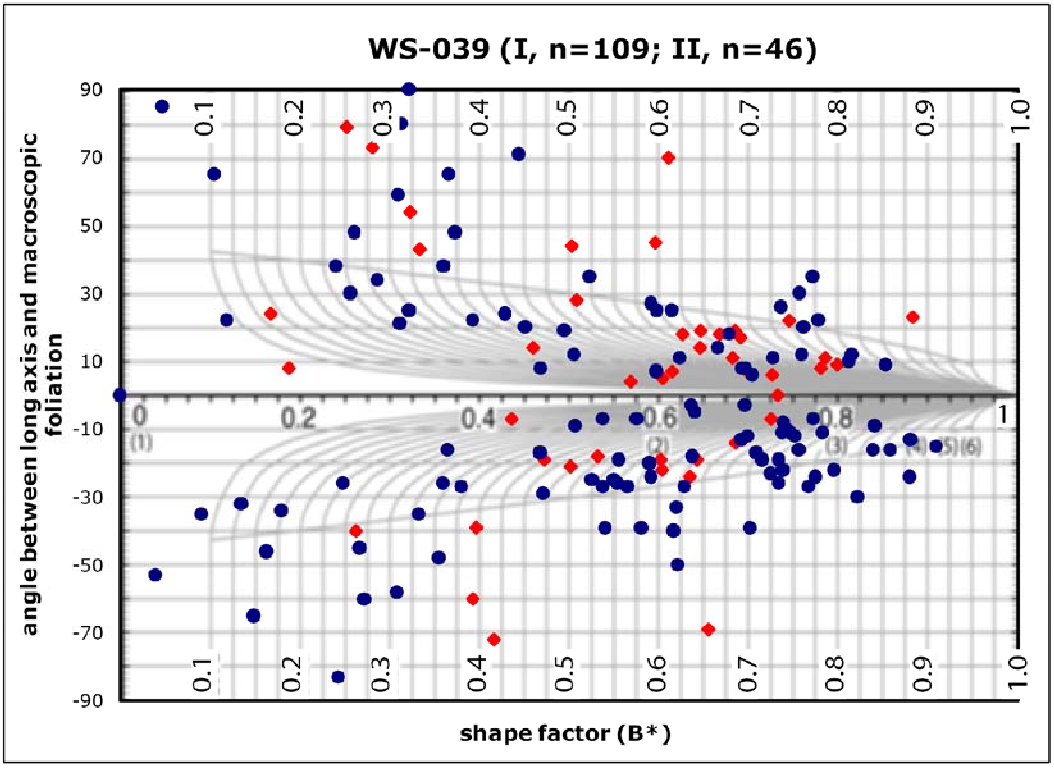
WS-039 (I, n=109; II, n=46)
angle between long axis and macroscopic foliation
shape factor (B*)
90
70
50
30
10
-10
-30
-50
-70
-90
0.1
0.2
0.3
0.4
0.5
0.6
0.7
0.8
0.9
1.0
0
(1)
(2)
(3)
(4)
(5)
(6)
1

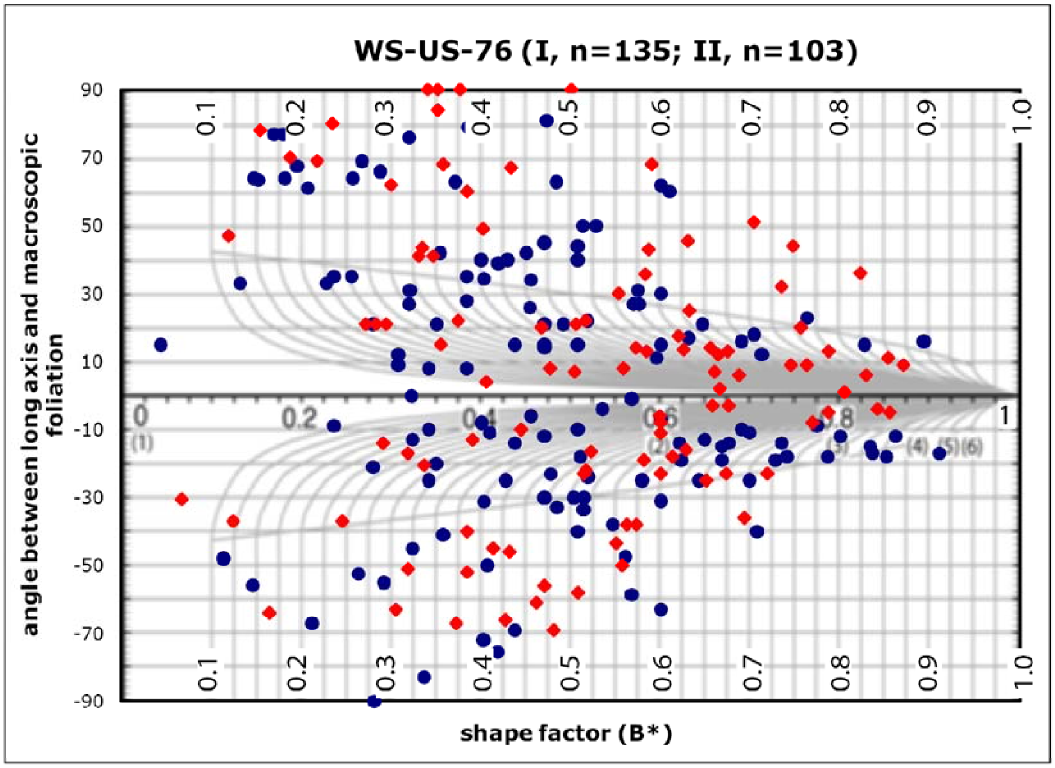
WS-US-76 (I, n=135; II, n=103)
angle between long axis and macroscopic foliation
shape factor (B*)
90
70
50
30
10
-10
-30
-50
-70
-90
0.1
0.2
0.3
0.4
0.5
0.6
0.7
0.8
0.9
1.0
0
(1)
(2)
(3)
(4)
(5)
(6)
1

APPENDIX D

Measurements of Quartz c-axes (Trend and Plunge)

- WS-024-I (1st quartz lenses/ribbon)
- WS-024-I (2nd groundmass)
- WS-020-I
- WS-022-I
- WS-037-I

Universal Stage Data Conversion-1st

Sample ID: WS-024-I

U-Stage Zero Position: 90°

	Universal Stage Measurement			Quartz C-axis	
	Trend	Plunge	Arc	Trend	Plunge
1	285	21	2	165	21
2	345	25	2	105	25
3	348	50	1	282	50
4	333	50	1	297	50
5	337	25	2	113	25
6	396	52	2	54	52
7	403	25	1	227	25
8	337	30	2	113	30
9	332	34	2	118	34
10	344	17	2	106	17
11	333	11	1	297	11
12	307	53	2	143	53
13	287	72	2	163	72
14	610	54	1	20	54
15	330	30	2	120	30
16	329	18	2	121	18
17	337	20	2	113	20
18	337	59	1	293	59
19	334	15	2	116	15
20	338	14	1	292	14
21	180	58	2	270	58
22	336	23	2	114	23
23	338	46	2	112	46
24	338	13	1	292	13
25	339	57	2	111	57
26	545	62	1	85	62
27	341	8	2	109	8
28	351	31	2	99	31
29	345	16	2	105	16
30	387	55	2	63	55
31	358	14	2	92	14
32	334	6	2	116	6
33	334	4	1	296	4
34	433	58	1	197	58
35	303	50	1	327	50
36	338	15	2	112	15
37	367	18	1	263	18
38	349	20	2	101	20
39	335	80	2	115	80
40	380	45	2	70	45
41	379	32	2	71	32
42	351	61	1	279	61
43	343	17	2	107	17
44	328	7	1	302	7
45	558	67	1	72	67
46	329	1	1	301	1
47	331	11	1	299	11
48	564	66	1	66	66
49	280	1	2	170	1
50	340	70	1	290	70
51	330	31	1	300	31
52	356	1	1	274	1

Universal Stage Data Conversion-1st

Sample ID: WS-024-I

U-Stage Zero Position: 90°

	Universal Stage Measurement			Quartz C-axis	
	Trend	Plunge	Arc	Trend	Plunge
53	344	67	1	286	67
54	345	77	2	105	77
55	333	66	1	297	66
56	508	89	1	122	89
57	351	50	1	279	50
58	336	10	1	294	10
59	333	13	1	297	13
60	343	15	2	107	15
61	358	17	2	92	17
62	432	60	1	198	60
63	334	28	1	296	28
64	328	23	2	122	23
65	337	25	2	113	25
66	134	57	2	316	57
67	281	18	1	349	18
68	336	26	2	114	26
69	524	66	1	106	66
70	284	21	2	166	21
71	342	58	1	288	58
72	280	12	1	350	12
73	342	25	2	108	25
74	323	1	1	307	1
75	377	15	1	253	15
76	408	14	1	222	14
77	427	50	1	203	50
78	319	30	1	311	30
79	360	8	1	270	8
80	427	25	1	203	25
81	326	19	2	124	19
82	333	15	2	117	15
83	347	18	1	283	18
84	313	67	2	137	67
85	367	33	1	263	33
86	381	77	1	249	77
87	347	19	2	103	19
88	332	22	2	118	22
89	432	75	1	198	75
90	322	27	2	128	27
91	295	77	2	155	77
92	337	47	2	113	47
93	348	48	2	102	48
94	335	8	1	295	8
95	332	12	1	298	12
96	338	70	2	112	70
97	314	70	2	136	70
98	341	14	2	109	14
99	291	23	2	159	23
100	612	63	1	18	63
101	328	24	2	122	24
102	367	75	2	83	75
103	318	10	2	132	10
104	355	28	2	95	28

Universal Stage Data Conversion-1st

Sample ID: WS-024-I

U-Stage Zero Position: 90°

	Universal Stage Measurement			Quartz C-axis	
	Trend	Plunge	Arc	Trend	Plunge
105	313	23	2	137	23
106	323	17	2	127	17
107	321	18	2	129	18
108	292	69	2	158	69
109	281	23	2	169	23
110	333	22	2	117	22
111	326	29	2	124	29
112	339	15	2	111	15
113	345	24	2	105	24
114	128	75	2	322	75
115	167	73	2	283	73
116	334	13	2	116	13
117	359	29	2	91	29
118	326	9	1	304	9
119	316	27	1	314	27
120	322	27	2	128	27
121	343	13	1	287	13
122	314	76	1	316	76
123	340	32	1	290	32
124	328	22	2	122	22
125	335	32	1	295	32
126	408	56	2	42	56
127	319	12	2	131	12
128	168	34	2	282	34
129	403	23	2	47	23
130	332	35	2	118	35
131	319	19	2	131	19
132	332	14	2	118	14
133	316	23	2	134	23
134	329	82	1	301	82
135	629	22	1	1	22
136	333	26	2	117	26
137	327	33	2	123	33
138	288	62	1	342	62
139	320	78	1	310	78
140	331	24	1	299	24
141	375	77	1	255	77
142	296	16	2	154	16
143	295	81	1	335	81
144	332	18	2	118	18
145	308	12	2	142	12
146	442	55	2	8	55
147	312	28	2	138	28
148	314	21	2	136	21
149	372	50	1	258	50
150	307	51	1	323	51
151	302	73	2	148	73
152	318	12	2	132	12
153	418	58	2	32	58
154	317	17	2	133	17
155	326	13	2	124	13
156	317	11	2	133	11

Universal Stage Data Conversion-1st

Sample ID: WS-024-I

U-Stage Zero Position: 90°

	Universal Stage Measurement			Quartz C-axis	
	Trend	Plunge	Arc	Trend	Plunge
157	353	14	2	97	14
158	343	44	1	287	44
159	322	63	1	308	63
160	332	35	1	298	35
161	333	19	1	297	19
162	331	76	2	119	76
163	329	66	2	121	66
164	373	67	2	77	67
165	336	56	1	294	56
166	372	18	1	258	18
167	267	16	1	3	16
168	314	61	1	316	61
169	325	67	2	125	67
170	321	71	2	129	71
171	317	57	1	313	57
172	350	68	2	100	68
173	324	14	1	306	14
174	325	15	1	305	15
175	327	12	1	303	12
176	383	19	1	247	19
177	237	53	2	213	53
178	290	20	2	160	20
179	416	74	2	34	74
180	318	27	1	312	27
181	318	28	1	312	28
182	320	19	2	130	19
183	414	52	1	216	52
184	415	51	1	215	51
185	319	21	2	131	21
186	317	24	2	133	24
187	426	53	2	24	53
188	318	18	2	132	18
189	408	56	2	42	56
190	425	50	1	205	50
191	522	73	1	108	73
192	514	78	1	116	78
193	243	52	1	27	52
194	317	18	2	133	18
195	318	12	2	132	12
196	452	28	1	178	28
197	318	18	2	132	18
198	315	16	2	135	16
199	270	32	2	180	32
200	434	48	1	196	48
201	323	19	2	127	19
202	192	75	1	78	75
203	304	13	2	146	13
204	308	20	1	322	20
205	324	18	1	306	18
206	430	83	1	200	83
207	320	13	2	130	13
208	307	22	2	143	22

Universal Stage Data Conversion-1st

Sample ID: WS-024-I

U-Stage Zero Position: 90°

	Universal Stage Measurement			Quartz C-axis	
	Trend	Plunge	Arc	Trend	Plunge
209	298	16	2	152	16
210	112	30	2	338	30
211	325	19	1	305	19
212	361	25	1	269	25
213	326	14	1	304	14
214	316	27	2	134	27
215	325	17	2	125	17
216	418	60	2	32	60
217	431	76	1	199	76
218	325	18	2	125	18
219	300	42	1	330	42
220	313	12	2	137	12
221	448	65	2	2	65
222	318	31	2	132	31
223	301	11	1	329	11
224	282	27	1	348	27
225	281	50	2	169	50
226	324	16	1	306	16
227	343	30	2	107	30
228	327	19	2	123	19
229	301	20	1	329	20
230	302	51	1	328	51
231	467	23	1	163	23
232	297	70	2	153	70
233	372	72	2	78	72
234	401	59	1	229	59
235	342	7	2	108	7
236	627	62	1	3	62
237	94	9	2	356	9
238	309	61	1	321	61
239	304	23	1	326	23
240	134	86	2	316	86
241	320	68	2	130	68
242	310	22	2	140	22
243	384	76	1	246	76
244	307	70	2	143	70
245	280	72	2	170	72
246	286	67	1	344	67
247	313	71	1	317	71
248	319	70	1	311	70
249	348	76	1	282	76
250	318	18	1	312	18
251	321	15	1	309	15
252	313	19	1	317	19
253	315	18	1	315	18
254	300	70	2	150	70
255	339	8	1	291	8
256	357	10	2	93	10
257	599	71	1	31	71
258	427	76	2	23	76
259	320	24	2	130	24
260	323	33	2	127	33

Universal Stage Data Conversion-1st

Sample ID: WS-024-I

U-Stage Zero Position: 90°

	Universal Stage Measurement			Quartz C-axis	
	Trend	Plunge	Arc	Trend	Plunge
261	407	22	1	223	22
262	311	18	1	319	18
263	335	23	1	295	23
264	268	52	2	182	52
265	450	76	1	180	76
266	330	25	1	300	25
267	323	18	2	127	18
268	438	22	1	192	22
269	328	1	2	122	1
270	374	55	1	256	55
271	320	56	1	310	56
272	426	61	1	204	61
273	318	18	2	132	18
274	330	61	1	300	61
275	338	18	1	292	18
276	418	60	1	212	60
277	333	17	1	297	17
278	352	77	1	278	77
279	289	74	1	341	74
280	403	20	1	227	20
281	333	18	1	297	18
282	301	27	2	149	27
283	499	75	1	131	75
284	248	1	2	202	1
285	302	68	2	148	68
286	264	80	2	186	80
287	397	17	1	233	17
288	298	21	2	152	21
289	276	63	2	174	63
290	375	16	1	255	16
291	367	27	2	83	27
292	331	58	1	299	58
293	328	22	2	122	22
294	327	17	1	303	17
295	324.5	18.5	1	305.5	18.5
296	314	18.5	1	316	18.5
297	316	16.5	1	314	16.5
298	408	34	2	42	34
299	475	73	1	155	73
300	337	9.5	1	293	9.5
301	324	18	1	306	18
302	324	25.5	2	126	25.5
303	376.5	71.5	1	253.5	71.5
304	234	85	2	216	85
305	314	56	2	136	56
306	380	75	2	70	75
307	333	22	1	297	22
308	306	74	1	324	74
309	313	21	1	317	21
310	331	20	2	119	20
311	331	13	2	119	13
312	326	9.5	1	304	9.5

Universal Stage Data Conversion-1st

	Sample ID:	WS-024-I		U-Stage Zero Position:		90°
	Universal Stage Measurement			Quartz C-axis		
	Trend	Plunge	Arc	Trend	Plunge	
313	327	26	2	123	26	
314	297	68	2	153	68	
315	314	73	1	316	73	
316	313	17	2	137	17	
317	326	62	1	304	62	
318	312	15.5	1	318	15.5	
319	306	20	2	144	20	
320	429	21	1	201	21	
321	308	15	1	322	15	
322	285	55	2	165	55	
323	325	16	2	125	16	
324	316	52	2	134	52	
325	313	14	1	317	14	
326	326.5	21.5	2	123.5	21.5	
327	111	89	2	339	89	
328	312	13	2	138	13	

Universal Stage Data Conversion-2nd

Sample ID: WS-024-I

U-Stage Zero Position:

	Universal Stage Measurement			Quartz C-axis	
	Trend	Plunge	Arc	Trend	Plunge
1	326	83	1	304	83
2	66	8	2	24	8
3	320.5	10	2	129.5	10
4	48	12	1	222	12
5	306.5	78	1	323.5	78
6	23	13	2	67	13
7	341.5	11.5	1	288.5	11.5
8	28	10	1	242	10
9	34	11.5	2	56	11.5
10	355	65	2	95	65
11	298.5	21	2	151.5	21
12	25	12	1	245	12
13	309.5	14	2	140.5	14
14	313	77	2	137	77
15	2	16	1	268	16
16	19	24	1	251	24
17	27	19	2	63	19
18	317	74.5	1	313	74.5
19	49	83	1	221	83
20	6.5	28	1	263.5	28
21	331	8	2	119	8
22	17.5	20	2	72.5	20
23	314.5	77	1	315.5	77
24	33.5	26.5	1	236.5	26.5
25	306.5	65	2	143.5	65
26	75.5	36	2	14.5	36
27	25.5	25	1	244.5	25
28	27	18	2	63	18
29	330.5	78	1	299.5	78
30	355	69.5	2	95	69.5
31	3	4.5	1	267	4.5
32	63	80	2	27	80
33	288.5	71.5	2	161.5	71.5
34	311	32	1	319	32
35	307.5	70	2	142.5	70
36	46	35	1	224	35
37	42	37	2	48	37
38	58.5	75	2	31.5	75
39	61	74.5	2	29	74.5
40	312.5	70	1	317.5	70
41	310	67.5	1	320	67.5
42	328.5	15	1	301.5	15
43	33	13	1	237	13
44	52	24	1	218	24
45	360	7	1	270	7
46	316.5	76.5	1	313.5	76.5
47	356.5	28	2	93.5	28
48	33.5	12.5	1	236.5	12.5
49	296.5	73	1	333.5	73
50	325.5	71.5	2	124.5	71.5
51	328.5	68.5	1	301.5	68.5
52	86.5	21	1	183.5	21

Universal Stage Data Conversion-2nd

	Sample ID:	WS-024-I		U-Stage Zero Position:	
	Universal Stage Measurement			Quartz C-axis	
	Trend	Plunge	Arc	Trend	Plunge
53	271	77	1	359	77
54	277.5	74	1	352.5	74
55	323.5	71.5	2	126.5	71.5
56	327	64	2	123	64
57	68	8	2	22	8
58	317.5	67	2	132.5	67
59	315	65	2	135	65
60	309	11	1	321	11
61	297.5	63.5	2	152.5	63.5
62	5.5	9	1	264.5	9
63	301	3	1	329	3
64	311	75.5	1	319	75.5
65	318	12	2	132	12
66	284.5	15.5	1	345.5	15.5
67	334.5	75	2	115.5	75
68	334.5	72	1	295.5	72
69	336.5	13.5	1	293.5	13.5
70	337	76	2	113	76
71	68	9	2	22	9
72	44	9	1	226	9
73	352	23	2	98	23
74	310	17	1	320	17
75	73	17	1	197	17
76	338.5	76.5	2	111.5	76.5
77	343.5	72	2	106.5	72
78	328	25	1	302	25
79	30	13	2	60	13
80	332	18	2	118	18
81	39.5	28	2	50.5	28
82	313	67	2	137	67
83	303	76	1	327	76
84	316	71	2	134	71
85	298	8	1	332	8
86	61.5	27.5	2	28.5	27.5
87	35	15	1	235	15
88	34	11	1	236	11
89	290.5	62	2	159.5	62
90	359	25	2	91	25
91	63	72.5	2	27	72.5
92	309.5	26.5	1	320.5	26.5
93	68	11.5	2	22	11.5
94	78.5	82	1	191.5	82
95	318	39	1	312	39
96	307.5	67.5	2	142.5	67.5
97	27	24	2	63	24
98	321.5	14.5	2	128.5	14.5
99	315	13.5	1	315	13.5
100	320	68	1	310	68
101	298	72	1	332	72
102	292	82.5	1	338	82.5
103	42	27.5	1	228	27.5
104	12.5	49.5	2	77.5	49.5

Universal Stage Data Conversion-2nd

Sample ID: WS-024-I

U-Stage Zero Position:

	Universal Stage Measurement			Quartz C-axis	
	Trend	Plunge	Arc	Trend	Plunge
105	291	65	2	159	65
106	60.5	77	1	209.5	77
107	59	14	1	211	14
108	67.5	3.5	1	202.5	3.5
109	312	7	1	318	7
110	275	30	1	355	30
111	75	33	2	15	33
112	52	15	1	218	15
113	282	67.5	1	348	67.5
114	4.5	74	2	85.5	74
115	53.5	5.5	2	36.5	5.5
116	332	21	2	118	21
117	62	10	2	28	10
118	63	72	2	27	72
119	277	76	1	353	76
120	317	78	1	313	78
121	75	7	1	195	7
122	332	53	1	298	53
123	45.5	14	2	44.5	14
124	317.5	65	2	132.5	65
125	67	78	2	23	78
126	320.5	70	2	129.5	70
127	8	15	1	262	15
128	297	72	2	153	72
129	309.5	58	1	320.5	58
130	313	69	2	137	69
131	35	23.5	2	55	23.5
132	60	7	2	30	7
133	40	26	1	230	26
134	86.5	38	1	183.5	38
135	50	60	2	40	60
136	56	12	1	214	12
137	56	64	1	214	64
138	28.5	18	2	61.5	18
139	56.5	48	1	213.5	48
140	342	16.5	1	288	16.5
141	42.5	21	1	227.5	21
142	39	13	2	51	13
143	39	4.5	1	231	4.5
144	70.5	25	1	199.5	25
145	23	24	1	247	24
146	18	24	1	252	24
147	29	24	1	241	24
148	57	25	1	213	25
149	34	9	2	56	9
150	283.5	57	1	346.5	57
151	284	70	2	166	70
152	69.5	51	2	20.5	51
153	60	29	2	30	29
154	40.5	23	2	49.5	23
155	67.5	72.5	2	22.5	72.5
156	30.5	18	1	239.5	18

Universal Stage Data Conversion-2nd

	Sample ID: WS-024-I			U-Stage Zero Position:	
	Universal Stage Measurement			Quartz C-axis	
	Trend	Plunge	Arc	Trend	Plunge
157	308	32	1	322	32
158	337	81	1	293	81
159	36	74.5	2	54	74.5
160	73	12.5	2	17	12.5
161	328	64.5	2	122	64.5
162	62.5	73.5	2	27.5	73.5
163	322.5	63	2	127.5	63
164	353.5	25	1	276.5	25
165	296.5	73	2	153.5	73
166	56	82	1	214	82
167	303.5	56.5	1	326.5	56.5
168	336	35	1	294	35
169	57	5.5	2	33	5.5
170	350.5	82	1	279.5	82
171	40	17.5	2	50	17.5
172	57	20	2	33	20
173	295.5	64.5	2	154.5	64.5
174	33	11.5	2	57	11.5
175	340.5	31.5	1	289.5	31.5
176	39	30	1	231	30
177	40	9	2	50	9
178	292	30	2	158	30
179	309	37	2	141	37
180	309.5	12	1	320.5	12
181	43	76.5	2	47	76.5
182	301	20	1	329	20
183	325	7.5	2	125	7.5
184	313	77	1	317	77
185	311.5	77	1	318.5	77
186	348	78	1	282	78
187	326.5	79	2	123.5	79
188	300	67	2	150	67
189	286	75	1	344	75
190	278	40	2	172	40

Universal Stage Data Conversion

Sample ID: WS-020-I

U-Stage Zero Position: 97°

	Universal Stage Measurement			Quartz C-axis	
	Trend	Plunge	Arc	Trend	Plunge
1	365	66	2	85	66
2	611	80	1	19	80
3	334	80	2	116	80
4	409	75	2	41	75
5	265	72.5	1	5	72.5
6	144	89	1	126	89
7	99	77.5	2	351	77.5
8	428	10	1	202	10
9	426	12	1	204	12
10	456.5	1	1	173.5	1
11	350	1	1	280	1
12	351	7	1	279	7
13	362	74.5	1	268	74.5
14	347	64	2	103	64
15	381	89	1	249	89
16	382	79	2	68	79
17	387.5	58	2	62.5	58
18	403.5	56	2	46.5	56
19	370.5	64	2	79.5	64
20	366.5	64	2	83.5	64
21	534	70.5	1	96	70.5
22	382	68	2	68	68
23	329	56	2	121	56
24	558.5	64	1	71.5	64
25	373	63.5	2	77	63.5
26	332	79	2	118	79
27	356.5	45	2	93.5	45
28	279	35	2	171	35
29	278	24.5	2	172	24.5
30	348	58	2	102	58
31	335.5	62	2	114.5	62
32	340	46.5	2	110	46.5
33	368	13	1	262	13
34	401	75.5	2	49	75.5
35	335	54	2	115	54
36	341	50	2	109	50
37	370	52	1	260	52
38	347.5	53	2	102.5	53
39	359	75	1	271	75
40	537	30	1	93	30
41	174	72.5	2	276	72.5
42	507.5	48.5	1	122.5	48.5
43	331	53	2	119	53
44	193	74	2	257	74
45	370	62	1	260	62
46	331	47	2	119	47
47	369	75	1	261	75
48	354	70	1	276	70
49	296	62.5	2	154	62.5
50	348	18	2	102	18
51	408	21.5	2	42	21.5
52	620	69	1	10	69

Universal Stage Data Conversion

Sample ID: WS-020-I

U-Stage Zero Position: 97°

	Universal Stage Measurement			Quartz C-axis	
	Trend	Plunge	Arc	Trend	Plunge
53	353	22.5	2	97	22.5
54	356	55	2	94	55
55	389	55	2	61	55
56	339	52	2	111	52
57	394	56	2	56	56
58	384	82	2	66	82
59	369	78	2	81	78
60	423	59.5	2	27	59.5
61	401	75	1	229	75
62	366.5	78	2	83.5	78
63	399.5	64	2	50.5	64
64	355	51	2	95	51
65	369	79.5	2	81	79.5
66	425	79	1	205	79
67	287	6	2	163	6
68	295	17	2	155	17
69	363	17.5	2	87	17.5
70	326	15	2	124	15
71	292	1	2	158	1
72	411	52	2	39	52
73	322	29	2	128	29
74	374	18.5	1	256	18.5
75	411	24	2	39	24
76	367	18	2	83	18
77	493	64	1	137	64
78	387	15	1	243	15
79	374	77	2	76	77
80	233	64	2	217	64
81	117	62	2	333	62
82	126.5	69	2	323.5	69
83	371	50	1	259	50
84	405	72	2	45	72
85	367	52	1	263	52
86	373	62	1	257	62
87	369	64	1	261	64
88	435	83	2	15	83
89	425	23	2	25	23
90	335	67	2	115	67
91	433	76	2	17	76
92	341	80	1	289	80
93	321	15	1	309	15
94	287.5	80.5	2	162.5	80.5
95	339.5	73.5	2	110.5	73.5
96	341	16.5	2	109	16.5
97	399	79	1	231	79
98	352.5	78	1	277.5	78
99	419	14.5	1	211	14.5
100	263.5	70	1	6.5	70
101	352	87	1	278	87
102	423	78.5	2	27	78.5
103	413.5	4	2	36.5	4
104	399.5	64	2	50.5	64

Universal Stage Data Conversion

Sample ID: WS-020-I

U-Stage Zero Position: 97°

	Universal Stage Measurement			Quartz C-axis	
	Trend	Plunge	Arc	Trend	Plunge
105	391	12.5	2	59	12.5
106	425	20	1	205	20
107	332	60	2	118	60
108	315	9	2	135	9
109	327	15	2	123	15
110	298	55	1	332	55
111	309	32.5	1	321	32.5
112	309	57	1	321	57
113	307.5	55	1	322.5	55
114	413	81.5	2	37	81.5
115	280	11.5	1	350	11.5
116	282.5	0.5	2	167.5	0.5
117	284	13	1	346	13
118	397	77	1	233	77
119	304	53	1	326	53
120	361	79.5	2	89	79.5
121	383	70	1	247	70
122	397	74	1	233	74
123	287	61	1	343	61
124	264	70	1	6	70
125	282.5	73	1	347.5	73
126	333.5	54	1	296.5	54
127	274.5	78	1	355.5	78
128	275.5	52.5	1	354.5	52.5
129	333.5	15	1	296.5	15
130	333.5	12	2	116.5	12
131	374	28	2	76	28
132	372	86	2	78	86
133	622.5	55	1	7.5	55
134	418.5	53	2	31.5	53
135	373.5	89	2	76.5	89
136	416.5	79	2	33.5	79
137	418	77.5	2	32	77.5
138	418	70	2	32	70
139	441	65	2	9	65
140	419.5	75	2	30.5	75
141	329	22	2	121	22
142	320	20	2	130	20
143	319.5	78.5	1	310.5	78.5
144	305	63	1	325	63
145	280.5	62	1	349.5	62
146	320.5	83.5	1	309.5	83.5
147	290	66.5	1	340	66.5
148	308	65	2	142	65
149	372	53	2	78	53
150	376	52	2	74	52
151	416.5	68.5	2	33.5	68.5
152	371.5	70	2	78.5	70
153	425.5	52.5	2	24.5	52.5
154	426.5	51.5	2	23.5	51.5
155	313.5	75.5	1	316.5	75.5
156	390.5	6	2	59.5	6

Universal Stage Data Conversion

Sample ID: WS-020-I

U-Stage Zero Position: 97^{o}

	Universal Stage Measurement			Quartz C-axis	
	Trend	Plunge	Arc	Trend	Plunge
157	400.5	56.5	2	49.5	56.5
158	378.5	8	2	71.5	8
159	346	64	2	104	64
160	348	85	2	102	85
161	407.5	56	1	222.5	56
162	370	50	2	80	50
163	277	1	1	353	1
164	351	24.5	1	279	24.5
165	353	23.5	1	277	23.5
166	372	6.5	1	258	6.5
167	337	80	1	293	80
168	385	78	2	65	78
169	439.5	68	1	190.5	68
170	239	70	2	211	70
171	319	10.5	2	131	10.5
172	619	74.5	1	11	74.5
173	338.5	62	2	111.5	62
174	300.5	71	1	329.5	71
175	369	70	2	81	70
176	377	68	2	73	68
177	342.5	0.5	1	287.5	0.5
178	336	56	2	114	56
179	269.5	6	2	180.5	6
180	404.5	55	2	45.5	55
181	414	52	2	36	52
182	416	53	2	34	53
183	363	79	1	267	79
184	275	79.5	1	355	79.5
185	269	82.5	1	1	82.5
186	374	75	1	256	75
187	329	69	2	121	69
188	619	50	1	11	50
189	351	60	2	99	60
190	440	18	2	10	18
191	290	63.5	2	160	63.5
192	322	74	2	128	74
193	350	59.5	1	280	59.5
194	398	22.5	2	52	22.5
195	346	56	2	104	56
196	333.5	17.5	2	116.5	17.5
197	312	6	1	318	6
198	315	6	1	315	6
199	299.5	66	1	330.5	66
200	277	15	1	353	15
201	251	68	2	199	68
202	428.5	59	2	21.5	59
203	373.5	79.5	2	76.5	79.5
204	373	77	2	77	77
205	410	6	1	220	6
206	105	12.5	2	345	12.5
207	421	11	1	209	11
208	423.5	23	2	26.5	23

Universal Stage Data Conversion

Sample ID: WS-020-I

U-Stage Zero Position: 97°

	Universal Stage Measurement			Quartz C-axis	
	Trend	Plunge	Arc	Trend	Plunge
209	387	71	2	63	71
210	310	13.5	2	140	13.5
211	603	5.5	1	27	5.5
212	386.5	78	1	243.5	78
213	621	1	1	9	1
214	430	62	1	200	62
215	582	61.5	1	48	61.5
216	408.5	65.5	2	41.5	65.5
217	492	7	1	138	7
218	384.5	58	2	65.5	58
219	296.5	4	2	153.5	4
220	555	40	1	75	40
221	395	84.5	2	55	84.5
222	339	12.5	2	111	12.5
223	264	56.5	1	6	56.5
224	267	9	1	3	9
225	282.5	63	1	347.5	63
226	420.5	50	2	29.5	50
227	357	72.5	2	93	72.5
228	93.5	22	2	356.5	22
229	430.5	85	2	19.5	85
230	346	83	2	104	83
231	318	20	2	132	20
232	299.5	29	1	330.5	29
233	435.5	61	2	14.5	61
234	392	70	2	58	70
235	427.5	64.5	1	202.5	64.5
236	338	76	2	112	76
237	338.5	22.5	2	111.5	22.5
238	332.5	55	2	117.5	55
239	296.5	59	2	153.5	59
240	351	55	2	99	55
241	298	59	2	152	59
242	327.5	82	2	122.5	82
243	331	10	1	299	10
244	410	53.5	2	40	53.5
245	277	84.5	2	173	84.5
246	362	8	1	268	8
247	327.5	50.5	1	302.5	50.5
248	343	68	2	107	68
249	360.5	30	1	269.5	30
250	265	10	1	5	10
251	324	30.5	1	306	30.5
252	305.5	9	1	324.5	9
253	304.5	7	1	325.5	7
254	327	74	2	123	74
255	294.5	18.5	1	335.5	18.5
256	333	32	2	117	32
257	619	49	1	11	49
258	353	56.5	2	97	56.5
259	401.5	84	2	48.5	84
260	310	66	2	140	66

Universal Stage Data Conversion

Sample ID: WS-020-I

U-Stage Zero Position: 97°

	Universal Stage Measurement			Quartz C-axis	
	Trend	Plunge	Arc	Trend	Plunge
261	293.5	32	1	336.5	32
262	292.5	28.5	1	337.5	28.5
263	322	51	2	128	51
264	387	85	2	63	85
265	387	79.5	2	63	79.5
266	278	53.5	1	352	53.5
267	315.5	14.5	1	314.5	14.5
268	373	71	2	77	71
269	126	18	2	324	18
270	300	17	1	330	17
271	93	78	2	357	78
272	345	62	2	105	62
273	339	52.5	2	111	52.5
274	333	52	2	117	52
275	280.5	77	1	349.5	77
276	341	84	2	109	84
277	322	57	2	128	57
278	332	78	2	118	78
279	332	66	2	118	66
280	320	16	2	130	16
281	322.5	56	2	127.5	56
282	280.5	14.5	2	169.5	14.5
283	327.5	13	2	122.5	13
284	350	20	2	100	20
285	333.5	55	2	116.5	55
286	385.5	54.5	2	64.5	54.5
287	311.5	84	2	138.5	84
288	320	77	2	130	77
289	339	1	2	111	1
290	343	69	2	107	69
291	353	6	2	97	6
292	428	77	2	22	77
293	360	82	1	270	82
294	596	25	1	34	25
295	347	13	1	283	13
296	529.5	54	1	100.5	54
297	358	48.5	2	92	48.5
298	374.5	12.5	2	75.5	12.5
299	400	19	2	50	19
300	385	12.5	2	65	12.5
301	554	17.5	1	76	17.5
302	313.5	61	2	136.5	61
303	371	58	2	79	58
304	330	56	2	120	56
305	328.5	52.5	2	121.5	52.5
306	327	55	2	123	55
307	338.5	24.5	2	111.5	24.5
308	450	0.5	1	180	0.5
309	316	14	1	314	14
310	341	10	2	109	10
311	365	83	2	85	83
312	187	35	2	263	35

Universal Stage Data Conversion

Sample ID: WS-020-I

U-Stage Zero Position: 97°

	Universal Stage Measurement			Quartz C-axis	
	Trend	Plunge	Arc	Trend	Plunge
313	563	7	1	67	7
314	355	56	2	95	56
315	350	72	2	100	72
316	606	60	1	24	60
317	303.5	13	2	146.5	13
318	417	1	2	33	1
319	337.5	9.5	1	292.5	9.5
320	338	60	2	112	60
321	320.5	15.5	2	129.5	15.5
322	366	58	2	84	58
323	319	24.5	2	131	24.5
324	316	10	2	134	10
325	327	24	2	123	24
326	357.5	13	1	272.5	13
327	378	78	1	252	78
328	281.5	70	2	168.5	70
329	486	71	1	144	71
330	390	53	2	60	53
331	401	52	2	49	52
332	371.5	67.5	2	78.5	67.5
333	319	63	1	311	63
334	270.5	54.5	1	359.5	54.5
335	301.5	68	2	148.5	68
336	291.5	38	1	338.5	38
337	265.5	82.5	2	184.5	82.5
338	323.5	52	1	306.5	52

Universal Stage Data Conversion

Sample ID: WS-022-I

U-Stage Zero Position: 0°

	Universal Stage Measurement			Quartz C-axis	
	Trend	Plunge	Arc	Trend	Plunge
1	278	34	1	352	34
2	284.5	62.5	1	345.5	62.5
3	69	72.5	2	21	72.5
4	312	30	1	318	30
5	291	66	1	339	66
6	16.5	72	2	73.5	72
7	282	27	1	348	27
8	310	21.5	2	140	21.5
9	313	27.5	2	137	27.5
10	43	65	2	47	65
11	43.5	59	2	46.5	59
12	265.5	67.5	1	4.5	67.5
13	31	79.5	2	59	79.5
14	313.5	12.5	1	316.5	12.5
15	271	77	2	179	77
16	18	16	2	72	16
17	330	27.5	1	300	27.5
18	285	54.5	1	345	54.5
19	285.5	78.5	1	344.5	78.5
20	284.5	72	1	345.5	72
21	64	73	2	26	73
22	342.5	9.5	2	107.5	9.5
23	291	66	1	339	66
24	131	20.5	2	319	20.5
25	263.5	80	1	6.5	80
26	301	76.5	1	329	76.5
27	278	62.5	1	352	62.5
28	295	67	1	335	67
29	302	68.5	1	328	68.5
30	287	64	1	343	64
31	317	42	1	313	42
32	316	42	1	314	42
33	327	31	1	303	31
34	327.5	6	1	302.5	6
35	301.5	47	1	328.5	47
36	27.5	67.5	2	62.5	67.5
37	283.5	51	2	166.5	51
38	283	57.5	1	347	57.5
39	13.5	54.5	1	256.5	54.5
40	52	56.5	2	38	56.5
41	56.5	50.5	2	33.5	50.5
42	53	70	2	37	70
43	280.5	53	1	349.5	53
44	301.5	75	2	148.5	75
45	318.5	79	2	131.5	79
46	319.5	77	2	130.5	77
47	8.5	72.5	2	81.5	72.5
48	8.5	68	2	81.5	68
49	32.5	72.5	2	57.5	72.5
50	333	83	2	117	83
51	281	65	1	349	65
52	27.5	72.5	2	62.5	72.5

Universal Stage Data Conversion

Sample ID: WS-022-I

U-Stage Zero Position: 0°

	Universal Stage Measurement			Quartz C-axis	
	Trend	Plunge	Arc	Trend	Plunge
53	350	45	2	100	45
54	288	52	1	342	52
55	205	68	2	245	68
56	316.5	52.5	1	313.5	52.5
57	300	67	1	330	67
58	309	0.5	1	321	0.5
59	309.5	1	2	140.5	1
60	28.5	56.5	2	61.5	56.5
61	46	81	2	44	81
62	302	65	1	328	65
63	304.5	64	1	325.5	64
64	12	75	2	78	75
65	52	80	2	38	80
66	283	18.5	1	347	18.5
67	320.5	12	1	309.5	12
68	319	12.5	1	311	12.5
69	318	10.5	1	312	10.5
70	347.5	52.5	2	102.5	52.5
71	338	71.5	2	112	71.5
72	272	65	1	358	65
73	323	13	2	127	13
74	324	15	2	126	15
75	326	18	2	124	18
76	326	17	2	124	17
77	303	76	2	147	76
78	282	72	1	348	72
79	76	71.5	2	14	71.5
80	297	52	1	333	52
81	298	55	1	332	55
82	263	66	1	7	66
83	302.5	4.5	2	147.5	4.5
84	293	8	1	337	8
85	84	58.5	2	6	58.5
86	359.5	65.5	2	90.5	65.5
87	1.5	1	1	268.5	1
88	272	53	1	358	53
89	189	31.5	1	81	31.5
90	353.5	8	2	96.5	8
91	37.5	79.5	2	52.5	79.5
92	255.5	57	1	14.5	57
93	14	57	2	76	57
94	352.5	60.5	2	97.5	60.5
95	277	55	1	353	55
96	343	57	2	107	57
97	351.5	60	2	98.5	60
98	323	72.5	2	127	72.5
99	223	72	2	227	72
100	355	82.5	2	95	82.5
101	310	70	2	140	70
102	337.5	29.5	2	112.5	29.5
103	48.5	53	2	41.5	53
104	322	9	1	308	9

Universal Stage Data Conversion

Sample ID: WS-022-I

U-Stage Zero Position: 0°

	Universal Stage Measurement			Quartz C-axis	
	Trend	Plunge	Arc	Trend	Plunge
105	323	57	2	127	57
106	185	11	2	265	11
107	286	10	2	164	10
108	26.5	54.5	1	243.5	54.5
109	327	76	2	123	76
110	311.5	55	1	318.5	55
111	44	65.5	2	46	65.5
112	308	72.5	1	322	72.5
113	59	53	1	211	53
114	57	47.5	2	33	47.5
115	70.5	68.5	2	19.5	68.5
116	69.5	70.5	2	20.5	70.5
117	316	57	2	134	57
118	50.5	55.5	2	39.5	55.5
119	297	77	1	333	77
120	296	80	2	154	80
121	58	48	2	32	48
122	291	23.5	2	159	23.5
123	16.5	58	2	73.5	58
124	278.5	70.5	1	351.5	70.5
125	295.5	67	1	334.5	67
126	281	84	1	349	84
127	281	73	1	349	73
128	296	65	1	334	65
129	335	14	1	295	14
130	60.5	73	2	29.5	73
131	49.5	63	2	40.5	63
132	333	16.5	2	117	16.5
133	291.5	55.5	1	338.5	55.5
134	280.5	61	1	349.5	61
135	337	54.5	2	113	54.5
136	333	56.5	2	117	56.5
137	322.5	54.5	2	127.5	54.5
138	346	54	1	284	54
139	336.5	70	2	113.5	70
140	285	59	2	165	59
141	283	70	1	347	70
142	284	11	2	166	11
143	350	75.5	2	100	75.5
144	285	69.5	1	345	69.5
145	341.5	36	2	108.5	36
146	314.5	56	2	135.5	56
147	255	65.5	1	15	65.5
148	316	12	1	314	12
149	15	77.5	2	75	77.5
150	18	74.5	1	252	74.5
151	323.5	64	1	306.5	64
152	321	74	2	129	74
153	82	79	1	188	79
154	291	58.5	1	339	58.5
155	326.5	59	1	303.5	59
156	295.5	49.5	1	334.5	49.5

Universal Stage Data Conversion

Sample ID: WS-022-I

U-Stage Zero Position: 0º

	Universal Stage Measurement			Quartz C-axis	
	Trend	Plunge	Arc	Trend	Plunge
157	358	80	2	92	80
158	132	9	1	138	9
159	1	73	1	269	73
160	349.5	78.5	2	100.5	78.5
161	185.5	74	2	264.5	74
162	329	23.5	2	121	23.5
163	337.5	37	2	112.5	37
164	316.5	46	1	313.5	46
165	351	29	1	279	29
166	269	3	1	1	3
167	309	48	1	321	48
168	65.5	73.5	2	24.5	73.5
169	52.5	82	2	37.5	82
170	268.5	57.5	1	1.5	57.5
171	30.5	48	2	59.5	48
172	349	56	1	281	56
173	33.5	67	1	236.5	67
174	331	58.5	1	299	58.5
175	27.5	48	2	62.5	48
176	320.5	52	2	129.5	52
177	262	26.5	1	8	26.5
178	310	18	1	320	18
179	320	58.5	2	130	58.5
180	27	49.5	2	63	49.5
181	340	68	2	110	68
182	336	55	1	294	55
183	334.5	49	2	115.5	49
184	337.5	54	1	292.5	54
185	264	54.5	1	6	54.5
186	8	74.5	1	262	74.5
187	9.5	69	2	80.5	69
188	38	72.5	2	52	72.5
189	15	74.5	2	75	74.5
190	265.5	73	2	184.5	73
191	323	6.5	1	307	6.5
192	31	51.5	1	239	51.5
193	239	54	1	31	54
194	315	58.5	1	315	58.5
195	142.5	59.5	1	127.5	59.5
196	95	56.5	1	175	56.5
197	321	7.5	1	309	7.5
198	338	62.5	2	112	62.5
199	340	24	1	290	24
200	293	82	2	157	82
201	35	64.5	2	55	64.5
202	293.5	64.5	2	156.5	64.5
203	281.5	4	1	348.5	4
204	312	25.5	2	138	25.5
205	43	63.5	2	47	63.5
206	265	67	1	5	67
207	314	21	1	316	21
208	310	24	1	320	24

Universal Stage Data Conversion

Sample ID: WS-022-I

U-Stage Zero Position: 0º

	Universal Stage Measurement			Quartz C-axis	
	Trend	Plunge	Arc	Trend	Plunge
209	285	83	2	165	83
210	14	61.5	1	256	61.5
211	302.5	73	1	327.5	73
212	288	64.5	1	342	64.5
213	311.5	46	1	318.5	46
214	59	79	2	31	79
215	304.5	47	1	325.5	47
216	314	71.5	1	316	71.5
217	32	73	1	238	73
218	316.5	53	1	313.5	53
219	195	56	1	75	56
220	305.5	63	1	324.5	63
221	320	8	2	130	8
222	325.5	0.5	1	304.5	0.5
223	74	73.5	2	16	73.5
224	308	56.5	2	142	56.5
225	319	52	1	311	52
226	54	80.5	1	216	80.5
227	298	77	1	332	77
228	297.5	73.5	1	332.5	73.5
229	193.5	53	1	76.5	53
230	280	69	1	350	69
231	294	59.5	1	336	59.5
232	336.5	50	2	113.5	50
233	331.5	48	2	118.5	48
234	347	53	1	283	53
235	335	66	2	115	66
236	286	61	1	344	61
237	279.5	63	1	350.5	63
238	284.5	18	2	165.5	18
239	341	40	2	109	40
240	322	63	1	308	63
241	351	15	2	99	15
242	295.5	51.5	1	334.5	51.5
243	3.5	75.5	1	266.5	75.5
244	271.5	84.5	1	358.5	84.5
245	296.5	17	2	153.5	17
246	345	60	2	105	60
247	37	78	2	53	78
248	300.5	51	1	329.5	51
249	78	49.5	2	12	49.5
250	61	77	2	29	77
251	267	60	1	3	60
252	296.5	51.5	1	333.5	51.5
253	323	56.5	2	127	56.5
254	327	54.5	2	123	54.5
255	271	53	1	359	53
256	294	77	1	336	77
257	334.5	16	2	115.5	16
258	315	66	1	315	66
259	320.5	21.5	2	129.5	21.5
260	59	48	2	31	48

Universal Stage Data Conversion

Sample ID: WS-022-I

U-Stage Zero Position: 0º

	Universal Stage Measurement			Quartz C-axis	
	Trend	Plunge	Arc	Trend	Plunge
261	295	69	1	335	69
262	335	63	2	115	63
263	318	30	1	312	30
264	31	47.5	1	239	47.5
265	206	78	2	244	78
266	318.5	52	1	311.5	52
267	306.5	69.5	1	323.5	69.5
268	306.5	74	1	323.5	74
269	70.5	71	2	19.5	71
270	27	76	2	63	76
271	80.5	60.5	2	9.5	60.5
272	286	11.5	1	344	11.5
273	285.5	62.5	1	344.5	62.5
274	339.5	59.5	1	290.5	59.5
275	263.5	59	1	6.5	59
276	324	56	1	306	56
277	358	58.5	2	92	58.5
278	339	51.5	1	291	51.5
279	309	74.5	2	141	74.5
280	61.5	68	2	28.5	68
281	293.5	58.5	1	336.5	58.5
282	340	65.5	2	110	65.5
283	297.5	70.5	1	332.5	70.5
284	300.5	32.5	2	149.5	32.5
285	134	76	1	136	76
286	342.5	65.5	1	287.5	65.5
287	312.5	20	1	317.5	20
288	29	35	2	61	35
289	265	56	1	5	56
290	84	74	2	6	74
291	313.5	29	1	316.5	29
292	313.5	74	1	316.5	74
293	337.5	15	1	292.5	15
294	336.5	19	1	293.5	19
295	311.5	1	2	138.5	1
296	316	15.5	1	314	15.5

Universal Stage Data Conversion

Sample ID: WS-037-I

U-Stage Zero Position: 0°

	Universal Stage Measurement			Quartz C-axis	
	Trend	Plunge	Arc	Trend	Plunge
1	301	1	2	149	1
2	336	54	1	294	54
3	39	46	2	51	46
4	43	42	2	47	42
5	313	48	1	317	48
6	323	50	1	307	50
7	74	46	2	16	46
8	326	49	1	304	49
9	52	45	2	38	45
10	43	72	1	227	72
11	284	62	1	346	62
12	36	53	2	54	53
13	291	50	1	339	50
14	314	57	1	316	57
15	287	55	2	163	55
16	313	47	2	137	47
17	76	3	2	14	3
18	158	65	1	112	65
19	272	71	2	178	71
20	194	68	2	256	68
21	305	20	1	325	20
22	339	75	2	111	75
23	294	14	2	156	14
24	297	50	2	153	50
25	65	56	2	25	56
26	313	51	2	137	51
27	68	47	2	22	47
28	288	20	2	162	20
29	43	48	2	47	48
30	51	55	2	39	55
31	225	57	1	45	57
32	184	75	2	266	75
33	313	68	2	137	68
34	277	77	2	173	77
35	51	21	1	219	21
36	268	34	2	182	34
37	61	26	1	209	26
38	38	23	1	232	23
39	62	62	1	208	62
40	101	51	2	349	51
41	325	1	2	125	1
42	49	30	2	41	30
43	295	9	1	335	9
44	27	68	2	63	68
45	274	9	1	356	9
46	332	17	2	118	17
47	249	72	1	21	72
48	47	13	1	223	13
49	287	53	2	163	53
50	328	16	1	302	16
51	294	56	2	156	56
52	63	55	1	207	55

Universal Stage Data Conversion

Sample ID: WS-037-I

U-Stage Zero Position: 0°

	Universal Stage Measurement			Quartz C-axis	
	Trend	Plunge	Arc	Trend	Plunge
53	100	59	1	170	59
54	64	53	2	26	53
55	335	1	1	295	1
56	315	1	2	135	1
57	37	49	2	53	49
58	280	29	2	170	29
59	69	22	1	201	22
60	70	23	1	200	23
61	71	20	1	199	20
62	326	25	2	124	25
63	324	18	2	126	18
64	59	51	2	31	51
65	308	15	2	142	15
66	71	51	2	19	51
67	313	5	2	137	5
68	296	48	2	154	48
69	277	24	1	353	24
70	274	76	2	176	76
71	312	20	1	318	20
72	80	56	1	190	56
73	294	12	2	156	12
74	298	33	2	152	33
75	49	16	1	221	16
76	350	61	2	100	61
77	296	15	2	154	15
78	321	35	2	129	35
79	307	32	2	143	32
80	309	12	1	321	12
81	323	29	2	127	29
82	344	13	1	286	13
83	21	7	1	249	7
84	27	67	1	243	67
85	308	16	2	142	16
86	323	12	2	127	12
87	279	34	2	171	34
88	285	77	2	165	77
89	276	4	2	174	4
90	315	8	1	315	8
91	72	1	1	198	1
92	284	75	2	166	75
93	348	77	2	102	77
94	308	57	1	322	57
95	317	74	1	313	74
96	145	67	2	305	67
97	288	20	1	342	20
98	345	6	2	105	6
99	321	17	2	129	17
100	158	73	2	292	73
101	283	54	1	347	54
102	303	23	1	327	23
103	292	51	1	338	51
104	47	8	2	43	8

Universal Stage Data Conversion

Sample ID: WS-037-I

U-Stage Zero Position: 0°

	Universal Stage Measurement				Quartz C-axis	
	Trend	Plunge	Arc		Trend	Plunge
105	300	21	2		150	21
106	274	26	2		176	26
107	269	74	1		1	74
108	298	75	2		152	75
109	144	80	2		306	80
110	323	22	2		127	22
111	68	21	1		202	21
112	132	57	1		138	57
113	344	48	2		106	48
114	314	26	2		136	26
115	303	55	1		327	55
116	283	33	2		167	33
117	129	12	1		141	12
118	312	21	2		138	21
119	321	33	1		309	33
120	313	26	2		137	26
121	223	77	1		47	77
122	300	2	2		150	2
123	297	54	1		333	54
124	337	66	2		113	66
125	315	60	1		315	60
126	359	81	2		91	81
127	298	15	2		152	15
128	299	46	1		331	46
129	315	19	2		135	19
130	308	57	1		322	57
131	333	67	1		297	67
132	287	50	1		343	50
133	315	52	1		315	52
134	298	67	1		332	67
135	298	62	1		332	62
136	315	5	1		315	5
137	192	63	1		78	63
138	310	20	2		140	20
139	296	27	2		154	27
140	296	29	2		154	29
141	173	54	2		277	54
142	302	49	1		328	49
143	299	56	1		331	56
144	70	12	1		200	12
145	324	14	1		306	14
146	307	38	2		143	38
147	275	14	1		355	14
148	323	7	1		307	7
149	273	5	2		177	5
150	67	79	1		203	79
151	284	20	2		166	20
152	279	59	2		171	59
153	284	64	2		166	64
154	303	72	1		327	72
155	317	70	2		133	70
156	312	73	2		138	73

Universal Stage Data Conversion

Sample ID: WS-037-I

U-Stage Zero Position: 0°

	Universal Stage Measurement			Quartz C-axis	
	Trend	Plunge	Arc	Trend	Plunge
157	316	67	2	134	67
158	74	75	1	196	75
159	280	24	2	170	24
160	324	78	2	126	78
161	316	71	2	134	71
162	3	82	2	87	82
163	57	59	1	213	59
164	55	53	1	215	53
165	92	74	2	358	74
166	349	73	2	101	73
167	30	57	2	60	57
168	6	1	1	264	1
169	308	60	2	142	60
170	303	1	1	327	1
171	327	56	1	303	56
172	58	18	2	32	18
173	55	77	2	35	77
174	87	68	1	183	68
175	301	72	1	329	72
176	312	69	2	138	69
177	81	8	1	189	8
178	64	63	2	26	63
179	46	70	2	44	70
180	66	23	2	24	23
181	64	20	2	26	20
182	76	70	2	14	70
183	273	66	2	177	66
184	317	27	1	313	27
185	338	77	2	112	77
186	29	49	1	241	49
187	255	72	2	195	72
188	294	49	1	336	49
189	47	55	2	43	55
190	138	53	2	312	53
191	308	29	2	142	29
192	70	17	2	20	17
193	268	21	1	2	21
194	334	60	1	296	60
195	331	66	1	299	66
196	65	67	1	205	67
197	67	21	1	203	21
198	301	56	1	329	56
199	262	67	2	188	67
200	228	71	2	222	71
201	309	57	1	321	57
202	335	12	1	295	12
203	278	32	2	172	32
204	315	73	2	135	73
205	78	25	2	12	25
206	78	80	2	12	80
207	297	72	2	153	72
208	294	51	2	156	51

Universal Stage Data Conversion

Sample ID: WS-037-I

U-Stage Zero Position: 0°

	Universal Stage Measurement			Quartz C-axis	
	Trend	Plunge	Arc	Trend	Plunge
209	311	67	2	139	67
210	309	32	2	141	32
211	40	50	2	50	50
212	296	30	2	154	30
213	66	53	2	24	53
214	351	58	1	279	58
215	293	70	2	157	70
216	82	13	1	188	13
217	296	68	1	334	68
218	326	50	2	124	50
219	292	21	1	338	21
220	306	37	2	144	37
221	310	1	2	140	1
222	39	80	2	51	80
223	326	30	1	304	30
224	309	8	1	321	8
225	287	58	1	343	58
226	37	21	2	53	21
227	295	20	2	155	20
228	308	1	2	142	1
229	253	13	1	17	13
230	337	28	1	293	28
231	25	63	1	245	63
232	70	51	2	20	51
233	311	52	2	139	52
234	286	47	1	344	47
235	308	46	1	322	46
236	20	33	2	70	33
237	298	35	1	332	35
238	327	33	1	303	33
239	64	32	2	26	32
240	314	61	1	316	61
241	48	23	1	222	23
242	65	5	1	205	5
243	313	51	2	137	51
244	33	72	2	57	72
245	273	17	2	177	17
246	321	66	1	309	66
247	37	50	2	53	50
248	324	3	2	126	3
249	295	49	1	335	49
250	289	62	2	161	62
251	41	47	2	49	47
252	62	75	2	28	75
253	16	77	2	74	77
254	171	65	2	279	65
255	119	76	1	151	76
256	67	32	2	23	32
257	299	1	1	331	1
258	330	1	1	300	1
259	333	1	2	117	1
260	323	23	2	127	23

Universal Stage Data Conversion

	Sample ID:	WS-037-I		U-Stage Zero Position:		0°
	Universal Stage Measurement			Quartz C-axis		
	Trend	Plunge	Arc	Trend	Plunge	
261	173	54	2	277	54	
262	282	2	2	168	2	
263	311	48	1	319	48	
264	307	53	1	323	53	
265	304	21	2	146	21	

Universal Stage Data Conversion

Sample ID: WS-024-II

U-Stage Zero Position: 90^o

	Universal Stage Measurement			Quartz C-axis	
	Trend	Plunge	Arc	Trend	Plunge
1	377	32	1	253	32
2	313.5	12.5	2	136.5	12.5
3	301.5	21	1	328.5	21
4	314.5	20.5	2	135.5	20.5
5	350	24.5	1	280	24.5
6	352	33	1	278	33
7	321	35	1	309	35
8	316.5	38	1	313.5	38
9	328	19	2	122	19
10	287	29	1	343	29
11	322.5	23	1	307.5	23
12	345	13.5	2	105	13.5
13	305	15.5	1	325	15.5
14	280.5	19	2	169.5	19
15	306	22	1	324	22
16	360.5	60.5	1	269.5	60.5
17	269.5	28	2	180.5	28
18	286	8	2	164	8
19	334.5	17	2	115.5	17
20	329	17	2	121	17
21	370.5	24.5	2	79.5	24.5
22	190	26	2	260	26
23	327	11	1	303	11
24	336.5	21.5	2	113.5	21.5
25	269.5	28	2	180.5	28
26	342	40	1	288	40
27	297.5	33	2	152.5	33
28	322	29.5	2	128	29.5
29	278	29.5	2	172	29.5
30	296	9.5	1	334	9.5
31	268	60	2	182	60
32	321	26	2	129	26
33	294	20	1	336	20
34	323.5	5	1	306.5	5
35	355	10.5	1	275	10.5
36	303.5	26	2	146.5	26
37	274	33	1	356	33
38	301	30	1	329	30
39	281.5	34	1	348.5	34
40	331	32	2	119	32
41	343.5	78.5	2	106.5	78.5
42	286.5	29.5	2	163.5	29.5
43	310.5	16	2	139.5	16
44	336	26.5	1	294	26.5
45	319.5	20	1	310.5	20
46	582	45	1	48	45
47	331	15	2	119	15
48	377	25	1	253	25
49	306	27	1	324	27
50	325.5	30	1	304.5	30
51	304	23.5	2	146	23.5
52	266	12.5	2	184	12.5

Universal Stage Data Conversion

Sample ID: WS-024-II

U-Stage Zero Position: 90°

	Universal Stage Measurement			Quartz C-axis	
	Trend	Plunge	Arc	Trend	Plunge
53	500	7	1	130	7
54	417	62.5	1	213	62.5
55	300.5	31.5	1	329.5	31.5
56	282	28	2	168	28
57	412	58.5	1	218	58.5
58	329.5	61	1	300.5	61
59	399	60.5	1	231	60.5
60	348	15.5	2	102	15.5
61	340.5	68.5	1	289.5	68.5
62	344	35	2	106	35
63	350.5	33	2	99.5	33
64	349	0.5	1	281	0.5
65	311.5	19	1	318.5	19
66	410.5	49	1	219.5	49
67	277.5	23	2	172.5	23
68	301	36	2	149	36
69	270	9	2	180	9
70	271	13	2	179	13
71	269.5	13	2	180.5	13
72	269	9	2	181	9
73	313	10	2	137	10
74	287	18	2	163	18
75	406.5	20	1	223.5	20
76	343	5	1	287	5
77	340	33.5	1	290	33.5
78	348.5	35.5	1	281.5	35.5
79	298	23	2	152	23
80	296	1.5	1	334	1.5
81	345	8.5	1	285	8.5
82	353	19	2	97	19
83	353	8	2	97	8
84	295	4	2	155	4
85	355	5.5	2	95	5.5
86	344.5	7.5	2	105.5	7.5
87	345.5	10.5	2	104.5	10.5
88	282	36	2	168	36
89	342.5	22.5	1	287.5	22.5
90	284	8.5	2	166	8.5
91	622.5	36	1	7.5	36

Universal Stage Data Conversion

Sample ID: WS-020-II

U-Stage Zero Position: 90°

	Universal Stage Measurement			Quartz C-axis	
	Trend	Plunge	Arc	Trend	Plunge
1	315	32	1	315	32
2	412	30	1	218	30
3	218.5	11.5	2	231.5	11.5
4	367.5	54.5	1	262.5	54.5
5	311	34	1	319	34
6	327	22	2	123	22
7	399.5	76.5	1	230.5	76.5
8	307.5	6.5	1	322.5	6.5
9	329.5	60	2	120.5	60
10	295	10	1	335	10
11	401	53	1	229	53
12	333.5	8	1	296.5	8
13	421.5	55	1	208.5	55
14	291	13	2	159	13
15	272	31	2	178	31
16	250	25.5	2	200	25.5
17	425	54	1	205	54
18	367	53.5	2	83	53.5
19	323	9.5	1	307	9.5
20	332	53.5	1	298	53.5
21	334.5	17	1	295.5	17
22	356	60	1	274	60
23	363.5	54.5	1	266.5	54.5
24	364	53.5	1	266	53.5
25	331	9	1	299	9
26	328	9.5	1	302	9.5
27	346	28.5	1	284	28.5
28	349.5	37.5	1	280.5	37.5
29	325.5	7	2	124.5	7
30	325	9	1	305	9
31	345.5	5.5	1	284.5	5.5
32	304.5	35	1	325.5	35
33	330	32.5	1	300	32.5
34	310	71	2	140	71
35	382	52	1	248	52
36	343.5	55.5	1	286.5	55.5
37	313	6	1	317	6
38	296	10.5	1	334	10.5
39	308	24	2	142	24
40	422.5	50.5	1	207.5	50.5
41	297.5	29	1	332.5	29
42	315	12	1	315	12
43	316	16	1	314	16
44	329	57.5	1	301	57.5
45	344	5	1	286	5
46	300	14	1	330	14
47	355.5	64	1	274.5	64
48	266	8.5	2	184	8.5
49	383	62.5	1	247	62.5
50	270	32	1	0	32
51	131.5	56	2	318.5	56
52	306	56	1	324	56

Universal Stage Data Conversion

Sample ID: WS-020-II

U-Stage Zero Position: 90°

	Universal Stage Measurement			Quartz C-axis	
	Trend	Plunge	Arc	Trend	Plunge
53	299.5	54	1	330.5	54
54	347.5	6	2	102.5	6
55	401.5	46.5	1	228.5	46.5
56	317	10	1	313	10
57	395.5	47	1	234.5	47
58	294	9	2	156	9
59	320	8	1	310	8
60	293	10	1	337	10
61	311.5	9	1	318.5	9
62	304.5	15	2	145.5	15
63	278.5	31.5	2	171.5	31.5
64	269	32.5	2	181	32.5
65	279.5	28.5	2	170.5	28.5
66	281	7.5	1	349	7.5
67	287.5	24.5	2	162.5	24.5
68	312.5	30	1	317.5	30
69	340.5	30.5	1	289.5	30.5
70	305	60	1	325	60
71	388.5	60	1	241.5	60
72	336	52	1	294	52
73	292	24	1	338	24
74	367	58	2	83	58
75	345.5	8	1	284.5	8
76	282	19	1	348	19
77	338	10	1	292	10
78	387	54.5	1	243	54.5
79	415.5	55.5	1	214.5	55.5
80	609	54	1	21	54
81	358	66	1	272	66
82	314.5	13.5	1	315.5	13.5
83	308	36	1	322	36
84	340	7.5	1	290	7.5
85	340	8.5	1	290	8.5
86	388	60.5	1	242	60.5
87	385.5	59.5	1	244.5	59.5
88	360	54.5	1	270	54.5
89	351	5	1	279	5
90	344	12.5	2	106	12.5
91	284.5	8	1	345.5	8
92	345	8	1	285	8
93	268.5	30.5	2	181.5	30.5
94	271.5	52	2	178.5	52
95	274	27	2	176	27
96	349.5	10.5	1	280.5	10.5
97	308	55.5	1	322	55.5

APPENDIX E

Deformation Temperature of WS-037-I

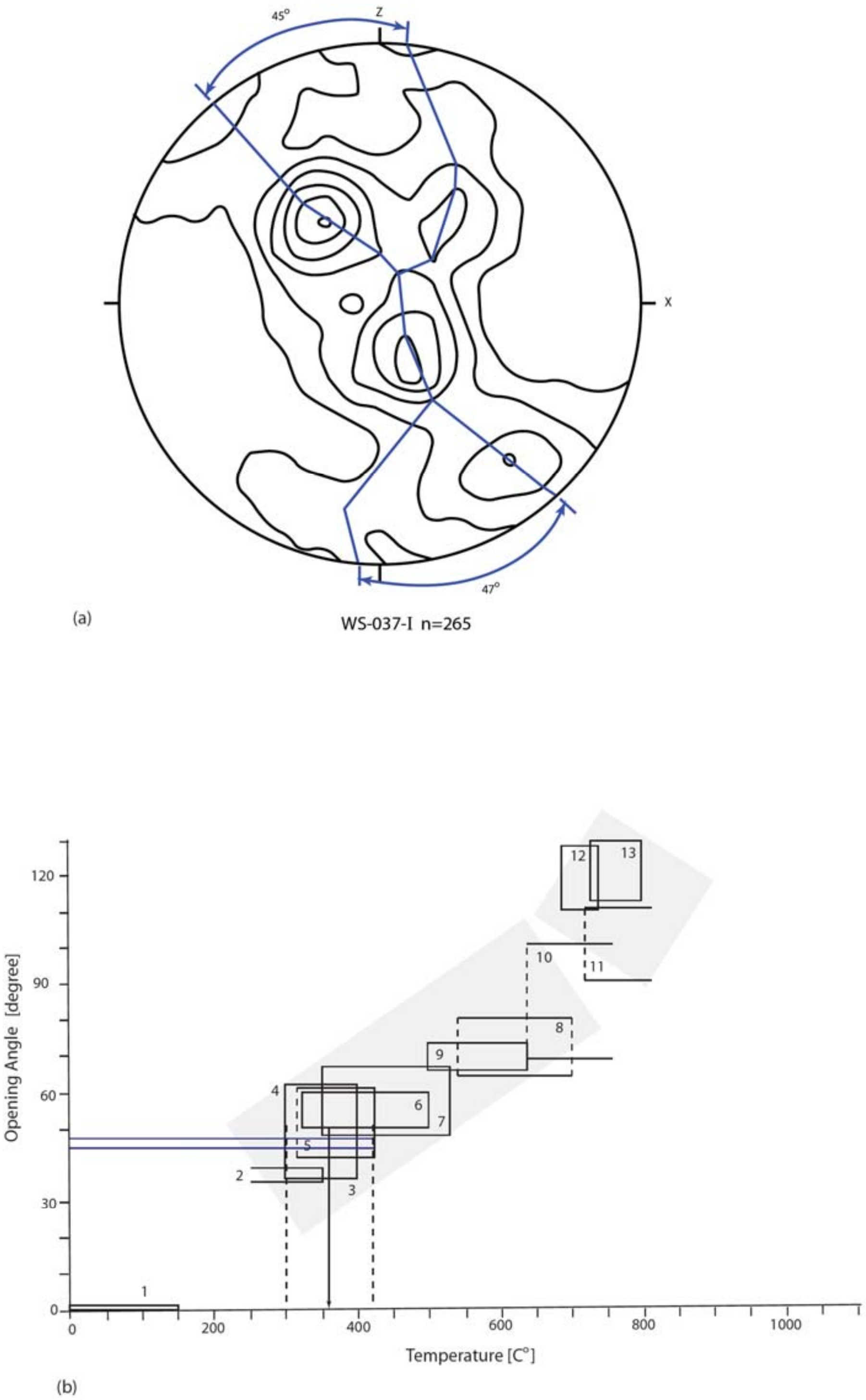

Figure E-1. Quartz c-axis central girdle opening angle (a). Possible deformation temperature (b) (after Kruhl, 1998).

VITA

Ching Tu was born in Taipei, Taiwan in May 27th 1969. She attended Tung-Nan Junior College of Technology (now Tungnan University), where she received a diploma from the Civil Engineering Department. She entered the geology program at University of Tennessee in spring, 2003, and graduated in spring, 2006 (Summa Cum Laude) earning her Bachelor of Science degree in geology. She entered graduate program in fall 2006 and earned her Master of Science degree in May, 2009.